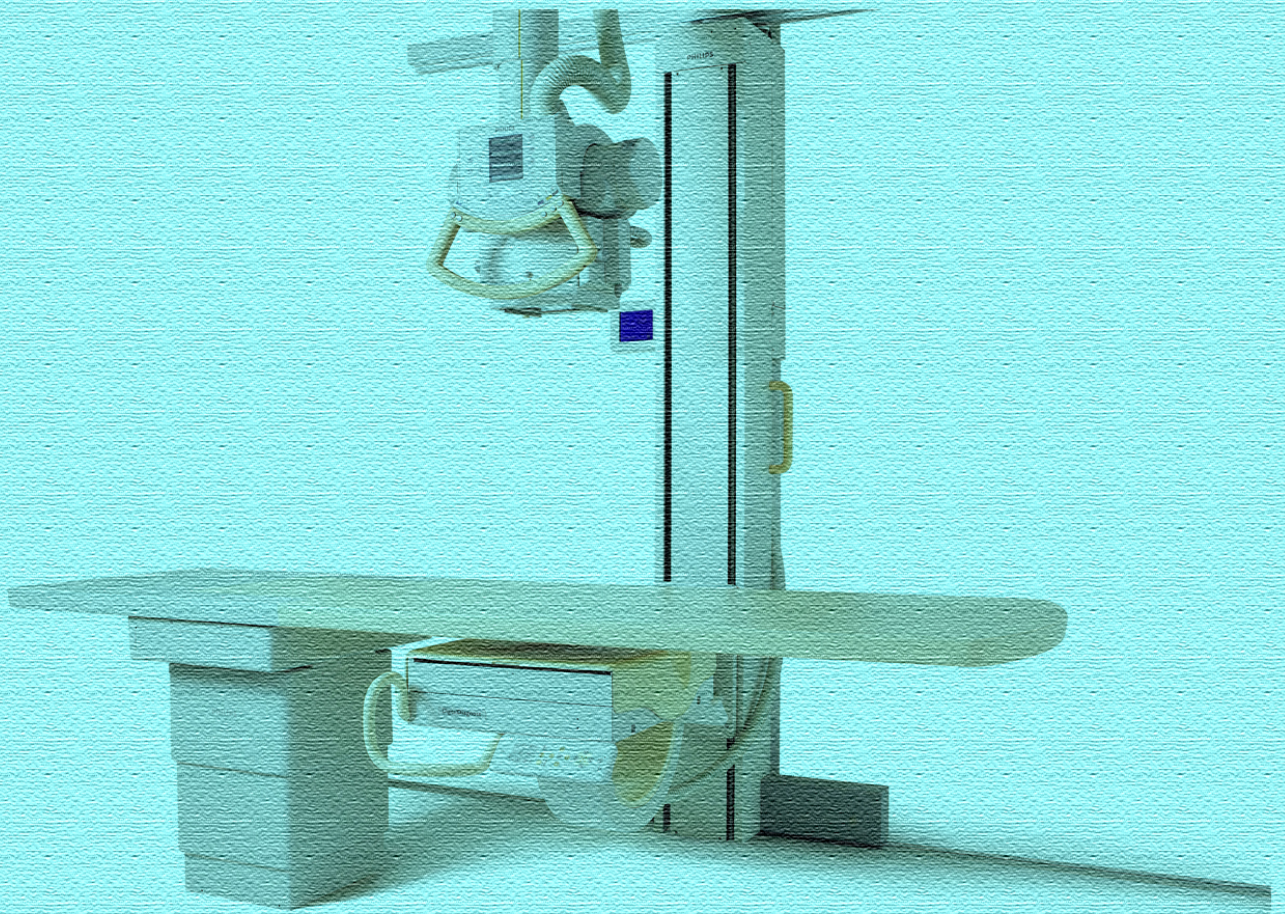


RADIOLOGY

Open Journal 



| September 2016 | Volume 1 | Issue 2 |

Editor-in-Chief
Chung-Ming Chen, PhD

Co-Editor-in-Chief
Rajendra Badgaiyan, MD

Associate Editors
Fei Liu, PhD
Alessandro Arrigo, MD
Priya Bhosale, MD

TABLE OF CONTENTS

Editorial

1. Bio-Mathematical Modelling in Tumor Evaluation Via Magnetic Resonance Imaging e11-e13
– *Mario Sansone**

Case Report

2. Extrapleural Solitary Fibrous Tumor of Foot: A Case Report 35-38
– *Yuko Kobashi*, Yohei Munetomo, Akira Baba, Shinji Yamazoe and Takuji Mogami*

Short Communication

3. Stereotactic Body Radiation Therapy Treatment for Prostate Cancer: From Setup to Delivery Strategies 39-41
– *Stefania Clemente**

Systematic Review

4. Does Iterative Reconstruction Improve Image Quality and Reduce Dose in Computed Tomography? 42-54
– *Dejian Qiu* and Euclid Seeram*

Case Report

5. Two Case Reports of Angioleiomyoma of the Finger 55-59
– *Yuko Kobashi*, Yohei Munetomo, Akira Baba, Shinji Yamazoe, Takuji Mogami and Jun Miyauch*

Review

6. On the Destruction of Cancer Cells Using Laser-Induced Shock Waves: A Review on Experiments and Multiscale Computer Simulations 60-75
– *Martin Oliver Steinhauser**

Editorial

*Corresponding author
Mario Sansone, PhD

Assistant Professor
Department of Electrical Engineering
and Information Technologies
University of Naples Federico II
Via Claudio 21, Naples 8013, Italy
E-mail: msansone@unina.it

Volume 1 : Issue 2

Article Ref. #: 1000ROJ1e003

Article History

Received: August 25th, 2016

Accepted: August 26th, 2016

Published: August 30th, 2016

Citation

Sansone M. Bio-mathematical modelling in tumor evaluation via magnetic resonance imaging. *Radiol Open J.* 2016; 1(2): e11-e13. doi: [10.17140/ROJ-1-e003](https://doi.org/10.17140/ROJ-1-e003)

Copyright

©2016 Sansone M. This is an open access article distributed under the Creative Commons Attribution 4.0 International License (CC BY 4.0), which permits unrestricted use, distribution, and reproduction in any medium, provided the original work is properly cited.

Bio-Mathematical Modelling in Tumor Evaluation Via Magnetic Resonance Imaging

Mario Sansone, PhD*

Department of Electrical Engineering and Information Technologies, University of Naples Federico II, Via Claudio 21, Naples 8013, Italy

In the last 25 years, within the field of tumor evaluation using magnetic resonance imaging (MRI), 2 main promising applications have emerged that can provide useful *functional* information beyond the morphological images: dynamic contrast enhanced MRI (DCE-MRI) and diffusion weighted imaging (DWI or DW-MRI). DCE-MRI involves the administration of a contrast medium that, flowing into the vascular network feeding the tumor, might give information on tissue vascular perfusion which is related to the *angiogenesis* phenomenon, in turn associated to tumor growth. DWI exploits the water brownian motion that is affected by tissue cellularity and vascularization. The successful application of both DCE-MRI and DWI lays strongly on both technical MRI improvements achieved in the last decades and on adequate bio-mathematical modelling of tissues. In this editorial, I will briefly discuss a few main issues of both applications focussing on bio-mathematical modelling.

DCE-MRI

The main technical issues in DCE-MRI concern the trade-off between time-space resolution and accurate quantification of contrast medium concentration. They both affect the accuracy of bio-mathematical modelling typically used in DCE assessment of the tumor.

In the early years of DCE, radiologists mainly looked at the *shape* of the time-intensity curve of a single voxel or averaged regions of interest (ROIs); in fact, it had been observed that, after contrast medium administration, a typical aggressive (malignant) tumor showed a wash-in (absorption) and a wash-out (excretion) phase while a benign lesion showed a slow absorption rate. However, this type of analysis was strongly reader-dependent and did not allow to easily and quantitatively compare subsequent studies of the same subject or studies from different subjects. It was clear that a more quantitative approach was needed.

Several groups (Tofts et al¹, Larsson et al², Brix et al³) proposed to use bio-mathematical models to analyze DCE data. These early models are based mainly on tissue compartmentalization (plasma and extracellular compartments) and the interesting parameters are the kinetics constants of exchange across compartments that are related to the permeability of the vessel walls: in fact, immature, leaky vessels (quickly grown stimulated with the vascular endothelial growing factor (VEGF) by the tumor) should show a higher permeability.⁴ However, these models are a strong simplification of reality because of limitation of the technical equipments available at that time. In fact, the need for high resolution images prevented fast acquisition of multiple series.

Today, a number of fast pulse sequences of acquisition give the possibility to use more realistic bio-mathematical models: different groups Koh et al⁵, Schabel et al⁶, Sourbron⁷ have proposed more sophisticated models including some aspects not considered by the first generation models: the rough approximation of only 2 compartments within a voxel has been abandoned and a more realistic distribution of compartments is considered instead: moreover, capillary transit-time (the time required for a contrast medium particle to travel across a capillary) and vascular permeability are considered random variables with a certain distribution

within the voxel (region) of interest.

The complexity of the model and the measurement uncertainty pose some limits in the evaluation of the kinetics parameters (permeability, vascular fraction, transit time, etc.): the accuracy (repeatability) with which these parameters can be evaluated is intrinsically limited by mathematical constraints.⁸ Moreover, accurate measurement of the contrast medium concentration within the voxel is still an issue because fast pulse sequences can overcome the time-space resolution trade-off but typically introduce some additional uncertainty in the measurement.⁹

Therefore, it is important for the radiologists evaluating the parametric maps to be supported by specialised professionals (such as biomedical engineers) in the interpretation of these maps in order to take into account the quality of the map reconstruction.

DWI

DWI was born for brain perfusion assessment¹⁰ (and has quickly evolved leading to the tractography¹¹ that is not considered further here) and has been quickly becoming an important tool for the evaluation of tumors in other body parts such as prostate¹² and breast.¹³ The diffusion of water (brownian motion) has been studied by many physicists among which Einstein gave an important contribution: in fact, considering the diffusion as a random process he established the relation between the *diffusion constant*, the time of observation and the path of a water particle. Diffusion within biological tissues depends on tissue organization: in order to evaluate whether there are some preferred directions of motion, the concept of *diffusion tensor imaging* (roughly, diffusion constants along 3 orthogonal directions) has been introduced.¹⁴

During DWI acquisition random moving spins are affected by magnetic gradients in such a way that fast diffusing water molecules contribute to attenuate the signal from a specific voxel. The magnetic gradients parameters are called b-values. In this way, qualitative maps can be obtained in which voxels with fast diffusing water are represented by darker colors.¹⁵ However, this type of images give information on the apparent diffusion coefficient (ADC) because true molecular water diffusion is restricted and hindered by vascular tortuosity.

To overcome this issue, the first bio-mathematical model of water diffusion within biological tissues has been developed by Le Bihan et al¹⁶ in the late 1980's. This model, called intra-voxel-incoherent-motion (IVIM), again considered the tissues within a voxel as organized in compartments (capillaries and extracellular space). In this model the interesting quantities are the vascular fraction, the water diffusion constant and the pseudo-diffusion constant. This latter has been introduced to account for the *random* orientation of vessels in tissues.

As in the case of DCE-MRI, also in the case of DW-MRI the quantitative analysis is limited by mathematical constraints. Specifically, the b-values used in DW acquisition strongly affect the accuracy of parameters estimation. Very sophisticated solutions have been proposed in the field of tractography¹⁴; moreover, some studies have been performed in the field of tumor evaluation¹⁷; however, this issue is still under debate and no definitive solution is currently available.

Finally, a very interesting issue is the link between the different models. As the mentioned models describe different measurements of related quantities (liquid flow and diffusion across compartments within tissues) it seems not unreasonable that model parameters should be related across different models. A link between perfusion and IVIM models was first suggested theoretically by Le Bihan et al.¹⁸ This link, if definitively shown, might be used to cross-validate DCE and DW studies and possibly to improve the accuracy of parametric maps. However, in the field of tumor studies, it seems that this issue has not been yet addressed specifically: a very small number of studies has been performed in this direction^{13,19} but they did not show this link in a conclusive manner.

REFERENCES

1. Tofts PS, Kermode AG. Measurement of the blood-brain barrier permeability and leakage space using dynamic MR imaging. 1. Fundamental concepts. *Magn Reson Med.* 1991; 17(2): 357-367. doi: [10.1002/mrm.1910170208](https://doi.org/10.1002/mrm.1910170208)
2. Larsson HBW, Tofts PS. Measurement of blood-brain barrier permeability using dynamic Gd-DTPA scanning-a comparison of methods. *Magn Reson Med.* 1992; 24(1): 174-176. doi: [10.1002/mrm.1910240119](https://doi.org/10.1002/mrm.1910240119)
3. Brix G, Semmler W, Port R, Schad LR, Layer G, Lorenz WJ. Pharmacokinetic parameters in CNS Gd-DTPA enhanced MR imaging. *J Comput Assist Tomogr.* 1991; 15(4): 621-628. Web site. http://journals.lww.com/jcat/abstract/1991/07000/pharmacokinetic_parameters_in_cns_gd_dtpa_enhanced.18.aspx. Accessed August 24, 2016

4. Alan J, Buckley DL, Parker GJM. *Dynamic Contrast-Enhanced Magnetic Resonance Imaging in Oncology*. Berlin, Germany: Springer; 2005: 309.
5. Koh TS, Cheong LH, Tan CK, Lim CC. A distributed parameter model of cerebral blood-tissue exchange with account of capillary transit time distribution. *Neuroimage*. 2006; 30(2): 426-435. Web site. <http://search.proquest.com/openview/6ae90c9b0b9898df4dbf5cc177a6c42b/1?pq-origsite=gscholar&cbl=2031077>. Accessed August 24, 2016
6. Schabel MC. A unified impulse response model for DCE-MRI. *Magn Reson Med*. 2012; 68(5): 1632-1646. doi: [10.1002/mrm.24162](https://doi.org/10.1002/mrm.24162)
7. Sourbron S. A tracer-kinetic field theory for medical imaging. *IEEE Trans Med Imaging*. 2014; 33(4): 935-946. doi: [10.1109/TMI.2014.2300450](https://doi.org/10.1109/TMI.2014.2300450)
8. Bates DM, Watts DG. *Nonlinear Regression Analysis and Its Applications*. 2nd ed. USA: John Wiley & Sons, Inc; 1988: 87.
9. Sansone M, Fusco R, Petrillo A. Accuracy of contrast agent quantification in MRI: A comparison between two k-space sampling schemes. *Appl Magn Reson*. 2015; 46: 1283. doi: [10.1007/s00723-015-0718-8](https://doi.org/10.1007/s00723-015-0718-8)
10. Le Bihan D, Breton E, Lallemand D, Grenier P, Cabanis E, Laval-Jeantet M. MR imaging of intravoxel incoherent motions: application to diffusion and perfusion in neurologic disorders. *Radiology*. 1986; 161(2): 401-407. Web site. <http://www.meteoreservice.com/PDFs/DLBRadiology86.pdf>. Accessed August 24, 2016
11. Kinoshita Y, Ono M, Okuda Y, et al. MR tractography--visualization of structure of nerve fiber system from diffusion weighted images with maximum intensity projection method. *Nihon Igaku Hoshasen Gakkai Zasshi*. 1993; 53(2): 171-179. Web site. <http://eurekamag.com/research/008/982/008982405.php>. Accessed August 24, 2016
12. Fusco R, Sansone M, Petrillo M, et al. Multiparametric MRI for prostate cancer detection: Preliminary results on quantitative analysis of dynamic contrast enhanced imaging, diffusion-weighted imaging and spectroscopy imaging. *Magn Reson Imaging*. 34(7): 839-845. doi: [10.1016/j.mri.2016.04.001](https://doi.org/10.1016/j.mri.2016.04.001)
13. Fusco R, Sansone M, Filice S, Granata V, Catalano O, Amato DM. Integration of DCE-MRI and DW-MRI quantitative parameters for breast lesion classification. *BioMed Research International*. 2015; 237863: 12. doi: [10.1155/2015/237863](https://doi.org/10.1155/2015/237863)
14. Minati L, Węglarz WP. Physical foundations, models, and methods of diffusion magnetic resonance imaging of the brain: A review. *Concepts Magn Reson*. 2007; 30A: 278-307. doi: [10.1002/cmr.a.20094](https://doi.org/10.1002/cmr.a.20094)
15. Stejskal EO, Tanner JE. Spin diffusion measurements: Spin echoes in the presence of a time-dependent field gradient. *J Chem Phys*. 1965; 42(1): 288. doi: [10.1063/1.1695690](https://doi.org/10.1063/1.1695690)
16. Le Bihan D. Intravoxel incoherent motion imaging using steady-state free precession. *Magn Reson Med*. 1988; 7(3): 346-351. doi: [10.1002/mrm.1910070312](https://doi.org/10.1002/mrm.1910070312)
17. Lemke A, Stieltjes B, Schad LR, Laun FB. Toward an optimal distribution of b values for intravoxel incoherent motion imaging. *Magn Reson Imaging*. 2011; 29(6): 766-776. doi: [10.1016/j.mri.2011.03.004](https://doi.org/10.1016/j.mri.2011.03.004)
18. Le Bihan D, Turner R. The capillary network: A link between IVIM and classical perfusion. *Magn Reson Med*. 1992; 27(1): 171-178. Web site. <http://meteoreservice.com/PDFs/LeBihan92.pdf>. Accessed August 24, 2016
19. Sansone M, Fusco R, Petrillo A. An attempt to integrate diffusion weighted and dynamic contrast enhanced MRI. *Radiol Open J*. 1(1): 31-34. doi: [10.17140/ROJ-1-105](https://doi.org/10.17140/ROJ-1-105)

Case Report

Corresponding author

Yuko Kobashi, MD

Department of Radiology
Tokyo Dental College Ichikawa
General Hospital
5-11-13 Sugano, Ichikawa
Chiba, 272-8513 Japan
Tel. +81-47-325-0151
Fax: +81-47-325-4456
E-mail: ykobashi@ijkei.ac.jp

Volume 1 : Issue 2

Article Ref. #: 1000ROJ1106

Article History

Received: May 18th, 2016

Accepted: June 10th, 2016

Published: June 10th, 2016

Citation

Kobashi Y, Munetomo Y, Baba A, Yamazoe S, Mogami T. Extrapleural solitary fibrous tumor of foot: a case report. *Radiol Open J.* 2016; 1(2): 35-38. doi: [10.17140/ROJ-1-106](https://doi.org/10.17140/ROJ-1-106)

Copyright

©2016 Kobashi Y. This is an open access article distributed under the Creative Commons Attribution 4.0 International License (CC BY 4.0), which permits unrestricted use, distribution, and reproduction in any medium, provided the original work is properly cited.

Extrapleural Solitary Fibrous Tumor of Foot: A Case Report

Yuko Kobashi, MD¹; Yohei Munetomo, MD¹; Akira Baba, MD¹; Shinji Yamazoe, MD¹; Takuji Mogami, MD¹

Department of Radiology, Tokyo Dental College, Ichikawa General Hospital, Ichikawa, Chiba, Japan

ABSTRACT

A 77-year-old woman was admitted to our Hospital for a mass lesion in the plantar area of the left foot. The patient referred that the mass was present for about 30 years but it had never been treated before because asymptomatic. Foot Magnetic Resonance Imaging (MRI) reviewed a low-signal-intensity tumor on both T1 weighted and T2 weighted images. Based on clinical and diagnostic imaging findings we initially suspected a fibroproliferative neoplasm like an aggressive fibromatosis. Histologically the lesion was benign fibroblastic spindle cell lesion with dense or loose collagen fibers. Cellularity was low and no mitotic figures were found. The tumor cells were positive for CD34, whereas they were negative for α smooth muscle actin, desmin, HHF35 and S100 protein. These pathological findings were consistent with an Extrapleural Solitary Fibrous Tumor (Extrapleural SFT). The Extrapleural SFT should be included in the differential diagnosis of extrapleural lesions in which MRI suggests fibrous content. These entities exhibit a dense fibrocollagenous matrix that can produce low signal intensity on T2-weighted MRI images, similar to Extrapleural SFT. However, in order to reach a proper diagnosis and treatment is essential to integrate a detailed patients' clinical history and to perform a biopsy to collect cells for closer examination.

KEYWORDS: Solitary fibrous tumor; MRI; CD34.

ABBREVIATIONS: Extrapleural SFT: Extrapleural Solitary Fibrous Tumor; MRI: Magnetic Resonance Imaging; CT: Computed Tomographic; WHO: World Health Organization.

INTRODUCTION

Extrapleural Solitary fibrous tumor (Extrapleural SFT) is a rare soft tissue tumor originating from mesenchymal cells.¹ Extrapleural SFT shows no gender predilection, affecting people across a wide age range, from 5 to 92 years.² Extrapleural SFT is usually a benign, slow-growing tumor, but a malignant behavior has also been reported.³ Although Extrapleural SFTs most commonly occur in the pleura, numerous extrapleural sites of involvement have been reported.⁴ We describe a rare case of an Extrapleural SFT in the plantar area of the left foot.

CASE REPORT

A 77-year-old woman was admitted to our hospital for a mass lesion in the plantar area of the left foot. The mass was present for about 30 years but it had never been treated before because stable in size over time and asymptomatic. However, the patient recently complained of pain in the sole of her foot after long distance walking.

The patient was affected by Alzheimer-type senile dementia and by poor controlled diabetes mellitus. On physical examination, the plantar mass was about 7 cm in diameter, elastic and hard to move. The skin overlying the mass was not red or blistered. Foot X-rays showed marked pressure erosions in the second and third metatarsal bones due to a compression by the

mass (Figure 1, arrows). Toes of the left foot showed osteopenic change suggestive of osteoporosis. On foot CT, a low density tumor measuring 10 cm in diameter was present in the plantar area (Figure 2, arrows). The calcaneus showed erosive changes which sclerotic margin for the long-lasting compression by the tumor (Figure 2, arrowheads). The deformity of the metatarsal bones showed the same Computed Tomographic (CT) finding as the one of the calcaneus (not shown). Foot MRI (1.5 Tesla Achi-va Philips, Netherlands, USA) reviewed a low signal intensity tumor on both T1 weighted (TR 465 msec, TE 12 msec, Thickness 3.5 mm, FOV 220 mm), and T2 weighted images (TR 2929 msec, TE 30 msec, Thickness 3.5 mm, FOV 220 mm) (Figures 3a and 3b), and well-enhancement on gadolinium-enhanced fat suppression T1 weighted sagittal image (TR 625.7 msec, TE 12 m sec, Thickness 3.5 mm, FOV 220 mm) (Figures 3c and 3d) in the left sole, from the calcaneus to the first metatarsal head. The tumor involved the adductor and the abductor hallucis muscle, the flexor digitorum longus and brevis tendons, the flexor digi-

torum brevis muscle and the quadratus plantae muscle (Figure 3d). Despite the tumor compression, the first to third metatarsal and the calcaneus bones showed no bone marrow edema. Considering patient clinical history and presentation and MRI findings, we initially suspected a fibroproliferative neoplasm like an aggressive fibromatosis. An open biopsy under local anesthesia was then performed. Histologically the lesion was benign fibroblastic spindle cell lesion with dense or loose collagen fibers. Cellularity was low and no mitotic figures were found (Figure 4). The tumor cells were positive for CD34 (Figure 5), whereas they were negative for α smooth muscle actin, desmin, HHHF35 and S100 protein. Although blood vessels including stag-horn like ones were indistinct, we made diagnosis of extrapleural solitary fibrous tumor (extrapleural SFT). We tried to recommend a complete surgical excision of the lesion but the patient conditions due to the Alzheimer-type senile dementia progressed and she was eventually sent to a mental hospital.



Figure 1: Anterio-posterior view of left foot X-ray. A soft tissue density mass is present under the first to third metatarsal bones. The second and third metatarsal bones show a severe deformity due to the soft tissue density mass. Widening between the first and second metatarsal bone is visualized (arrows).

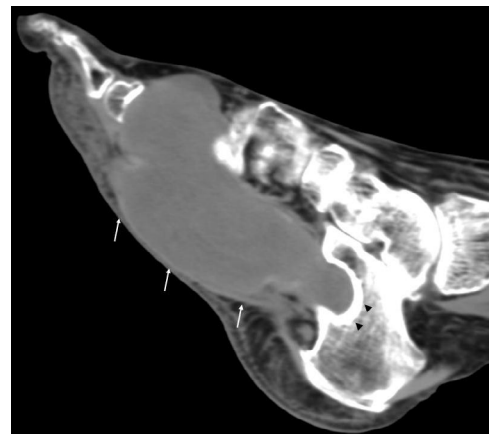


Figure 2: Foot CT (soft tissue window). A huge mass lesion is visualized in the sole (arrows). The mass lesion shows relatively homogenous low density with clear margin. The calcaneus is involved by the mass but the margin of it shows osteosclerotic change suggestive of slow growing tumor.

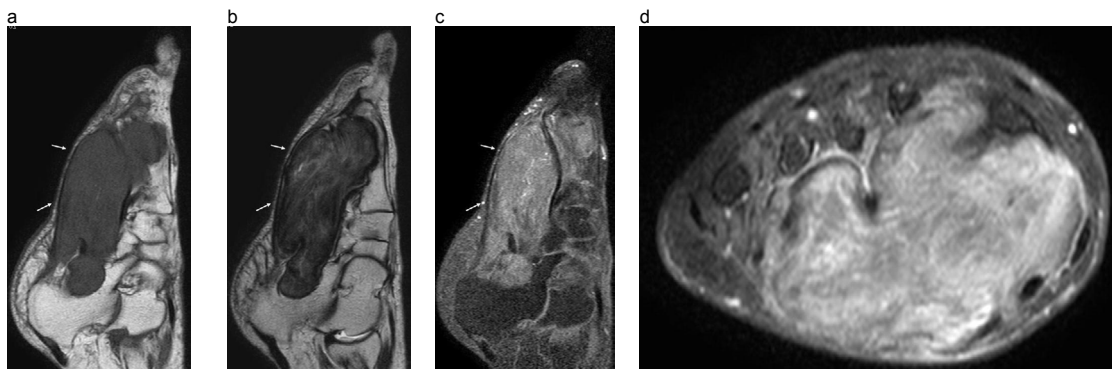


Figure 3: Foot MRI a) T1-weighted sagittal image, b) T2-weighted sagittal image, c) gadolinium-enhanced fat suppression T1-weighted sagittal image, d) gadolinium-enhanced fat suppression T1-weighted coronal image.
 a. The mass lesion in the sole shows low signal intensity (arrows) on T1-weighted sagittal image. The plantar fascia is present along the mass lesion without involvement. Subcutaneous fat tissue and the skin of the sole are intact. There are no bone marrow edemas in the calcaneus or other bones.
 b. The mass lesion shows heavy low signal intensity on T2-weighted sagittal image (arrows). The mass includes some high signal contents suggestive of myxoid or hyalinized in areas.
 c. The mass lesion is homogenously enhanced (arrows). Calcaneus and other bones are not enhanced.
 d. The mass lesion involves almost plantar muscles: an adductor hallucis muscle, an abductor hallucis muscle, long and short digital flexor tendons, a flexor digitorum brevis muscle and quadratus plantae muscle.

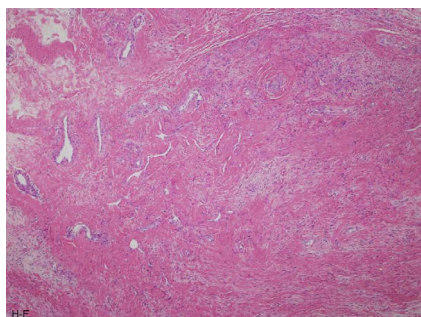


Figure 4: Hematoxylin and eosin stain (H-E stain). The tumor composes of small ovoid to spindle cells separated by thin bands of collagen fibers. Branching blood vessels and stromal hyalinization were visualized within it.



Figure 5: Immunohistochemical staining (CD34 staining). CD34 staining is positive. Both Desmin and S-100 protein staining are negative (not shown).

DISCUSSION

Extrapleural SFTs have been reported in several anatomical sites: nasal and paranasal sinus,⁵ spine,⁶ lung,⁷ mediastinum, pancreas,⁸ liver,⁹ kidney, retroperitoneal space,¹⁰ urinary bladder,¹¹ and extremities.¹² From the clinical point of view, an extrapleural SFT is usually a painless mass in the deep soft tissue without specific symptoms.¹³ Extrapleural SFT can show both benign and malignant behavior. From 10% to 15% of the tumors are malignant, occurring with more frequency in the cellular than in the fibrous forms.¹⁴ In the literature only few authors have reported SFT involving the extremities.^{12,15,16} Musyoki FN et al¹⁶ highlighted the orbits and the extremities (proximal extremities muscles and subcutaneous tissues) as the most common extrapleural SFT extrapleural location. Despite that, foot and ankle involvement is even less described. Lee JY et al¹⁴ reported the first case of an extrapleural SFT arising from the ankle in a 69-year-old female patient and treated by total excision. Kean CA et al¹⁷ described a rare manifestation of extrapleural SFT in a 55-year-old male patient affecting the medial right hallux: also in this case the treatment of choice was represented by the excision in toto. To the best of our knowledge, this is never say “the first” report of an extrapleural SFT in the foot affecting the plantar muscles. In addition, many authors reported that the majority of these tumors (80%) showed hypointense or isointense on T1-weighted image relative to muscle, and hypointense on T2-weighted image.¹²⁻¹⁹ On the other hand, Shin JH et al²⁰ reported that the extrapleural SFT in the buccal space showed hyperintense on T2-weighted image. Contrast enhanced MRI shows heterogeneous in as many as 82% of extrapleural SFT cases, and homogeneous enhancement effect in approximately 18%.^{16,18,19} In our case, the mass showed very low signal intensity on T2-weighted image. This peculiar aspect could be the result of 30 years of exerted compression on the extrapleural SFT which may have cause hemorrhage, reactive fibroplasia, and/or calcification. We didn’t detect any hemosiderin deposits or calcification on MRI and we therefore considered it as a reactive fibroplasia occurred on this tumor.

Considering the histo-pathological features, World Health Organization (WHO) classification of tumors of soft tis-

sue and bone has been revised since 2013.²¹ A notable point is what the extrapleural SFT has combined two soft tissue tumors called hemangiopericytoma and giant cell angiofibroma because their pathological findings are similar to the extrapleural SFT. We might have to reconsider MRI findings of the extrapleural SFT. Generally, an extrapleural SFT can vary in size, ranging from 1 cm to 30 cm.²² On light microscopy, a common histological feature of both pleural and extrapleural solitary fibrous tumor is a mixture of three components, namely, fibrous tissue, cellular components, and highly vascularized areas that consist of numerous dilated small to medium-sized blood vessels. On Immunohistochemical staining, positive CD34 and negative S-100 protein staining are typical for the extrapleural SFTs. The extrapleural SFT should be included in the differential diagnosis of extrapleural lesions in which MRI suggests fibrous content. Moreover, the differential diagnosis of extrapleural SFT includes fibromatosis, myofibroblastoma, metastasis of spindle cell carcinoma, low-grade fibromyxoid sarcoma and hemangioma.¹⁶ Clinical and imaging features of extrapleural SFTs also overlap with other fibrous tumors such as fibrous histiocytoma, fibrosarcoma and synovial sarcoma. These entities exhibit a dense fibrocollagenous matrix that can produce low signal intensity on T2-weighted MRI images, similar to extrapleural SFT. Despite our patient conditions did not allow any therapy, the treatment of choice for extrapleural SFT is total surgical excision, associated with long-term follow-up in order to early identify possible recurrence or malignant changes.¹⁴ In case of inoperable extrapleural SFT or incomplete excision, the use of radiotherapy or chemotherapy can increase the survival rate.¹⁶

CONCLUSION

SFT has been reported in a wide variety of extrapleural locations and is extremely rare in foot and ankle. Prolonged weight-bearing might cause bleeding and lead to a reactive fibroplasia, affecting the signal on MRI.

Diagnosis of extrapleural SFT is often challenging. In order to reach a proper diagnosis and treatment is essential to integrate a detailed patients’ clinical history and to perform a biopsy to collect cells for closer examination.

CONFLICTS OF INTEREST: None.

CONSENT

The patient has provided written permission for publication of the case details.

REFERENCES

- Klemperer P, Rabin CB. Primary neoplasm of the pleura: a report of five cases. *Arch Pathol.* 1931; 11: 385-412.
- de Perrot M, Fischer S, Brundler MA, Sekine Y, Keshavjee S. Solitary fibrous tumors of the pleura. *Ann Thorac Surg.* 2002; 74(1): 285-293. doi: [10.1016/S0003-4975\(01\)03374-4](https://doi.org/10.1016/S0003-4975(01)03374-4)
- Gold JS, Antonescu CR, Hajdu C, et al. Clinicopathologic correlates of solitary fibrous tumors. *Cancer.* 2002; 94: 1057. doi: [10.1002/cncr.10328](https://doi.org/10.1002/cncr.10328)
- Ginat DT1, Bokhari A, Bhatt S, Dogra V. Imaging features of solitary fibrous tumors. *AJR Am J Roentgenol.* 2011; 196(3): 487-495. doi: [10.2214/AJR.10.4948](https://doi.org/10.2214/AJR.10.4948)
- Weon YC, Kim EY, Kim HJ, Byun HS, Park K, Kim JH. Intracranial solitary fibrous tumors: imaging findings in 6 consecutive patients. *AJNR.* 2007; 28: 1466-1469. doi: [10.3174/ajnr.A0609](https://doi.org/10.3174/ajnr.A0609)
- Rodallec MH, Feydy A, Larousserie F, et al. Diagnostic imaging of solitary tumors of the spine: what to do and say. *RadioGraphics.* 2008; 28: 1019-1041. doi: [10.1148/rg.284075156](https://doi.org/10.1148/rg.284075156)
- Patsios D, Hwang DM, Chung TB. Intraparenchymal solitary fibrous tumor of the lung: an uncommon cause of a pulmonary nodule. *J Thorac Imaging.* 2006; 21: 50-53.
- Kwon HJ, Byun JH, Kang J, Park SH, Lee MG. Solitary fibrous tumor of the pancreas: imaging findings. *Korean J Radiol.* 2008; 9[Suppl]: S48-S51. doi: [10.3348/kjr.2008.9.s.s48](https://doi.org/10.3348/kjr.2008.9.s.s48)
- Nath DS, Rutzick AD, Sielaff TD. Solitary fibrous tumor of the liver. *AJR.* 2006; 187(2): W187-W190. doi: [10.2214/AJR.05.0294](https://doi.org/10.2214/AJR.05.0294)
- Nagasako Y, Misawa K, Kohashi S, Sano H. Solitary fibrous tumor in the retroperitoneum. *J Am Coll Surg.* 2004; 198: 322-323.
- Heinzelbecker J, Becker F, Pflugmann T, Friedmann J, Walz PH. Solitary fibrous tumour of the urinary bladder in a young woman presenting with haemodynamic-relevant gross haematuria. *Eur Urol.* 2008; 54: 1188-1191. doi: [10.1016/j.eururo.2008.07.057](https://doi.org/10.1016/j.eururo.2008.07.057)
- Akisue T, Matsumoto K, Kizaki T, et al. Solitary fibrous tumor in the extremity: case report and review of the literature. *Clin Orthop Relat Res.* 2003; 411: 236-244. doi: [10.1097/01.blo.0000065839.77325.b4](https://doi.org/10.1097/01.blo.0000065839.77325.b4)
- Abe S, Imamura T, Tateishi A, et al. Intramuscular solitary fibrous tumor: a clinicopathological case study. *J Comput Assist Tomogr.* 1999; 23: 458-462. Web site: http://journals.lww.com/jcat/Abstract/1999/05000/Intramuscular_Solitary_Fibrous_Tumor__A.24.aspx. Accessed May 17, 2016
- Lee JY, Kim DH, Seo KJ, Jung SN. A solitary fibrous tumor (cellular form) of the ankle. *J Foot Ankle Surg.* 2015. doi: [10.1053/j.jfas.2015.03.006](https://doi.org/10.1053/j.jfas.2015.03.006)
- Fukui T, Kawaguchi Y, Kawamoto T, et al. Solitary fibrous tumor arising in extremity: a report of two cases with 201-thallium scintigraphic and PET findings. *Cancer Ther.* 2008; 6B: 1017-1022.
- Musyoki FN, Nahal A, Powell TI. Solitary fibrous tumor: an update on the spectrum of extrapleural manifestations. *Skeletal Radiol.* 2012; 41(1): 5-13. doi: [10.1007/s00256-010-1032-z](https://doi.org/10.1007/s00256-010-1032-z)
- Kean CA, Moore BR, Nettles AM, Bui RP. Extrapleural solitary fibrous tumor of the foot a case report. *J Am Podiatr Med Assoc.* 2015; 105(6): 557-559. doi: [10.7547/13-126.1](https://doi.org/10.7547/13-126.1)
- Tateishi U, Nishihara H, Morikawa T, et al. Solitary fibrous tumor of the pleura: MR appearance and enhancement pattern. *J Comput Assist Tomogr.* 2002; 26: 174-179.
- Anders JO, Aurich M, Lang T, Wagner A. Solitary fibrous tumor in the thigh: review of the literature. *J Cancer Res Clin Oncol.* 2006; 132: 69-75. doi: [10.1007/s00432-005-0055-7](https://doi.org/10.1007/s00432-005-0055-7)
- Shin JH, Sung Y, Suh JH, Yang SO, Jeong K, Lee JH, Hwang JC. Solitary fibrous tumor in the buccal space: MR findings with pathologic correlation. *AJNR Am J Neuroradiol.* 2001; 22: 1890-1892. Web site: <http://www.ajnr.org/content/22/10/1890.full.pdf>. Accessed May 17, 2016
- Fletcher CDM, Bridge JA, Hogendoorn PCW, et al. *WHO Classification of Tumours of Soft Tissue and Bone.* Lyon, France: IARC Press; 2013.
- Cardillo G, Facciolo F, Cavazzana AO, et al. Localized (solitary) fibrous tumors of the pleura: an analysis of 55 patients. *Ann Thorac Surg.* 2000; 70: 1808-1812. doi: [10.1016/S0003-4975\(00\)01908-1](https://doi.org/10.1016/S0003-4975(00)01908-1)

Short Communication

*Corresponding author

Stefania Clemente, PhD

Medical Physicist

Department of Medical Physics

Azienda Ospedaliera Universitaria

Federico II Naples

Naples, Italy

E-mail: stefaniaclementesc@gmail.com

Volume 1 : Issue 2

Article Ref. #: 1000ROJ1107

Article History

Received: July 29th, 2016

Accepted: August 22nd, 2016

Published: August 23rd, 2016

Citation

Clemente S. Stereotactic body radiation therapy treatment for prostate cancer: From setup to delivery strategies. *Radiol Open J.* 2016; 1(2): 39-41. doi: [10.17140/ROJ-1-107](https://doi.org/10.17140/ROJ-1-107)

Copyright

©2016 Clemente S. This is an open access article distributed under the Creative Commons Attribution 4.0 International License (CC BY 4.0), which permits unrestricted use, distribution, and reproduction in any medium, provided the original work is properly cited.

Stereotactic Body Radiation Therapy Treatment for Prostate Cancer: From Setup to Delivery Strategies

Stefania Clemente, PhD*

Department of Medical Physics, Azienda Ospedaliera Universitaria Federico II Naples, Naples, Italy

INTRODUCTION

Stereotactic Body Radiation Therapy (SBRT) of prostate cancer has garnered increasing attention owing to its proposed low a/b value, which is close to 1.5 Gy.¹ Recent clinical data support the low value for a/b ratio as predicted by radiobiological models; hence, large doses per fraction should result in a higher probability of tumor control together with a reduced probability of complications for healthy tissue. In this paper, we focused on the technical parameters and treatment strategies adopted in the hypofractionation (HF) studies published in literature.

SETUP AND PREPARATION STRATEGIES

The effect of geometric uncertainties is known to be one of the major concerns in radiation dose delivery in prostate cancer.² These uncertainties are mostly due to patient setup errors and extensive motion of the rectum and bladder that is dependent on organ filling. In this regard, an augmented impact of geometric uncertainties is expected when high doses per fractions are adopted. This could occur because in HF treatments, any single targeting error causes a greater biologic impact by consistently underdosing the target organ at greater expense of the organs at risks (OARs).³ Several technological innovations have boosted the high-precision localization of the prostate during treatment, allowing the delivery of highly conformed dose fractions to a well-defined target with sharp dose fall-off towards the bladder and rectum.⁴ However, multiple technical parameters and operational variables can affect the correct localization of the prostate and the reproducibility of the procedures.⁵

Changes in patient posture were also of importance (e.g., relaxation of pelvic muscles). To reduce motion, specific patient positioning, immobilization strategies, controlled diet, and rectum/bladder filling have been practiced by different groups.⁶⁻⁸ The most commonly used patient treatment position was the supine. However, the optimal treatment position for the prostate remains controversial and inconclusive because several studies⁵ have reported advantages and disadvantages for both supine and prone approaches. An advantage of the prone position is that the irradiation dose to the rectum is reduced because the seminal vesicles (SV) are pulled away from the rectum.⁹ Moreover, the geometric relationship between the prostate and the pelvic bony anatomy is more consistent in the prone position and seems to be very important for centers using bony structure based positioning.¹⁰ Conversely, a disadvantage of the prone position is greater prostate motion compared with the supine position.¹¹ Additionally, the supine position is more comfortable for patients and more convenient for therapists than the prone position. Immobilization frames were routinely used to reduce the degree of spatial uncertainty secondary to positioning error. Pelvic vacuum cushions, thermoplastic sheets, foam agents, and/or leg, knee, ankle and foot supports were generally used in the reviewed studies. Despite reports that a whole-body cushion ensures more reproducibility,⁶ the usefulness of specific supports must be substantiated. For example, the use of a knee support during prostate irradiation, which prevents dorsal rectum shifts and prostate rotation at the apex around the left-right axis, decreases the dose delivered to the rectal wall.¹²

Displacements of the prostate relative to the radiation beams occur not only as a result of patient positioning but also owing to different filling levels and pressures from the bladder and rectum. Graf et al¹³ reported reduced prostate motion when patients were appropriately instructed regarding constant bladder and rectum filling. In most of the selected HF studies, the bladder volume was kept constant by having the patient empty the bladder and drinks a known amount of water before the simulation and treatment. Different strategies were adopted for the rectum, for which filling is more difficult to control. Frequently, a rectal enema was performed in patients treated with extremely high frequency (EHF) regimens. In fact, several studies showed a decrease in the interfraction prostate displacement with a consequent reduction in the target margin when an enema was used.^{14,15} None of the drugs or compounds delivered was shown in the current literature to be useful in preventing or mitigating acute damage to healthy tissues. The use of a rectal balloon, which positively influences intrafraction prostate stability, was sporadic. The use of tissue spacers in the region between the prostate and the anterior rectal wall has never been referenced. However, a reduced variability in the data regarding bladder toxicity, especially late toxicity, was observed in patients who received preparation, this indicates a more accurate prediction of the expected toxicity when assessed for a lower anatomical inter patient variability.

IMAGING STRATEGIES

The use of computed tomography/magnetic resonance imaging (CT/MRI) image fusion for more precise target volume identification in prostate cancer patients was reported. Hentschel et al¹⁶ reported that CT scans overestimate prostate volume by 35% compared with MRI. In particular, they found that the mean area defined by CT imaging was larger than the area defined by MRI, mainly at the base and the apex of the prostate. However, in the segmentation process, it is necessary to take into account the prostate swelling that occurs during treatment.¹⁷ In a recent study performed by Gunnlaugsson et al,¹⁸ the adoption of an EHF regimen showed a significant increase in prostate shape and size of 14% at the middle of treatment (Equivalent dose in 2 Gy fractions Z 33 Gy) and 9% at the end of treatment (Equivalent dose in 2 Gy fractions Z 67 Gy). This trend differs from the conventional fractionation trend.¹⁹

IMAGE GATED RADIOTHERAPY STRATEGIES

The daily or random prostate localization timing were done using several different technologies, including transabdominal US, x-ray portal imaging, and kilo-voltage and mega-voltage cone-beam computed tomography (CBCT). With these technologies, patient localization uses bony anatomy, implanted fiducials (seeds or electromagnetic transponders), or soft-tissue images. EHF studies reported mostly a prostate alignment performed with implanted fiducial markers. Intermodality shifts between the different technologies seem comparable, as reported by Mayyas et al.²⁰ Among the methods, localization using markers results in the least interuser disagreement compared with using

anatomy or soft tissues.^{14,21} Different authors have reported that the choice of imaging frequency and timing are key components in delivering the desired dose while reducing the associated overhead, such as imaging dose, preparation, and processing time.²²

ADAPTIVE STRATEGIES

No adaptive strategy was adopted in the published EHF studies. Several groups have conducted research in the pelvic region with different adaptive approaches.^{23,24} One notable method that could be applied to HF regimens is the so called “*plan of the day*” approach.²⁵ In this strategy, a multiple-plan library was generated before the treatment course from weekly serial 6-8 CT datasets from 4 patients. During each fraction, a daily plan was manually chosen from the library according to the patient’s daily anatomy. Chen et al²⁵ reported an excellent target coverage using a similar approach, with the dose delivered to the OARs being only slightly increased.

CONCLUSIONS

Recent clinical data support a low value for a/b ratio as predicted by radiobiological models; hence, large doses per fraction should result in a higher probability of tumor control together with a reduced probability of complications for healthy tissue. The evaluation of the cost-effectiveness of the treatment, it is mandatory to also consider the associated morbidity. This paper is an overview on technical parameters and delivery strategies to be taken as a guideline for HF radiotherapy treatments.

REFERENCES

1. Miralbell R, Roberts SA, Zubizarreta E, et al. Dose-fractionation sensitivity of prostate cancer deduced from radiotherapy outcomes of 5,969 patients in seven international institutional datasets: a/b Z 1.4 (0.9-2.2). *Gy. Int J Radiat Oncol Biol Phys.* 2012; 82: 17-24. doi: [10.1016/j.ijrobp.2010.10.075](https://doi.org/10.1016/j.ijrobp.2010.10.075)
2. Rosenschold PM, Desai NB, Oh JH, et al. Modeling positioning uncertainties of prostate cancer external beam radiation therapy using pre-treatment data. *Radiother Oncol.* 2014; 110: 251-255. doi: [10.1016/j.radonc.2013.12.010](https://doi.org/10.1016/j.radonc.2013.12.010)
3. Craig T, Moiseenko V, Battista J, et al. The impact of geometric uncertainty on hypofractionated external beam radiation therapy of prostate cancer. *Int J Radiat Oncol Biol Phys.* 2003; 57: 833-842. doi: [10.1016/S0360-3016\(03\)00638-2](https://doi.org/10.1016/S0360-3016(03)00638-2)
4. Schiller K, Petrucci A, Geinitz H, et al. Impact of different setup approaches in image-guided radiotherapy as primary treatment for prostate cancer: A study of 2940 setup deviations in 980 MVCTs. *Strahlenther Onkol.* 2014; 190: 722-726. doi: [10.1007/s00066-014-0629-x](https://doi.org/10.1007/s00066-014-0629-x)
5. Butler WM, Merrick GS, Reed JL, et al. Intrafraction displacement of prone versus supine prostate positioning monitored by

- real-time electromagnetic tracking. *J Appl Clin Med Phys*. 2013; 14(2): 4141. doi: [10.1120/jacmp.v14i2.4141](https://doi.org/10.1120/jacmp.v14i2.4141)
6. White P, Yee CK, Shan LC, et al. A comparison of two systems of patient immobilization for prostate radiotherapy. *Radiat Oncol*. 2014; 9: 29. doi: [10.1186/1748-717X-9-29](https://doi.org/10.1186/1748-717X-9-29)
7. Valdagni R, Rancati T. Reducing rectal injury during external beam radiotherapy for prostate cancer. *Nat Rev Urol*. 2013; 10: 345-357. doi: [10.1038/nrurol.2013.96](https://doi.org/10.1038/nrurol.2013.96)
8. Bell LJ, Cox J, Eade T, et al. The impact of rectal and bladder variability on target coverage during post-prostatectomy intensity modulated radiotherapy. *Radiother Oncol*. 2014; 110: 245-250. doi: [10.1016/j.radonc.2013.10.042](https://doi.org/10.1016/j.radonc.2013.10.042)
9. O'Neill L, Armstrong J, Buckney S, et al. A phase II trial for the optimization of treatment position in the radiation therapy of prostate cancer. *Radiother Oncol*. 2008; 88: 61-66. doi: [10.1016/j.radonc.2008.03.023](https://doi.org/10.1016/j.radonc.2008.03.023)
10. Liu B, Lerma FA, Patel S, et al. Dosimetric effects of the prone and supine positions on image guided localized prostate cancer radio-therapy. *Radiother Oncol*. 2008; 88: 67-76. doi: [10.1016/j.radonc.2007.11.034](https://doi.org/10.1016/j.radonc.2007.11.034)
11. Bayley AJ, Catton CN, Haycocks T, et al. A randomized trial of supine vs. prone positioning in patients undergoing escalated dose conformal radiotherapy for prostate cancer. *Radiother Oncol*. 2004; 70: 37-44. doi: [10.1016/j.radonc.2003.08.007](https://doi.org/10.1016/j.radonc.2003.08.007)
12. Steenbakkers RJ, Duppen JC, Betgen A, et al. Impact of knee support and shape of tabletop on rectum and prostate position. *Int J Radiat Oncol Biol Phys*. 2004; 60: 1364-1372. doi: [10.1016/j.ijrobp.2004.05.060](https://doi.org/10.1016/j.ijrobp.2004.05.060)
13. Graf R, Boehmer D, Nadobny J, et al. Appropriate patient instructions can reduce prostate motion. *Radiat Oncol*. 2012; 7: 125. doi: [10.1186/1748-717X-7-125](https://doi.org/10.1186/1748-717X-7-125)
14. Seo YE, Kim TH, Lee KS, et al. Interfraction prostate movement in bone alignment after rectal enema for radiotherapy. *Korean J Urol*. 2014; 55: 23-28. doi: [10.4111/kju.2014.55.1.23](https://doi.org/10.4111/kju.2014.55.1.23)
15. Fiorino C, Di Muzio N, Broggi S, et al. Evidence of limited motion of the prostate by carefully emptying the rectum as assessed by daily MVCT image guidance with helical tomotherapy. *Int J Radiat Oncol Biol Phys*. 2008; 71: 611-617. doi: [10.1016/j.ijrobp.2008.01.048](https://doi.org/10.1016/j.ijrobp.2008.01.048)
16. Hentschel B, Oehler W, Strauss D, Ulrich A, Malich A. Definition of the CTV prostate in CT and MRI by using CT-MRI image fusion in IMRT planning for prostate cancer. *Strahlenther Onkol*. 2011; 187: 183-190. doi: [10.1007/s00066-010-2179-1](https://doi.org/10.1007/s00066-010-2179-1)
17. Jonsson JH, Karlsson MG, Karlsson M, et al. Treatment planning using MRI data: An analysis of the dose calculation accuracy for different treatment regions. *Radiation Oncol*. 2010; 5: 62. doi: [10.1186/1748-717X-5-62](https://doi.org/10.1186/1748-717X-5-62)
18. Gunnlaugsson A, Kjellén E, Hagberg O, Thellenberg-Karlsson C, Widmark A, Nilsson P. Change in prostate volume during extreme hypo-fractionation analysed with MRI. *Radiation Oncol*. 2014; 9: 22. doi: [10.1186/1748-717X-9-22](https://doi.org/10.1186/1748-717X-9-22)
19. Sanguineti G, Marcenaro M, Franzone P, et al. Neoadjuvant androgen deprivation and prostate gland shrinkage during conformal radio-therapy. *Radiother Oncol*. 2003; 66: 151-157. doi: [10.1016/S0167-8140\(03\)00031-8](https://doi.org/10.1016/S0167-8140(03)00031-8)
20. Mayyas E, Chetty IJ, Chetvertkov M, et al. Evaluation of multiple image-based modalities for image-guided radiation therapy (IGRT) of prostate carcinoma: A prospective study. *Med Phys*. 2013; 40: 041707. doi: [10.1118/1.4794502](https://doi.org/10.1118/1.4794502)
21. Johnston ML, Vial P, Wiltshire KL, et al. Daily online bony correction is required for prostate patients without fiducial markers or soft-tissue imaging. *Clin Oncol (R Coll Radiol)*. 2011; 23: 454-459. doi: [10.1016/j.clon.2011.02.013](https://doi.org/10.1016/j.clon.2011.02.013)
22. Zhang P, Hunt M, Happersett L, et al. Incorporation of treatment plan spatial and temporal dose patterns into a prostate intrafractional motion management strategy. *Med Phys*. 2012; 39: 5429-5436. doi: [10.1118/1.4742846](https://doi.org/10.1118/1.4742846)
23. Qi P, Pouliot J, Roach M, et al. Offline multiple adaptive planning strategy for concurrent irradiation of the prostate and pelvic lymph nodes. *Med Phys*. 2014; 41: 021704. doi: [10.1118/1.4860663](https://doi.org/10.1118/1.4860663)
24. Kim J, Kumar S, Liu C, et al. A novel approach for establishing benchmark CBCT/CT deformable image registrations in prostate cancer radiotherapy. *Phys Med Biol*. 2013; 58(22): 8077-8097. Web site: <http://iopscience.iop.org/article/10.1088/0031-9155/58/22/8077/meta>. Accessed July 28, 2016
25. Chen W, Gemmel A, Rietzel E. A patient-specific planning target volume used in 'plan of the day' adaptation for interfractional motion mitigation. *J Radiat Res*. 2013; 54(Suppl 1): i82-i90. doi: [10.1093/jrr/rrt070](https://doi.org/10.1093/jrr/rrt070)

Systematic Review

*Corresponding author
Dejian Qiu

Department of Medical Imaging
and Radiation Sciences
Monash University
Clayton, Victoria, Australia
Tel. (61)490215223; (65)82283580
E-mail: dqiu9@student.monash.edu;
qiudejian68@gmail.com

Volume 1 : Issue 2

Article Ref. #: 1000ROJ1108

Article History

Received: July 22nd, 2016

Accepted: August 23rd, 2016

Published: August 24th, 2016

Citation

Qiu D, Seeram E. Does iterative reconstruction improve image quality and reduce dose in computed tomography? *Radiol Open J.* 2016; 1(2): 42-54. doi: [10.17140/ROJ-1-108](https://doi.org/10.17140/ROJ-1-108)

Copyright

©2016 Qiu D. This is an open access article distributed under the Creative Commons Attribution 4.0 International License (CC BY 4.0), which permits unrestricted use, distribution, and reproduction in any medium, provided the original work is properly cited.

Does Iterative Reconstruction Improve Image Quality and Reduce Dose in Computed Tomography?

Dejian Qiu*; Euclid Seeram, PhD, MSc, BSc, FCAMRT

Department of Medical Imaging and Radiation Sciences, Monash University, Clayton, Victoria, Australia

ABSTRACT

The Filtered Back Projection (FBP) algorithm has been the standard algorithm for image reconstruction in computed tomography (CT) for many years, but it creates possible streak artifacts and a notable increase in image noise when radiation dose is reduced exceedingly. With technological advancement and increased computational capacities in workstations, iterative reconstruction (IR) algorithms have re-emerged as a potential alternative. The purpose of this review is to establish if there is a general consensus that IR algorithms faithfully reduce radiation dose and improve image quality in CT in comparison with the FBP algorithm. A systematic review of the literature from 2012 to 2015 was conducted using Ovid MEDLINE and PubMed databases, as well as various well-known journals such as the *American Journal of Roentgenology*, *European Journal of Radiology*, *Physica Medica* and the *Korean Journal of Radiology*. A total of 57 articles were categorized as either synopsis articles or performance evaluation clinical studies, where the latter was further divided into 6 sub-categories according to the type of IR algorithm examined. The results show that the use of IR algorithms reduces objective image noise, and at least preserves spatial resolution and low contrast detectability, even when dose is reduced. The findings are also applicable to specific patient groups, such as pediatrics and obese patients. In conclusion, there is a general consensus that IR algorithms can faithfully reduce radiation dose and improve image quality in CT in comparison with the FBP algorithm.

KEYWORDS: Iterative Reconstruction (IR); Computed Tomography (CT); Filtered Back Projection (FBP); Radiation dose; Image quality.

ABBREVIATIONS: FBP: Filtered Back Projection; CT: Computed Tomography; IR: Iterative Reconstruction; ASIR: Adaptive Statistical Iterative Reconstruction; MBIR: Model-Based Iterative Reconstruction; IRIS: Image Reconstruction in Image Space; SAFIRE: Sinogram Affirmed Iterative Reconstruction; AIDR: Adaptive Iterative Dose Reduction; ASiR: Adaptive Statistical Iterative Reconstruction; BMI: Body Mass Index.

INTRODUCTION

Rapid technological advancements in imaging techniques, such as the development of multi-detector computed tomography, has resulted in a substantial rise in demand for CT examinations as a key diagnostic imaging modality over the past decade.¹⁻³ While the diagnostic benefits of CT are well-documented, the associated risks of increased exposure to ionizing radiation such as radiation-induced cancer has become an area of increasing concern.⁴ Radiation exposure from CT accounts for approximately two-thirds of all medical-related radiation worldwide, and recent studies have cited associated cumulative cancer risk from CT to be as high as 1.5%.⁵ Several techniques, such as automatic tube current modulation, automatic tube voltage selection and dynamically adjustable z-axis beam collimation, have been employed to reduce CT-associated radiation dose, but the amount of dose reduction is limited if the FBP algorithm is used for image reconstruction.^{6,7} The FBP algorithm has been the standard algorithm for im-

age reconstruction in CT for many years, but it poses the limitation of producing possible streak artifacts and a notable increase in image noise level if radiation dose is reduced exceedingly.⁸

The re-emergence of IR techniques in CT recently offers a potential alternative that allows a reduction in radiation dose while preserving image quality.¹ IR algorithms were first considered for use in early CT scanning back in the 1970's, but were deemed unsuitable for clinical use due to the need for high computational capacities in workstations and long reconstruction times.⁹ However, with the advancement of computer technology and improvements in computational capacities, IR has now become a realistic option for use in CT in clinical settings, and various CT manufacturers currently offer a variety of IR algorithms. For example, while GE Healthcare offers Adaptive Statistical Iterative Reconstruction (ASIR) and Model-Based Iterative Reconstruction (MBIR), Siemens Healthcare offers Iterative Reconstruction in Image Space (IRIS) and Sinogram Affirmed Iterative Reconstruction (SAFIRE). On the other hand, other major CT manufacturers such as Philips Healthcare and Toshiba America Medical Systems, offer iDose and Adaptive Iterative Dose Reduction (AIDR) respectively.^{1,9}

Several studies done between 2012 and 2015 have shown that the use of IR algorithms do indeed aid in reducing radiation dose and improving image quality in CT examinations when compared to the FBP algorithm.^{6,10} However, there has yet to be any known review published on related studies to establish if this is a shared consensus within the medical imaging community, and whether the outcomes differ for different types of CT examinations and patients. This is especially crucial, as most of these studies often employ the use of IR algorithms from only one or two CT manufacturers, with the focus on a single specific type of CT examination.

The primary aim of this literature review is to establish if there is a general consensus that IR algorithms faithfully reduce radiation dose and improve image quality in CT in comparison with the FBP algorithm. The secondary aims are to provide an overview of the limitations of the FBP algorithm, outline the advantages of IR algorithms, as well as to explain how IR algorithms work in general and present examples of available IR algorithms from CT vendors.

MATERIAL AND METHODS

An online search was conducted for literature published from 2012 to 2015 using PubMed and Ovid MEDLINE databases. A subsequent search was also performed in various well-known journals, such as the *American Journal of Roentgenology*, *European Journal of Radiology*, *Physica Medica* and the *Korean Journal of Radiology*. Only articles that were published within the last four years were included, in view of the rapid development of technology in CT. The search strategy involved the use of three primary keywords, which were “iterative reconstruction (IR)”, “computed tomography (CT)” and “filtered back projec-

tion (FBP)”, in addition to five secondary keywords, namely “radiation dose”, “image quality”, “image noise”, “advantages” and “limitations”. Each of the searches consisted of a combination of one primary keyword and one secondary keyword. The articles that were collected provided information on the various types of IR algorithms, as well as their effects on radiation dose and image quality when used in place of the FBP algorithm in CT image reconstruction.

Articles from the initial search results were screened in detail and assessed for relevance. Studies that were included in this review were peer-reviewed and belonged to two main categories of literature, namely synopsis articles that provided general information about IR and FBP algorithms, and controlled experimental studies that measured the comparative effects of IR algorithms on radiation dose and image quality against the FBP algorithm. Literature that were not available in the English language were excluded for review, in addition to those that were physically unobtainable from library databases. Papers evaluating the use of IR algorithms in nuclear medicine were also excluded as they were considered to be beyond the scope of this literature review.

RESULTS

The initial searches performed using the two databases returned a total of 535 articles after removing duplicate results. After applying the exclusion criteria, 221 papers were considered to be clinically relevant for review. However, due to the number of similarities in the types and outcomes of relevant studies, only articles with the most informative and representative findings were included for review. As such, 57 articles were eventually analyzed in this review. Articles were categorized as either synopsis articles or clinical studies evaluating the performance of various IR algorithms. Articles that belonged to the latter were further sub-divided into 6 categories according to the types of IR algorithms used in these studies, since algorithms offered by different manufacturers may have varying extents of influence on dose and quality of images when used for image reconstruction.

Synopsis Articles

Twenty-two synopsis articles were analyzed in this review. These articles provided an insight into the image reconstruction process of FBP and IR algorithms, as well as an overview of IR algorithms available from CT vendors and the differences between each algorithm.

Limitations of the FBP Algorithm in CT Image Reconstruction

It is essential to first comprehend the image reconstruction process and limitations of the FBP algorithm, so as to recognize the advantages offered by IR algorithms. Various articles provided an overview of the basic principles behind the FBP reconstruction algorithm.^{8,9,11,12}

The FBP algorithm is described as an analytical image reconstruction method which consists of 2 main components, namely back-projection and convolution filtering. The back-projection process involves the summation of multiple back-projections of projection data obtained with the x-ray source at different angles, until the complete image is reconstructed.⁹ This however results in a blurred image, so convolution filtering using filter kernels is applied to each set of projection data before back-projection to improve spatial resolution and contrast.^{9,12} The reconstruction process of the FBP algorithm is illustrated in Figure 1.

Application of the convolution filters to obtain a sharper image however, also increases the amount of noise in images. The limitations of the FBP algorithm become even more pronounced when it is used in low-dose CT examinations, since an inverse correlation exists between radiation dose and image noise.¹² These limitations in image quality can be primarily attributed to the underlying assumptions about scanner geometry that the FBP algorithm is based on, which are mostly deviant from reality.¹¹ These assumptions include a pencil x-ray beam, the x-ray focal spot being a point source, a lack of consideration for the shape and size of detector cells and voxels, as well as neglecting the image noise resulting from Poisson statistical variations of x-ray photons.⁸ As a result, there is a need for alternative algorithms that model the CT system more accurately, in order to produce diagnostic images while maintaining a low dose in CT examinations.

Advantages of IR Algorithms and How They Work

A number of articles have also identified the ability to reduce image noise while preserving spatial resolution and image contrast, even at lower tube currents in reduced-dose examinations, as the main advantage offered by IR algorithms.^{6,12,13} In addition, IR algorithms can help reduce artifacts caused by metallic implants, as well as those resulting from photon starvation and beam-hardening effects.¹ It is therefore essential to understand

how IR algorithms work in general, since it provides the basis to comprehending why IR algorithms are able to offer these advantages.

The iterative reconstruction process can generally be divided into a few steps. Firstly, the measured projection data is acquired, before it is reconstructed using the standard FBP algorithm to produce an initial image estimate. This initial image estimate is then forward-projected to create a simulated projection data, which is subsequently compared with the measured projection data. The difference between the 2 sets of data is then determined to generate an updated image that will be back-projected on the current CT image, to keep the difference between the current CT image and the measured projection data to a minimum. This iteration process is then repeated several times in what is known as the “iterative loop”, until the difference is considered to be sufficiently minimal. The output is the resultant volumetric image after the termination of the iterative cycle.^{1,6,9} The entire iterative reconstruction process is illustrated in Figure 2. A comparison of images reconstructed using the FBP and IR algorithms is shown in Figure 3.

Examples of IR Algorithms

There are currently several IR algorithms available from the 4 major CT vendors, namely GE Healthcare, Siemens Healthcare, Philips Healthcare, and Toshiba Medical Systems. Algorithms from the respective vendors differ significantly in their approaches within the image reconstruction process, but share the common objective of improving image quality and reducing noise, especially in low-dose CT procedures. The various examples of IR image reconstruction techniques are listed in Table 1. As these algorithms are now part of standard image reconstruction for CT, only a brief overview of algorithms from GE Healthcare and Siemens Healthcare will be provided to illustrate the differences between various IR algorithms. A summary of the key differences between IR algorithms offered by various major CT vendor is presented in Table 2.

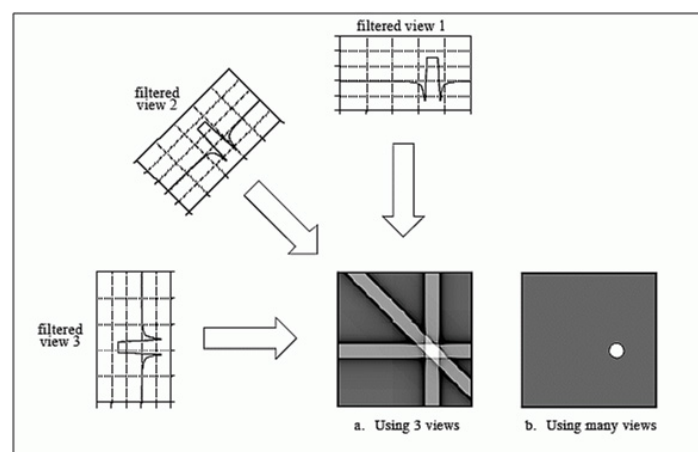


Figure 1: The image reconstruction process of the FBP algorithm. Each set of projection data, taken at different angles, undergoes convolution filtering before back-projection. This removes the blurring that would result from simple backprojection without filtering.²

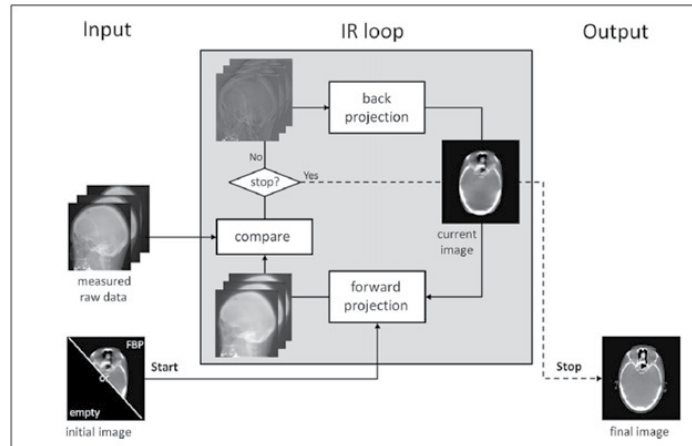


Figure 2: An illustration of the iterative reconstruction process. Forward projection of the CT image reconstructed with standard FBP algorithm creates an initial image estimate, which is then compared with the measured raw data. Comparisons generate an updated image that is back-projected to the current CT image until the difference is minimized. The final volumetric image is produced when the iterative loop terminates after multiple cycles of iteration.¹

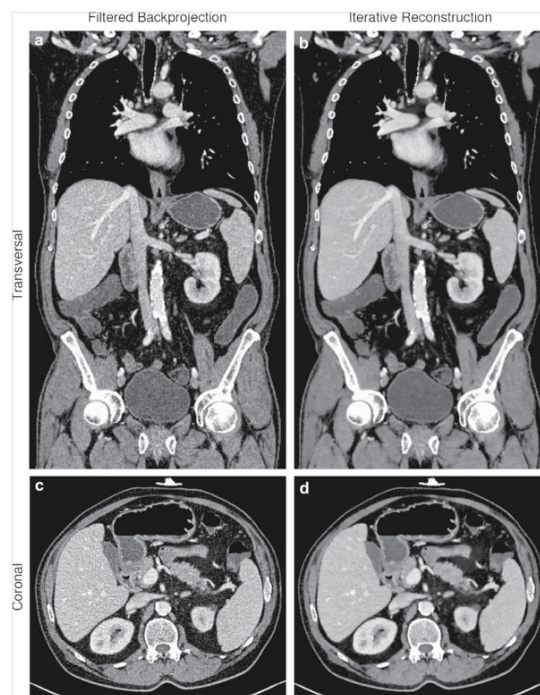


Figure 3: Comparison of image quality of images reconstructed using FBP and IR algorithms.¹

Acronym	IR Algorithm	Vendor	Year
ASiR	Adaptive Statistical Iterative Reconstruction	GE Healthcare	2008
Veo (MBiR)	Veo Model-Based Iterative Reconstruction	GE Healthcare	2009
ASiR-v	ASiR-v	GE Healthcare	2013
IRIS	Image Reconstruction In Image Space	Siemens Healthcare	2009
SAFIRE	Sonogram-Affirmed Image Reconstruction	Siemens Healthcare	2010
ADMIRE	Advanced Modeled Oterative Reconstruction	Siemens Healthcare	2014
IDose ⁴	IDose ⁴	Philips	2009
AIDR	Adaptive Iterative Dose Reduction	Toshiba Medical System	2010
AIDR 3D	Adaptive Iterative Dose Reduction 3-Dimensional	Toshiba Medical System	2012

Table 1: Examples of IR algorithms from major CT vendors.

IR Algorithm	Key features
ASiR	1 st generation hybrid IR algorithm blended in 10% increments with traditional FBP according to user preference Based on advanced statistical noise and object modeling
Veo (MBIR)	Fully-iterative model-based IR algorithm Based on advanced modeling of system optics , in addition to statistical noise, object and physics modeling Allows for further noise reduction but involves long processing times
ASIR-V	Next generation of the ASiR algorithm Based on advanced physics modeling , in addition to statistical and object modeling Improved performance over ASiR, with shorter processing times as compared to MBIR
IRIS	1 st generation IR algorithm Iterative corrections are performed in the image space on a virtual "master image", instead of on the raw data Allows for fast processing times , but limited in removal of image artifacts
SAFIRE	Involves 2 different iterative correction loops Corrections first performed on the raw data to remove image artifacts, before noise reduction in the image space
ADMIRE	Next generation of the SAFIRE algorithm Weighted FBP is introduced into the first iteration loop for improved artifact removal, in addition to advanced statistical noise modeling
iDose ⁴	Iterative corrections performed on both projection data and in the image space Statistical noise modeling applied to denoise image in projection data, then compared to a noiseless ideal anatomical model in image space to avoid artificial appearance of images
AIDR	Iterative corrections only performed in the image domain and not on the raw projection data Fast processing times but limited in overall dose reduction
AIDR 3D	Next generation of the AIDR algorithm Iterative corrections performed in both the raw data and image domains Based on statistical noise, object and system optics modeling Weighted blending added to avoid artificial appearance of images

Table 2: Key differences between IR algorithms from major CT vendors.

Adaptive statistical iterative reconstruction (ASiR) is a hybrid IR algorithm by GE Healthcare, and was the first IR algorithm available among vendors.¹⁴ The ASiR model accounts for changes in the projection data measurements due to statistical distribution of photons, and the iterative process involves comparison of estimated pixel values and predicted ideal values until both values converge.^{15,16} ASiR is usually blended with traditional FBP in 10% increments. GE healthcare later introduced Veo, or model-based iterative reconstruction (MBIR) in 2009, which is a complex and fully iterative reconstruction algorithm.⁹ In addition to statistical noise modelling, MBIR uses a model that accounts for the system optics, in order to achieve further noise reduction.¹⁷⁻¹⁹ Increased complexity of the algorithm however means that a longer processing time is needed, hence MBIR is used less extensively in the clinical setting.²⁰ ASIR-V, known as the next generation of ASiR, was then introduced in late 2013 with comparable clinical performance to MBIR but shorter processing times.

Siemens Healthcare on the other hand, introduced image reconstruction in image space (IRIS) in 2009, a unique algorithm that does not involve forward and back projections onto the raw image data.⁹ The IRIS algorithm creates a virtual image from the raw data, and the iterative corrections to reduce image noise are performed on the virtual image itself in the image space, allowing for faster processing times.^{21,22} Eliminating the need for multiple forward and back projections however also meant that the IRIS algorithm is solely for the purpose of noise reduction, and not for the removal of potential image artifacts.²³

Siemens Healthcare later introduced sinogram affirmed iterative reconstruction (SAFIRE) in 2010, and it differs from IRIS in that the iterative corrections are performed on the raw data, before conversion into the image space.²⁴ This allows for noise reduction, artifact removal and reduced processing time.²⁵ Advanced modeled iterative reconstruction (ADMIRE), the third-generation of IR technique by Siemens Healthcare, was

finally approved for use in 2014 with additional algorithm processing steps such as the use of weighted FBP in the iterative loop, allowing for improved artifact removal in produced images.⁹

Clinical Studies Evaluating the Performance of IR Algorithms

These studies were performed with the use of either phantom or patient models, and examined the performance of IR algorithms in terms of noise reduction, dose reduction and improvement in image quality when compared with the FBP algorithm. Thirty-five articles were reviewed, and the results are discussed in 6 sub-sections according to the type of IR algorithm that was used. A summary of the performance of various IR algorithms is listed in Table 3.

Performance of ASiR and ASIR-V Algorithms

Various studies comparing the ASiR and FBP algorithms demonstrated significant reductions in radiation dose and preservation of image quality with the use of the ASiR algorithm. Two of such studies compared the use of the FBP protocol against 40% ASiR protocols at similar and lower tube potentials.^{26,27} The first study showed a 33.8% (3.21 mSv *versus* 4.85 mSv)

reduction in effective dose at similar tube voltages of 120 kV, in chest CT angiography examinations of patients with pulmonary embolism.²⁷ Meanwhile, the latter study found no notable differences in overall image quality between FBP and 40% ASiR images with reduced dose, although significant improvement was noted in the subjective assessment of noise level.²⁶ Image quality was both subjectively and objectively measured based on various indicators, such as image sharpness, noise, artefacts, signal-to-noise ratio (SNR), contrast-to-noise ratio (CNR), visibility of small structures and overall diagnostic confidence.

Similar results were reported in specific patient groups such as pediatrics and obese patients. A pediatric study for children under the age of 12 found that the use of a 30% ASiR algorithm led to a dose reduction of 46.4% (3.7 mGy *versus* 6.9 mGy) for chest CT and 38.2% (5.0 mGy *versus* 8.1 mGy) in abdominal CT examinations.²⁸ Another study was conducted on obese patients weighing 91 kg and above, and reported an average dose reduction of 31.5% (13.5 *versus* 19.7) with the use of a 30% ASiR algorithm.²⁹ Both subjective and objective image noise were significantly lower with ASiR in both studies, while diagnostic acceptability and image sharpness of ASiR images were comparable to FBP images. A visual comparison of the image quality of FBP and ASiR images is shown in Figure 4,

IR Algorithm	Performance of algorithms
ASiR	30% and 40% blended ASiR algorithms were most commonly used Dose reductions of up to 46.4% reported in CT examinations of the chest or abdomen Both subjective and objective image noise were lower with the use of ASiR , with comparable diagnostic acceptability and image sharpness to FBP images Results are also similar in both pediatrics and obese patients Use of a high blend (>50%) can result in smoothed appearance which decreases visibility of small structures
Veo (MBIR)	Reported better dose reduction and image quality improvement than older-generation IR algorithms such as ASiR Not used extensively in clinical settings due to long processing times Use of MBIR can result in pixelated blotchy appearance and smoothed appearance , resulting in suboptimal resolution of thin bone structures
ASIR-V	50% blended ASIR-V algorithm reported to be the preferred blending weightage to obtain best spatial resolution Significantly superior to ASiR and FBP in noise reduction (up to 61.3%) and improvement in contrast-to-noise ratio.
IRIS	Variable results reported on the effects of IRIS on image quality and dose reduction Use of the IRIS algorithm definitively improved or preserved objective image noise , but subjective image quality reported to deteriorate with use of IRIS in 3 studies Poorer subjective image quality attributed to poorer image contrast and sharpness One study suggested the use of IRIS only allows approximately up to 20.4% dose reduction
SAFIRE	Use of SAFIRE at lower doses generally resulted in superior or similar image quality to full-dose FBP images Amount of improvement in image quality with the use of SAFIRE is lesser in patients of heavier weights (>75kg) or obese patients
ADMIRE	Use of ADMIRE improved or at least preserved low-contrast detectability in images, with significant dose reduction of up to 80% when compared to FBP images
iDose ⁴	Superior image quality reported in iDose ⁴ images when compared to FBP images when performed at the same dose level Variable results reported in terms of subjective quality when comparing iDose ⁴ images acquired at lower doses to standard-dose FBP images
AIDR	Reported noise reduction of up to 31% and estimated dose reduction of 52%
AIDR 3D	Superior noise reduction of up to 37.5% in abdominal examinations, with increased noise reduction with increased size of patients

Table 3: Performances of IR algorithms from major CT vendors.

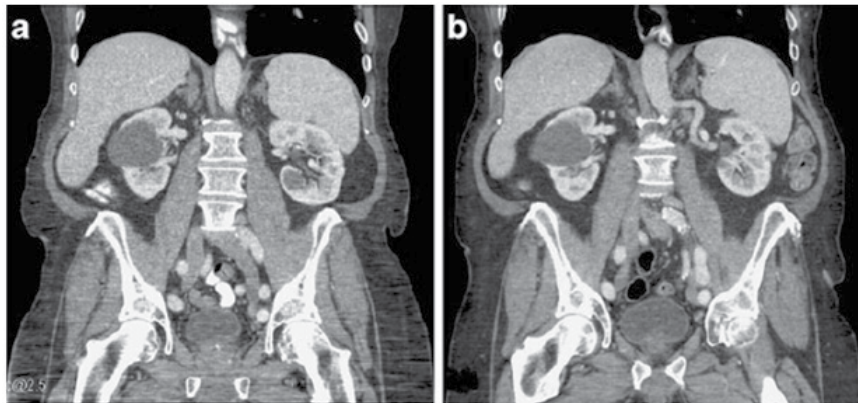


Figure 4: A comparison of image quality of coronal images reconstructed with FBP (a) and ASiR (b) algorithms in the imaging of a right renal cyst. The image reconstructed using the ASiR algorithm at reduced radiation dose (21.4% dose reduction) shows comparable image quality to the image reconstructed with FBP, with lower image noise.²⁹

comparing coronal images of a patient with a right renal cyst. The lesion was well visualized on both images with comparable image quality, however the image reconstructed using ASiR was significantly less noisy and required a lower radiation dose to obtain.

Certain studies did however show that using an excessive blend of ASiR in the algorithm can result in a deterioration in the quality of images.^{14,30,31} One study conducted on a CT phantom reported that a blend of 50% ASiR or higher can result in a smoothed image texture that radiologists are uncomfortable with.³⁰ A smoothed appearance can result in a deterioration of subjective image quality, as shown in 2 studies performed in abdominal and soft tissue neck CT scans, where significant decreases in the visibility of small structures due to the smoothing effect were noted in ASiR images even at a blend of 40% ASiR.^{14,31}

Finally, one study evaluated the performance of ASIR-V, which is the latest generation of the ASiR algorithm.²⁰ Image noise, CNR and spatial resolution were compared between FBP and 3 levels (30%, 50% and 70%) of ASiR and ASIR-V algorithms, at 5 different tube currents with the use of a body phantom. The 50% ASIR-V algorithm was found to produce the best spatial resolution in images, and the ASIR-V algorithms in general demonstrated significantly superior decreases in noise levels and increases in CNR. The use of a 50% ASIR-V algorithm yielded a maximum noise reduction of 61.3%, in addition to an increase in CNR of 248.4% when performed at the lowest tube current of 30 mA.

Performance of Veo (MBIR)

Results from various studies showed that Veo may potentially offer better dose reduction and image quality improvement than older-generation IR algorithms such as ASiR when compared to FBP. One phantom study compared the impact of MBIR to FBP and 50% ASiR algorithms on dose reduction in abdominal CT imaging at various levels of tube current.³² The results revealed

that while the ASiR algorithm was able to provide up to a 35.9% reduction in dose, the use of MBIR allowed for a greater dose reduction of 59.9% when both algorithms were compared to FBP. Using the exact three algorithms, a separate study by Katsura et al³³ evaluated the effect of MBIR on the image quality in the CT imaging of the cervicothoracic region, and found that MBIR images had notably lower objective image noise when compared to ASiR and FBP images (8.88 *versus* 18.63 *versus* 26.52 Hounsfield units respectively). The outcomes of both studies are similar to another phantom study, which reported significant lower noise in MBIR images when compared to FBP images at all radiation dose levels in CT scans of the liver.³⁴ Significant improvements were also noted in both spatial resolution and low-contrast detectability when MBIR was used over FBP.

Despite its advantages, the use of MBIR can result in a pixelated blotchy appearance in images, as noted in the study by Katsura et al.³³ Similar findings were reported in another study performed in pediatric chest CT examinations, where a blotchy pixelated appearance of the central bronchi and lung vessels was seen in minimum-dose MBIR images.³⁵ The smoothing effect resulting from the use of MBIR was also found to result in sub-optimal resolution of bone structures in a separate study on low-dose CT examinations of the paranasal sinuses.³⁶

Studies in specific populations such as pediatrics also reported significant improvements in overall image quality with the use of the MBIR algorithm, specifically with reduced image noise and improved SNR. Two studies in pediatric chest CT examinations in particular noted an improved visualization of small structures, such as subpleural vessels and lung fissures, in reduced-dose CT examinations with the use of the MBIR algorithm.^{35,37}

Performance of the IRIS Algorithm

Studies evaluating the performance of IRIS in CT examinations generally reported that the use of IRIS preserved or improved image quality when compared to the FBP algorithm in reduced-

dose scans. Significantly reduced noise (23.3 versus 33.5 Hounsfield Units, p -value=0.001) and improved subjective image quality scores (3.2 versus 3.0, p -value=0.038) were noted when IRIS was used over FBP in coronary CT angiography examinations.³⁸ Another study meanwhile found no notable differences in both objective image noise and subjective image quality between reduced-dose IRIS images and standard-dose FBP images in CT examinations of the chest, abdomen and pelvis, despite a dose reduction of 44.4% (6.7 mSv versus 12.0 mSv).³⁹ On the other hand, no significant differences in subjective image quality (4.37 versus 4.31, p -value=0.72) were noted between IRIS and FBP images in reduced-dose CT examinations of the paranasal sinuses when radiation dose was reduced by up to 60% (0.11 mSv versus 0.28 mSv), while significant improvement in mean image quality score (4.81 versus 4.37, p -value=0.004) was achieved when radiation dose was reduced by only 20% (0.23 mSv versus 0.28 mSv).⁴⁰

Three other studies however suggested much lower thresholds for dose reduction in order for the use of IRIS to preserve image quality. One study comparing with the use of FBP and IRIS algorithms in chest CT examinations at both 100% and 50% doses found that while objective image noise was considerably lower in half-dose IRIS images than in full-dose FBP images, the subjective image quality score was significantly lower (p -value<0.0001) for half-dose IRIS images than for full-dose FBP images.²¹ The decrease in image quality scores was largely due to poorer image contrast and sharpness of mediastinal structures. Similarly, in a study of patients undergoing liver CT scans for hepatocellular carcinoma (HCC), overall subjective image quality was lower (2.27 versus 2.87, p -value<0.05) in IRIS images at 80 kV than FBP images at 120 kV.⁴¹ Head CT images reconstructed using IRIS at 30% reduced dose were also found to have considerable poorer subjective image quality when compared to standard-dose FBP images in a study by Korn et al,²³ and a linear regression analysis of CNR against tube current performed in the study suggested that the use of IRIS only preserves image quality up to an approximate 20.4% reduction in radiation dose.

Performance of SAFIRE and ADMIRE Algorithms

Studies that evaluated the performance of the SAFIRE algorithm in general also reported superior or similar image quality in reduced-dose SAFIRE images, in comparison to standard-dose FBP images. Improvements in subjective assessment of noise and image quality scores were noted in SAFIRE images at 20% reduced dose level (1.3 versus 1.6 and 1.3 versus 1.7 respectively), in a study assessing the performance of SAFIRE in head CT examinations.⁴² The results are supplemented by findings in a study that compared half-dose SAFIRE images to full-dose FBP images in chest CT examinations, reporting lower objective noise and improved SNR (p -value<0.001) in SAFIRE lung images, while no considerable differences were noted in subjective image quality on both lung and mediastinal images.⁴³ Additionally, 1 phantom study indicated improved low-contrast detect-

ability with the use of SAFIRE for all radiation dose levels and lesion sizes, with no statistically significant changes in spatial resolution.⁴⁴

Certain studies showed that other factors, such as patient body weight and anatomy of interest, can affect the performance of SAFIRE in improving image quality. While SNR and CNR improved in SAFIRE images of patients weighing 75 kg and below, no improvements were noted in patients that were heavier than 75 kg, in a study which evaluated the performance of SAFIRE in coronary CT angiography.⁴⁵ The results are in line with a separate study by Wang et al⁴⁶ on obese patients with a body mass index (BMI) larger than 30 kg/m². Another study investigating the use of SAFIRE in cervical spine CT examinations meanwhile noted that while increasing the iteration strength level of the SAFIRE algorithm improved visualization of the intervertebral discs and ligaments, the use of a higher-strength SAFIRE algorithm resulted in poorer visualization of soft tissues and trabecular bone.⁴⁷

One study assessed the effect of ADMIRE on low-contrast detectability in a contrast-detail phantom, when compared to the FBP algorithm.⁴⁸ The results demonstrated an average increase of 5.2% (p -value<0.001) in detection accuracy with the use of ADMIRE, and low contrast detectability increased with increasing object contrast, size, dose index and strength of ADMIRE. The use of the ADMIRE algorithm allowed a significant reduction in dose that ranged from 56% to 60% and 4% to 80% in 2 reading sessions, while preserving low-contrast detectability.

Performance of the iDose⁴ Algorithm

Comparison of the performance of the iDose⁴ algorithm to the FBP algorithm generally demonstrated lower image noise, increased CNR and improved overall image quality with the use of iDose⁴, when reconstructed images were acquired at the same level of radiation dose. One such study assessed the performance of the iDose⁴ algorithm in CT perfusion scans of the pancreas, and reported a noise reduction of 36.8% (10.6 versus 16.9 Hounsfield Units) when comparing iDose⁴ images to FBP images at 80 kV.⁴⁹ Similarly, subjective image quality scores were markedly higher in iDose⁴ images, when compared to FBP images in another study involving low-dose CT scans of the brain (2.91 versus 2.72, p -value<0.0055).⁵⁰ In addition, no changes in spatial resolution were noted with the use of the iDose⁴ algorithm in another study which investigated the performance of FBP and iDose⁴ algorithms at different acquisition parameter settings with the use of a Catphan phantom.⁵¹ The study also reported improvement in low-contrast resolution with the use of iDose⁴ in low-dose scans of less than 5 mGy.

Differences do however exist between these studies when comparing the image quality of iDose⁴ images at reduced dose to FBP images acquired at standard dose. While the study on CT perfusion scans of the pancreas reported no notable dif-

ferences in subjective image quality and mean CNR values between reduced-dose (10.81 mSv) iDose⁴ images and standard-dose (23.37 mSv) FBP images, improvements in both objective and subjective image quality in iDose⁴ images were noted in another study performed in chest-abdomen-pelvis CT scans, with an effective dose reduction of 46.5% (7.1 mSv *versus* 12.9 mSv).^{49,52} Interestingly, reduced-dose iDose⁴ images were given poorer subjective image quality scores by radiologists when compared to standard-dose FBP images in the study involving low-dose CT scans of the brain, despite lower objective noise levels in the iDose⁴ images.⁵⁰

Performance of AIDR and AIDR 3D Algorithms

One study assessed the influence of AIDR on dose reduction and image quality, while four others compared the newer AIDR 3D algorithm with the FBP algorithm. In a study which assessed the impact of the AIDR algorithm in both a phantom study and a patient-based study in lumbar spine CT examinations, it was reported that lower image noise and improved SNR was achieved with the use of AIDR without altering spatial resolution.⁵³ Results of the patient-based study showed a mean image noise reduction of 31% (15.6 *versus* 22.5 Hounsfield units) and an improvement of SNR from 2.36 to 3.50 with AIDR, despite an estimated dose reduction of 52%.

Studies assessing the performance of AIDR 3D algorithms generally reported significant image noise reduction and CNR improvement when AIDR 3D was used over the FBP algorithm. In a study by Kim et al⁵⁴ which assessed the effectiveness of AIDR 3D on noise reduction according to body habitus by using phantoms of different sizes, the use of AIDR 3D significantly reduced image noise and improved CNR and SNR values (p -values=0.001), with increasing noise reduction as the size of the phantom increased. Similar findings are reported in another study by Schindera et al,⁵⁵ where objective noise was reduced by 14.5 to 37.5% in abdominal CT examinations of obese patients through the use of a liver phantom.

However, the results vary when discussing its effect on low-contrast detectability. The study by Schindera et al⁵⁶ noted no significant improvement in low-contrast detectability, when AIDR 3D was used for scans on obese patients. Yet, a separate liver phantom study conducted by the same authors evaluating the use of AIDR 3D in general abdominal scans, reported that the use of AIDR 3D failed to preserve low-contrast detectability when the radiation dose level was reduced by 80%. In the latter study, sensitivity for detection of low-contrast liver tumors was found to be significantly lower (p -value=0.019) in AIDR 3D images acquired at 20% dose, when compared to both FBP and AIDR 3D images acquired at the full radiation dose level.

DISCUSSION

Increasing demand for CT examinations has led to rising concerns over the amount of exposure to ionizing radiation in medi-

cal imaging.⁴ Together with the rapid advancements in computer technology, IR algorithms have recently re-emerged as an alternative to the FBP algorithm in CT image reconstruction for dose reduction while preserving image quality.¹ This systematic review evaluated the relevant literature from 2012 to 2015 to establish if there is a general consensus that IR algorithms faithfully reduce dose and improve image quality in CT when compared to the FBP algorithm.

Review of the literature in clinical performance studies of different IR algorithms showed that the use of IR algorithms definitively reduced objective image noise regardless of the type of IR algorithm used.^{28,29,31,33-35,37,38,43,49,54,55} The extent of the noise reduction achieved however varies and depends on various factors, such as the type of IR algorithm used, the acquisition parameter settings, patient size and the type of CT examination performed. Newer generations of IR algorithms, such as MBIR and ASIR-V, allow for significantly increased noise reduction when compared to older algorithms such as ASiR, as demonstrated in the studies by Lim et al²⁰ and Ning et al.³²

It is however insufficient to draw conclusions on the performance of IR algorithms based on objective image noise alone. The subjective image quality with the use of IR algorithms also needs to be considered, so as to evaluate their effects on spatial resolution, low-contrast detectability and diagnostic acceptability.⁹ Most studies reported no changes in spatial resolution with the use of IR algorithms, while low-contrast detectability were preserved or improved despite IR images being acquired at a lower dose level.^{29,34,44,51,57}

Results from the literature suggest that the preservation of subjective image quality with the use of IR algorithms only holds true up to a certain threshold in dose reduction. When the radiation dose level is reduced excessively, the use of IR algorithms is unable to preserve image quality, as seen in studies by Hwang et al²¹ and Hur et al,⁴¹ where subjective image scores of IRIS images acquired at 50% and 70% dose respectively were considerably poorer than standard-dose FBP images. Similar findings were reported in two other studies by Love et al⁵⁰ and Schindera et al,⁵⁶ which assessed the performance of the iDose⁴ and AIDR 3D algorithms respectively. It is difficult to quantify the optimal amount of dose reduction that IR algorithms are able to provide without compromising on image quality, since it is dependent on various factors such as the type of IR algorithm used and the anatomy of interest that is examined, although one study by Korn et al²³ suggested that the use of an IRIS algorithm preserves image quality up to a 20.4% reduction in dose level.

The use of IR algorithms in CT examinations of specific patient populations, such as pediatrics and obese patients, have also shown to preserve or improve overall image quality in low-dose scans.^{28,29,35,37,46,54} In particular, the amount of noise reduction was noted to increase as the size of the body habitus increased in the studies of obese patients.⁵⁴ This is a noteworthy finding with important implications, since radiation dose is par-

ticularly of huge concern in these patient groups. Pediatrics are generally more sensitive to ionizing radiation than adults, while patients of larger body habitus receive higher radiation doses due to higher exposure settings required to obtain diagnostically acceptable images.

In the use of hybrid IR algorithms such as ASiR and iDose⁴, the percentage blend of IR algorithm to FBP can impact the influence of IR algorithms on the image quality of produced images. Using an excessively high iteration level of these algorithms can produce a smoothing effect on images that may reduce visibility of small structures and consequently deteriorate subjective image quality.^{14,31,33} Artifacts were also noted with the use of the MBIR algorithm, where a blotchy pixelated appearance of the central bronchi and lung vessels was noted in a study performed in chest CT examinations.³³ It should however be noted that the changes in image appearance did not affect the diagnostic acceptability of images.

Finally, whether the use of IR algorithms improves image quality also depends on the anatomy of interest that is examined. Visualization of soft tissues and trabecular bone was noted to be poorer with increased strengths of SAFIRE algorithm in cervical spine CT examinations, while bone structure visualization was also poorer with the use of the MBIR algorithm in CT examinations of the paranasal sinuses.^{36,47} A possible conclusion that may be drawn from these findings is that the use of IR algorithms are unable to correct for poor image detail in denser structures as bone, although further studies are needed to validate this observation.

A limitation of the current review is that there were very few studies performed on the newest generations of IR algorithms, such as ASiR-V and ADMIRE. This is likely due to the fact that the algorithms were only introduced in late 2013 and 2014 respectively, resulting in limited availability of these algorithms for clinical use. Although results from the only studies evaluating these algorithms appear promising, further research is needed in clinical trials to affirm these results.

With the continuous research in place to develop newer generations of IR algorithms and rapid improvement in computer technology, it is likely that more advanced IR algorithms will be developed in the near future. The use of these algorithms will likely be able to further reduce radiation dose in CT examinations while preserving image quality, therefore a probable gradual shift away from traditional analytical methods for image reconstruction should be expected in the foreseeable future.

CONCLUSION

In conclusion, the results of the literature from 2012 to 2015 share the general consensus that IR algorithms do faithfully reduce radiation dose and improve image quality in CT examinations, when compared with the FBP algorithm. The use of IR algorithms definitively reduces objective image noise even at

reduced radiation dose levels, while subjective image quality, in terms of spatial resolution and low contrast detectability, is improved or preserved with the use of IR algorithms as long as the radiation dose is not reduced excessively. However, the use of IR algorithms of excessively high iteration levels should be avoided, as the produced smoothing effect can negatively impact the subjective image quality. The use of IR algorithms may also be unable to preserve image detail in denser structures such as bone, although further research may be needed to validate this observation. With the rapid improvement in technology, IR algorithms will likely become the preferred CT image reconstruction method in the foreseeable future.

ACKNOWLEDGMENTS

The authors thank the Department of Medical Imaging and Radiation Sciences, Monash University, Clayton, Victoria, Australia, for providing the opportunity to make this collaboration possible.

CONFLICTS OF INTEREST

The authors do not have any conflicts of interest to disclose.

REFERENCES

1. Beister M, Kolditz D, Kalender WA. Iterative reconstruction methods in X-ray CT. *Phys Med*. 2012; 28(2): 94-108. doi: [10.1016/j.ejpm.2012.01.003](https://doi.org/10.1016/j.ejpm.2012.01.003)
2. Smith SW. *The Scientist and Engineer's Guide to Digital Signal Processing*. California, USA: California Technical Publishing; 1997: 447.
3. Berdahl CT, Vermeulen MJ, Larson DB, Schull MJ. Emergency department computed tomography utilization in the United States and Canada. *Ann Emerg Med*. 2013; 62(5): 486-494.e3. doi: [10.1016/j.annemergmed.2013.02.018](https://doi.org/10.1016/j.annemergmed.2013.02.018)
4. Brenner DJ, Hall EJ. Cancer risks from CT scans: Now we have data, what next? *Radiology*. 2012; 265(2): 330-331. doi: [10.1148/radiol.12121248](https://doi.org/10.1148/radiol.12121248)
5. Ma S, Kong B, Liu B, Liu X. Biological effects of low-dose radiation from computed tomography scanning. *Int J Radiat Biol*. 2013; 89(5): 326-333. doi: [10.3109/09553002.2013.756595](https://doi.org/10.3109/09553002.2013.756595)
6. Kaza RK, Platt JF, Goodsitt MM, et al. Emerging techniques for dose optimization in abdominal CT. *Radiographics*. 2014; 34(1): 4-17. doi: [10.1148/rg.341135038](https://doi.org/10.1148/rg.341135038)
7. Lee KH, Lee JM, Moon SK, et al. Attenuation-based automatic tube voltage selection and tube current modulation for dose reduction at contrast-enhanced liver CT. *Radiology*. 2012; 265(2): 437-447. doi: [10.1148/radiol.12112434](https://doi.org/10.1148/radiol.12112434)

8. Hsieh J, Nett B, Yu Z, Sauer K, Thibault J-B, Bouman CA. Recent advances in CT image reconstruction. *Current Radiology Reports*. 2013;1(1): 39-51. doi: [10.1007/s40134-012-0003-7](https://doi.org/10.1007/s40134-012-0003-7)
9. Geyer LL, Schoepf UJ, Meinel FG, et al. State of the art: Iterative CT reconstruction techniques. *Radiology*. 2015; 276(2): 339-357. doi: [10.1148/radiol.2015132766](https://doi.org/10.1148/radiol.2015132766)
10. Goldman AR, Maldjian PD. Reducing radiation dose in body CT: A practical approach to optimizing CT protocols. *AJR Am J Roentgenol*. 2013; 200(4): 748-754. doi: [10.2214/AJR.12.10330](https://doi.org/10.2214/AJR.12.10330)
11. Padole A, Ali Khawaja RD, Kalra MK, Singh S. CT radiation dose and iterative reconstruction techniques. *AJR Am J Roentgenol*. 2015; 204(4): W384-W392. doi: [10.2214/AJR.14.13241](https://doi.org/10.2214/AJR.14.13241)
12. Seibert JA. Iterative reconstruction: How it works, how to apply it. *Pediat Radiol*. 2014; 44(Suppl 3): 431-439. doi: [10.1007/s00247-014-3102-1](https://doi.org/10.1007/s00247-014-3102-1)
13. Ehman EC, Yu L, Manduca A, et al. Methods for clinical evaluation of noise reduction techniques in abdominopelvic CT. *Radiographics*. 2014; 34(4): 849-862. doi: [10.1148/rg.344135128](https://doi.org/10.1148/rg.344135128)
14. Vachha B, Brodoefel H, Wilcox C, Hackney DB, Moonis G. Radiation dose reduction in soft tissue neck CT using adaptive statistical iterative reconstruction (ASIR). *Eur J Radiol*. 2013; 82(12): 2222-2226. doi: [10.1016/j.ejrad.2013.08.014](https://doi.org/10.1016/j.ejrad.2013.08.014)
15. Ren Q, Dewan SK, Li M, et al. Comparison of adaptive statistical iterative and filtered back projection reconstruction techniques in brain CT. *Eur J Radiol*. 2012; 81(10): 2597-2601. doi: [10.1016/j.ejrad.2011.12.041](https://doi.org/10.1016/j.ejrad.2011.12.041)
16. Marin D, Choudhury KR, Gupta RT, et al. Clinical impact of an adaptive statistical iterative reconstruction algorithm for detection of hypervascular liver tumours using a low tube voltage, high tube current MDCT technique. *Eur Radiol*. 2013; 23(12): 3325-3335. doi: [10.1007/s00330-013-2964-1](https://doi.org/10.1007/s00330-013-2964-1)
17. Husarik DB, Alkadhi H, Puippe GD, et al. Model-based iterative reconstruction for improvement of low-contrast detectability in liver CT at reduced radiation dose: Ex-vivo experience. *Clinical Radiology*. 2015; 70(4): 366-372. doi: [10.1016/j.crad.2014.11.015](https://doi.org/10.1016/j.crad.2014.11.015)
18. Yamada Y, Jinzaki M, Tanami Y, et al. Model-based iterative reconstruction technique for ultralow-dose computed tomography of the lung: A pilot study. *Invest Radiol*. 2012; 47(8): 482-489. doi: [10.1097/RLI.0b013e3182562a89](https://doi.org/10.1097/RLI.0b013e3182562a89)
19. Li K, Tang J, Chen GH. Statistical model based iterative reconstruction (MBIR) in clinical CT systems: Experimental assessment of noise performance. *Med Phys*. 2014; 41(4): 041906. doi: [10.1118/1.4867863](https://doi.org/10.1118/1.4867863)
20. Lim K, Kwon H, Cho J, et al. Initial phantom study comparing image quality in computed tomography using adaptive statistical iterative reconstruction and new adaptive statistical iterative reconstruction v. *J Comput Assist Tomogr*. 2015; 39(3): 443-448. doi: [10.1097/rct.0000000000000216](https://doi.org/10.1097/rct.0000000000000216)
21. Hwang HJ, Seo JB, Lee JS, et al. Radiation dose reduction of chest CT with iterative reconstruction in image space-Part I: Studies on image quality using dual source CT. *Korean J Radiol*. 2012; 13(6): 711-719. doi: [10.3348/kjr.2012.13.6.711](https://doi.org/10.3348/kjr.2012.13.6.711)
22. Park EA, Lee W, Kim KW, et al. Iterative reconstruction of dual-source coronary CT angiography: Assessment of image quality and radiation dose. *Int J Cardiovasc Imaging*. 2012; 28(7): 1775-1786. doi: [10.1007/s10554-011-0004-2](https://doi.org/10.1007/s10554-011-0004-2)
23. Korn A, Fenchel M, Bender B, et al. Iterative reconstruction in head CT: Image quality of routine and low-dose protocols in comparison with standard filtered back-projection. *AJNR Am J Neuroradiol*. 2012; 33(2): 218-224. doi: [10.3174/ajnr.A2749](https://doi.org/10.3174/ajnr.A2749)
24. Lee M, Kim MJ, Han KH, Lee MJ. Half-dose abdominal CT with sinogram-affirmed iterative reconstruction technique in children-comparison with full-dose CT with filtered back projection. *Pediat Radiol*. 2015; 45(2): 188-193. doi: [10.1007/s00247-014-3105-y](https://doi.org/10.1007/s00247-014-3105-y)
25. Haubenreisser H, Fink C, Nance JW Jr., et al. Feasibility of slice width reduction for spiral cranial computed tomography using iterative image reconstruction. *Eur J Radiol*. 2014; 83(6): 964-969. doi: [10.1016/j.ejrad.2014.01.026](https://doi.org/10.1016/j.ejrad.2014.01.026)
26. Romagnoli A, Funel V, Meschini A, et al. Optimisation of low-dose CT with adaptive statistical iterative reconstruction in total body examination. *Radiol Med*. 2012; 117(8): 1333-1346. doi: [10.1007/s11547-012-0897-3](https://doi.org/10.1007/s11547-012-0897-3)
27. Kaul D, Grupp U, Kahn J, et al. Reducing radiation dose in the diagnosis of pulmonary embolism using adaptive statistical iterative reconstruction and lower tube potential in computed tomography. *Eur Radiol*. 2014; 24(11): 2685-2691. doi: [10.1007/s00330-014-3290-y](https://doi.org/10.1007/s00330-014-3290-y)
28. Singh S, Kalra MK, Shenoy-Bhangle AS, et al. Radiation dose reduction with hybrid iterative reconstruction for pediatric CT. *Radiology*. 2012; 263(2): 537-546. doi: [1148/radiol.12110268](https://doi.org/10.1148/radiol.12110268)
29. Desai GS, Uppot RN, Yu EW, Kambadakone AR, Sahani DV. Impact of iterative reconstruction on image quality and radiation dose in multidetector CT of large body size adults. *Eur Radiol*. 2012; 22(8): 1631-1640. doi: [10.1007/s00330-012-2424-3](https://doi.org/10.1007/s00330-012-2424-3)
30. Brady SL, Yee BS, Kaufman RA. Characterization of adap-

- tive statistical iterative reconstruction algorithm for dose reduction in CT: A pediatric oncology perspective. *Med Phys*. 2012; 39(9): 5520-5531. doi: [10.1118/1.4745563](https://doi.org/10.1118/1.4745563)
31. Boning G, Schafer M, Grupp U, et al. Comparison of applied dose and image quality in staging CT of neuroendocrine tumor patients using standard filtered back projection and adaptive statistical iterative reconstruction. *Eur J Radiol*. 2015; 84(8): 1601-1607. doi: [10.1016/j.ejrad.2015.04.017](https://doi.org/10.1016/j.ejrad.2015.04.017)
32. Ning P, Zhu S, Shi D, Guo Y, Sun M. X-ray dose reduction in abdominal computed tomography using advanced iterative reconstruction algorithms. *PLoS ONE*. 2014; 9(3): e92568. doi: [10.1371/journal.pone.0092568](https://doi.org/10.1371/journal.pone.0092568)
33. Katsura M, Sato J, Akahane M, et al. Comparison of pure and hybrid iterative reconstruction techniques with conventional filtered back projection: Image quality assessment in the cervicothoracic region. *Eur J Radiol*. 2013; 82(2): 356-360. doi: [10.1016/j.ejrad.2012.11.004](https://doi.org/10.1016/j.ejrad.2012.11.004)
34. Husarik DB, Marin D, Samei E, et al. Radiation dose reduction in abdominal computed tomography during the late hepatic arterial phase using a model-based iterative reconstruction algorithm: How low can we go? *Invest Radiol*. 2012; 47(8): 468-474. doi: [10.1097/RLI.0b013e318251eafd](https://doi.org/10.1097/RLI.0b013e318251eafd)
35. Mievilte FA, Berteloot L, Grandjean A, et al. Model-based iterative reconstruction in pediatric chest CT: Assessment of image quality in a prospective study of children with cystic fibrosis. *Pediatr Radiol*. 2013; 43(5): 558-567. doi: [10.1007/s00247-012-2554-4](https://doi.org/10.1007/s00247-012-2554-4)
36. Hoxworth JM, Lal D, Fletcher GP, et al. Radiation dose reduction in paranasal sinus CT using model-based iterative reconstruction. *AJNR Am J Neuroradiol*. 2014; 35(4): 644-649. doi: [10.3174/ajnr.A3749](https://doi.org/10.3174/ajnr.A3749)
37. Sun J, Zhang Q, Hu D, Duan X, Peng Y. Improving pulmonary vessel image quality with a full model-based iterative reconstruction algorithm in 80kVp low-dose chest CT for pediatric patients aged 0-6 years. *Acta Radiol*. 2015; 56(6): 761-768. doi: [10.1177/0284185114540884](https://doi.org/10.1177/0284185114540884)
38. Spears JR, Schoepf UJ, Henzler T, et al. Comparison of the effect of iterative reconstruction versus filtered back projection on cardiac CT postprocessing. *Acad Radiol*. 2014; 21(3): 318-324. doi: [10.1016/j.acra.2013.11.008](https://doi.org/10.1016/j.acra.2013.11.008)
39. Karpitschka M, Augart D, Becker HC, Reiser M, Graser A. Dose reduction in oncological staging multidetector CT: Effect of iterative reconstruction. *Br J Radiol*. 2013; 86(1021): 20120224. doi: [10.1259/bjr.20120224](https://doi.org/10.1259/bjr.20120224)
40. Bulla S, Blanke P, Hassepass F, et al. Reducing the radiation dose for low-dose CT of the paranasal sinuses using iterative reconstruction: Feasibility and image quality. *Eur J Radiol*. 2012; 81(9): 2246-2250. doi: [10.1016/j.ejrad.2011.05.002](https://doi.org/10.1016/j.ejrad.2011.05.002)
41. Hur S, Lee JM, Kim SJ, Park JH, Han JK, Choi BI. 80-kVp CT using Iterative Reconstruction in Image Space algorithm for the detection of hypervascular hepatocellular carcinoma: Phantom and initial clinical experience. *Korean J Radiol*. 2012; 13(2): 152-164. doi: [10.3348/kjr.2012.13.2.152](https://doi.org/10.3348/kjr.2012.13.2.152)
42. Korn A, Bender B, Fenchel M, et al. Sinogram affirmed iterative reconstruction in head CT: Improvement of objective and subjective image quality with concomitant radiation dose reduction. *Eur J Radiol*. 2013; 82(9): 1431-1435. doi: [10.1016/j.ejrad.2013.03.011](https://doi.org/10.1016/j.ejrad.2013.03.011)
43. Wang H, Tan B, Zhao B, Liang C, Xu Z. Raw-data-based iterative reconstruction versus filtered back projection: Image quality of low-dose chest computed tomography examinations in 87 patients. *Clin Imaging*. 2013; 37(6): 1024-1032. doi: [10.1016/j.clinimag.2013.06.004](https://doi.org/10.1016/j.clinimag.2013.06.004)
44. von Falck C, Bratanova V, Rodt T, et al. Influence of sinogram affirmed iterative reconstruction of CT data on image noise characteristics and low-contrast detectability: An objective approach. *PLoS ONE*. 2013; 8(2): e56875. doi: [10.1371/journal.pone.0056875](https://doi.org/10.1371/journal.pone.0056875)
45. Schuhbaeck A, Achenbach S, Layritz C, et al. Image quality of ultra-low radiation exposure coronary CT angiography with an effective dose <0.1 mSv using high-pitch spiral acquisition and raw data-based iterative reconstruction. *Eur Radiol*. 2013; 23(3): 597-606. doi: [10.1007/s00330-012-2656-2](https://doi.org/10.1007/s00330-012-2656-2)
46. Wang R, Schoepf UJ, Wu R, et al. Image quality and radiation dose of low dose coronary CT angiography in obese patients: Sinogram affirmed iterative reconstruction versus filtered back projection. *Eur J Radiol*. 2012; 81(11): 3141-3145. doi: [10.1016/j.ejrad.2012.04.012](https://doi.org/10.1016/j.ejrad.2012.04.012)
47. Omoumi P, Verdun FR, Ben Salah Y, et al. Low-dose multidetector computed tomography of the cervical spine: Optimization of iterative reconstruction strength levels. *Acta Radiol*. 2014; 55(3): 335-344. doi: [10.1177/0284185113494981](https://doi.org/10.1177/0284185113494981)
48. Solomon J, Mileto A, Ramirez-Giraldo JC, Samei E. Diagnostic performance of an advanced modeled iterative reconstruction algorithm for low-contrast detectability with a third-generation dual-source multidetector CT scanner: Potential for radiation dose reduction in a multireader study. *Radiology*. 2015; 275(3): 735-745. doi: [10.1148/radiol.15142005](https://doi.org/10.1148/radiol.15142005)
49. Xie Q, Wu J, Tang Y, et al. Whole-organ CT perfusion of the pancreas: Impact of iterative reconstruction on image quality, perfusion parameters and radiation dose in 256-slice CT-preliminary findings. *PLoS ONE*. 2013; 8(11): e80468. doi: [10.1371/journal.pone.0080468](https://doi.org/10.1371/journal.pone.0080468)

50. Love A, Siemund R, Hoglund P, et al. Hybrid iterative reconstruction algorithm in brain CT: A radiation dose reduction and image quality assessment study. *Acta Radiologica*. 2014; 55(2): 208-217. doi: [10.1177/0284185113494980](https://doi.org/10.1177/0284185113494980)

51. Klink T, Obmann V, Heverhagen J, Stork A, Adam G, Begemann P. Reducing CT radiation dose with iterative reconstruction algorithms: The influence of scan and reconstruction parameters on image quality and CTDIvol. *Eur J Radiol*. 2014; 83(9):1645-1654. doi: [10.1016/j.ejrad.2014.05.033](https://doi.org/10.1016/j.ejrad.2014.05.033)

52. Arapakis I, Efstathopoulos E, Tsitsia V, et al. Using “iDose4” iterative reconstruction algorithm in adults’ chest-abdomen-pelvis CT examinations: Effect on image quality in relation to patient radiation exposure. *Br J Radiol*. 2014; 87(1036): 20130613. doi: [10.1259/bjr.20130613](https://doi.org/10.1259/bjr.20130613)

53. Gervaise A, Osemont B, Lecocq S, et al. CT image quality improvement using Adaptive Iterative Dose Reduction with wide-volume acquisition on 320-detector CT. *Eur Radiol*. 2012; 22(2): 295-301. doi: [10.1007/s00330-011-2271-7](https://doi.org/10.1007/s00330-011-2271-7)

54. Kim M, Lee JM, Yoon JH, et al. Adaptive iterative dose reduction algorithm in CT: Effect on image quality compared with filtered back projection in body phantoms of different sizes. *Korean J Radiol*. 2014; 15(2): 195-204. doi: [10.3348/kjr.2014.15.2.195](https://doi.org/10.3348/kjr.2014.15.2.195)

55. Schindera ST, Odedra D, Mercer D, et al. Hybrid iterative reconstruction technique for abdominal CT protocols in obese patients: Assessment of image quality, radiation dose, and low-contrast detectability in a phantom. *AJR Am J Roentgenol*. 2014; 202(2): W146-W152. doi: [10.2214/ajr.12.10513](https://doi.org/10.2214/ajr.12.10513)

56. Schindera ST, Odedra D, Raza SA, et al. Iterative reconstruction algorithm for CT: Can radiation dose be decreased while low-contrast detectability is preserved? *Radiology*. 2013; 269(2): 511-518. doi: [10.1148/radiol.13122349](https://doi.org/10.1148/radiol.13122349)

57. Gervaise A, Osemont B, Louis M, Lecocq S, Teixeira P, Blum A. Standard dose versus low-dose abdominal and pelvic CT: Comparison between filtered back projection versus adaptive iterative dose reduction 3D. *Diagn Interv Imaging*. 2014; 95(1): 47-53. doi: [10.1016/j.diii.2013.05.005](https://doi.org/10.1016/j.diii.2013.05.005)

Case Report

*Corresponding author

Yuko Kobashi, MD, PhD

Senior Investigator

Department of Radiology

Tokyo Dental College

Ichikawa General Hospital

5-11-13, Sugao, Ichikawa

Chiba 271-8513, Japan

Tel. +81-47-322-0151

Fax: +81-47-325-4456

E-mail: ykobashi@ijikei.ac.jp

Volume 1 : Issue 2

Article Ref. #: 1000ROJ1109

Article History

Received: August 5th, 2016

Accepted: September 15th, 2016

Published: September 15th, 2016

Citation

Kobashi Y, Munetomo Y, Baba A, Yamazoe S, Mogami T, Miyauchi J. Two case reports of angioleiomyoma of the finger. *Radiol Open J.* 2016; 1(2): 55-59. doi: [10.17140/ROJ-1-109](https://doi.org/10.17140/ROJ-1-109)

Copyright

©2016 Kobashi Y. This is an open access article distributed under the Creative Commons Attribution 4.0 International License (CC BY 4.0), which permits unrestricted use, distribution, and reproduction in any medium, provided the original work is properly cited.

Two Case Reports of Angioleiomyoma of the Finger

Yuko Kobashi, MD, PhD¹; Yohei Munetomo, MD¹; Akira Baba, MD¹; Shinji Yamazoe, MD¹; Takuji Mogami, MD¹; Jun Miyauchi MD²

¹Department of Radiology, Tokyo Dental College, Ichikawa General Hospital, 5-11-13, Sugao, Ichikawa, Chiba 271-8513, Japan

²Department of Pathology, Tokyo Dental College Ichikawa General Hospital, 5-11-13, Sugao, Ichikawa, Chiba 271-8513, Japan

ABSTRACT

Angioleiomyoma represents a benign stromal tumor, which usually occurs in the subcutaneous tissue of the extremities. The angioleiomyoma in the finger is rare. We report 2 rare cases of an angioleiomyoma in finger. Case one, was a 72-year-old man with a mass on the radial side of distal phalanx of the left third finger. Case two, was a 70-year-old man with a mass on the ulnar side of interphalangeal joint of the left thumb. Both cases showed isointense to hypointense mass lesion on both T1 and T2-weighted images and were pathologically diagnosed with an angioleiomyoma. Heterogeneously isointense to hypointense on T2-weighted MR image showed two components: smooth muscle tissue punctuated with thick-walled vessels and/or hyalization on pathological finding. When much hyalization is included, it will not be enhanced on gadolinium-enhanced fat suppressed T1-weighted magnetic resonance (MR) image. Both T2-weighted and gadolinium-enhanced fat suppressed T1-weighted MR image findings should be considered to predict tumor composition.

KEYWORDS: Angioleiomyoma; MRI; Hyalization; Myxoid.

INTRODUCTION

Angioleiomyoma in the extremities is a benign smooth muscle neoplasm arising from the small blood vessels of the muscle. It was first described in 1937 by AP Stout,¹ who reviewed the literature on solitary cutaneous and subcutaneous leiomyomas and added 15 more cases from his own clinic-pathologic findings.^{1,2} We found 40 articles about magnetic resonance imaging (MRI) findings in angioleiomyoma using PubMed online. Many authors reported that angioleiomyomas showed different types of signal intensity on MRI. There are very few reports about pathological and radiological correlation in angioleiomyomas. We report the pathological and radiological correlation of 2 cases of angioleiomyoma in the finger seen in our hospital and observed on MRI using a microscopy coil.

CASE REPORTS

Case 1

A 72-year-old man came to our observation because of the presence of a mass on his left middle finger, which had been hurting for the recent two weeks. The mass was present for approximately 30 years without pain or increase in size. On physical examination, the mass was slightly mobile, approximately 1 cm in size and located subcutaneously just adjacent to the radial side of distal phalanx of the left third finger. Overlying skin was intact. Range of motion of the proximal and distal interphalangeal joints of the third finger was complete. He had no history of trauma on the site of lesion. Radiograph of the finger showed an oval-shaped soft tissue mass lesion on the radial side of the distal phalanx. There was no associated calcification or

bony involvement (Figure 1). An excision biopsy was proposed. Before the surgery, a finger MRI was performed.

The finger MRI (1.5 Tesla Achiva, Philips, Netherlands) using a microscopy coil (micro 47 grant coil) showed a heterogeneously hypointense mass lesion located in the subcutaneous tissue layer adjacent to the distal phalanx of the left middle finger on both T1-weighted (TR 405 msec, TE 15 msec, Thickness 1.5 mm, FOV 60 mm) (Figure 2a) and T2-weighted (TR 2500 msec, TE 90 msec, Thickness 1.5 mm, FOV 60 mm) (Figure 2b) coronal images. On gadolinium-enhanced fat-suppressed T1-weighted coronal and axial images (TR 470 msec, TE 13 msec, Thickness 1.5 mm, FOV 60 mm), the mass lesion showed enhancement in the margin especially in the superior

area (Figures 2c-2d arrows). A fibro-proliferative neoplasm, an angioleiomyoma or a calcium pyrophosphate dihydrate crystal deposition disease (CPPD) like gout was initially suspected. Tumor resection was performed and the circumscribed mass was confirmed to be located within the subcutaneous fat.

No involvement of the adjacent lateral collateral ligament of the distal interphalangeal joint was observed. On microscopic examination, the mass showed well-circumscribed fascicles of mature smooth muscle cells surrounding vascular lumina, lined by normal appearing endothelium (Figure 3a), predominantly in the peripheral area of the tumor and mostly in the stromal hyalization (Figure 3b). The pathological diagnosis was an angioleiomyoma.



Figure 1: X-ray of the left 3rd finger, AP view. Oval shaped soft tissue density mass lesion without calcification is visualized along the distal phalanx of the third finger (arrow).

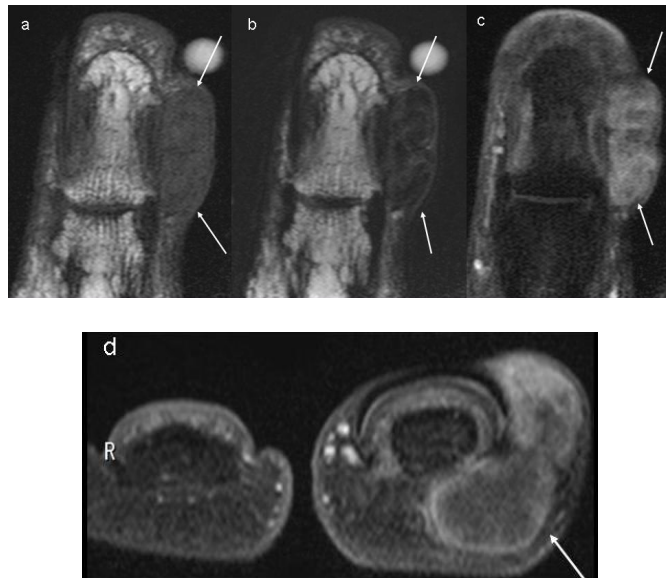


Figure 2: The third finger MRI using a microscopy coil (micro 47grant coil). The mass lesion shows very low signal intensity with intermediate signal septum on both T1-weighted (a) and T2-weighted (b) coronal images (arrows). On contrast study, the mass lesion is well enhanced (c, arrows).

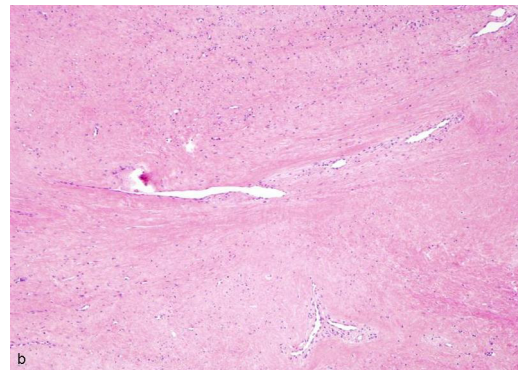
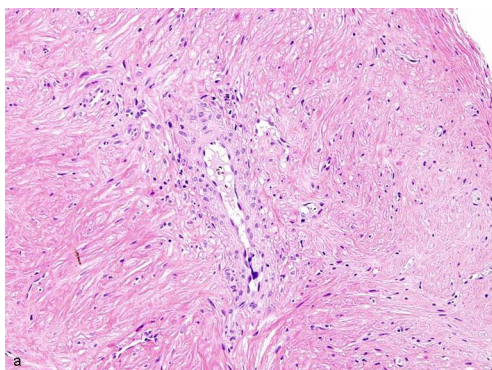


Figure 3: Tumor cells with H-E stain x200). The tumor consists of smooth muscle tissue punctuated with thick-walled vessels (a) and is predominantly visualized in the peripheral area. Most are occupied in the stromal hyalization (b).

Case 2

A 70-year-old man reported to our facility with a painless nodule adjacent to the ulnar side of interphalangeal joint (IP) of the left thumb. The nodule was present for approximately one year, with slow progressive growth. On physical examination, the nodule was rubbery in consistency, located subcutaneously and 1 cm in size. Overlying skin was intact. Range of motion of the left thumb was complete. Radiograph showed an oval-shaped soft tissue mass adjacent to the IP joint (Figure 4 arrow) of left thumb. An MRI (1.5 Tesla Achiva, Philips, Netherlands) was performed using a microscopy coil (micro 47 grant coil) in order to exclude the presence of a malignant tumor. It showed isointense nodule on both T2-weighted (TR 2550 msec, TE 90 msec, Thickness 1.5 mm, FOV 60 mm) (Figure 5a arrow) and T1-weighted (TR 400 msec, TE 15 msec, thickness 1.5 mm, FOV 60 mm) (Figure 5b arrow) image, and moderate enhancement on gadolinium-enhanced fat-suppressed T1-weighted im-

ages (TR 480 msec, TE 13 msec, Thickness 1.5 mm, FOV 60 mm) (Figure 5c arrow). The margins of the nodule were indistinct on MRI. We suspected an angioleiomyoma, a fibroproliferative neoplasm or a neurogenic tumor. Tumor resection was performed and a circumscribed mass was identified with in the subcutaneous fat layer. No involvement of the lateral collateral ligament of the IP joint was observed. Microscopically, it was composed of small vessels with smooth-muscle thickening of their walls (Figure 6). A little zonal distribution of hyalinization was noted. The pathological diagnosis was compatible with a solid type angioleiomyoma.

DISCUSSION

Angioleiomyoma in lower extremities occurs more frequently in women, while its presence at the head level, in the trunk or upper extremities is more common in men.^{3,4} The peak incidence is in the 4th to 6th decades of life. Pain and tenderness are more



Figure 4: X-ray of the left thumb, AP view. Oval shaped soft tissue density mass lesion is visualized at level of subcutaneous area of the IP joint (arrow). No bone erosive change is seen.

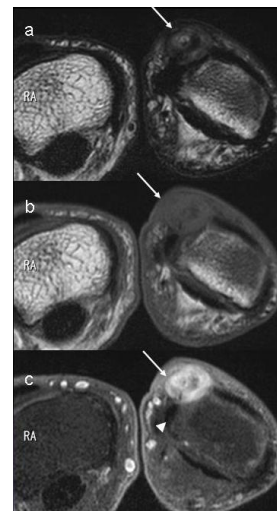


Figure 5: Thumb MRI using a microscopy coil (micro 47 grant coil). The mass lesion shows low signal intensity with a target like appearance on both T2-weighted (a, arrow) and T1-weighted (b, arrow). It is well-enhanced on gadolinium-enhanced fat suppression T1 weighted axial image (c, arrow). Medial lateral collateral ligament of the IP joint is indistinct (c, arrowhead).

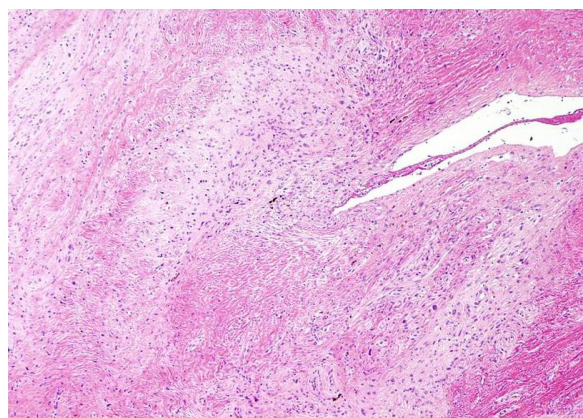


Figure 6: Tumor cells with H-E stain x100). Many small vessels with smooth-muscle thickening of their walls are visualized and are scattered among the stromal hyalinization.

frequent when the tumor is located in the lower extremities than in the upper extremities, head or neck. Duhig and Aye⁵ reported that 27 of 61 patients with this tumor complained of these symptoms.

Angioleiomyomas in the hand are rare and even more uncommon in the fingers. They account for 5-12% of all hand tumors. Prasad R et al⁶ reported that there are less than 200 cases of terminal phalanx angioleiomyoma described in the literature.

The most definitive diagnostic method to make a diagnosis is from histologic analysis of an excisional biopsy, together with a confirmatory immunohistochemical evaluation. Characteristics of angioleiomyoma on CT scan have not been well described yet. However, MRI has been frequently used as it is more sensitive for discerning between the soft tissue layers and can demonstrate a non-specific, well defined, round or oval mass in the subcutaneous or dermal tissue.⁷ Ashley DW et al⁸ reported that angioleiomyomas are usually either isointense or hyperintense if compared to skeletal muscle on T1-weighted MR image (low signal on magnetic resonance imaging) and heterogeneous on T2-weighted MR image (high signal on magnetic resonance imaging), and often have a hypointense fibrous capsule as the peripheral rim.

Some studies have reported about the pathological and radiological correlation of Angioleiomyoma.⁹⁻¹² Hwang et al¹⁰ suggested that the smooth muscle and the numerous vessels corresponded to the high signal intensity areas, while the fibrous tissue appeared iso signal intensity on T2-weighted MR images. Yoo et al¹¹ suggested that the presence of tortuous vascular channels surrounded by smooth muscle bundles and areas of myxoid change could explain the heterogeneity of signal intensity of the tumor on T2-weighted images. Matsuyama et al¹² reported that some flow void is suggestive of vessels along and/or within the tumor and can help in the diagnosis of angioleiomyoma. Some tumors showed predominant myxoid change and hyalization corresponding to the higher signal intensity on T2-weighted image than the remaining part of mass.⁹ However, in case 1, only hyalization component was visualized in the center area of the tumor on pathological findings and it showed heterogeneously hypointense signal on T2-weighted MR image. It may suggest that myxoid component reflects hyperintense signal and hyalization reflects hypointense signals on MRI. However, myxoid and hyalization occurring in angioleiomyomas might be secondary to the circulatory disturbance. In addition, small vessels with smooth-muscle thickening on pathological finding were consistent, with marginal enhancement area on gadolinium-enhanced fat suppression T1-weighted MR image. On the other hand, in our case 2, little hyalization areas were visualized in the tumor and showed isointense on T2-weighted MR image. Hyper cellular component composed of many small vessels with smooth-muscle thickening gave isointense on T2-weighted MR image. As the evidence, the tumor of case 2 moderately enhanced on gadolinium-enhanced fat suppressed T1-weighted MR image as compared to the tumor of case 1. Basing on the diagnostic

evidences obtained from our 2 cases, if we are able to consider both findings of T2-weighted and gadolinium-enhanced fat suppressed T1-weighted MR image, we could predict the tumor composition.

The differential diagnosis of a well-defined, enhancing, subcutaneous nodule or mass with T2-hyperintense to isointense signals includes synovial sarcoma, other low-grade soft tissue sarcomas, haemangioma, neurogenic tumour and nodular fasciitis. In addition, Low-grade sarcomas such as synovial sarcoma and low-grade myxofibrosarcoma may be slow in growing and appear well-circumscribed on MRI, giving the misleading impression that the lesion is well-localised. Haemorrhage, which may be seen as T2-hypointense, may be present in synovial sarcomas.

CONCLUSION

Angioleiomyoma of the finger is a rare tumor. Heterogeneously isointense to hypointense on T2-weighted MR image shows 2 components on pathological findings: a smooth muscle tissue punctuated with thick-walled vessels and/or hyalization. When much hyalization is included, it will not be enhanced on gadolinium-enhanced fat suppressed T1-weighted MR image. Both T2-weighted and gadolinium-enhanced fat suppressed T1-weighted MR images findings should consider in order to predict the tumor composition.

CONFLICTS OF INTEREST

The authors declare that they have no conflicts of interest.

CONSENT

The authors obtained written informed consent from the patients for submission of this manuscript for publication.

REFERENCES

1. Stout AP. Solitary cutaneous and subcutaneous leiomyoma. *Am J Cancer*. 1937; 29: 435-469. doi: [10.1158/ajc.1937.435](https://doi.org/10.1158/ajc.1937.435)
2. Marinou TR, Moustou E, Grivas TB, Zizi-Serbetzoglou A. Angioleiomyoma of the finger: A case report. *Scientific Chronicles*. 2014; 19(2): 190-195. Web site. <http://www.tzaneio.gr/epistimoniko/p14-2-12.pdf>. Accessed August 4, 2016
3. Hachisuga T, Hashimoto H, Enjoji M. Angioleiomyoma: A clinicopathologic reappraisal of 562 cases. *Cancer*. 1984; 54: 126-130. doi: [10.1002/1097-0142\(19840701\)54:1<126::AID-CNCR2820540125>3.0.CO;2-F](https://doi.org/10.1002/1097-0142(19840701)54:1<126::AID-CNCR2820540125>3.0.CO;2-F)
4. Morimoto N. Angiomyoma, Aclonicopathologic study. *Med J Kagoshima Univ*. 1973; 24: 663-683.
5. Duhig JT, Ayer JP. Vascular leiomyoma: A study of sixty-one

cases. *Arch Pathol Lab Med*. 1959; 68: 424-430.

6. Prasad R, Bhamidi A, Kumar RA, Muthukumar S. Angioleiomyoma of middle finger terminal phalanx-case report and review of literature. *J Hand Microsurg*. 2014; 6(1): 45-46. doi: [10.1007/s12593-013-0111-5](https://doi.org/10.1007/s12593-013-0111-5)

7. Sookur P, Saifuddin A. Indeterminate soft-tissue tumors of the hand and wrist: A review based on a clinical series of 39 cases. *Skeletal Radiology*. 2011; 40: 977-989. doi: [10.1007/s00256-010-1009-y](https://doi.org/10.1007/s00256-010-1009-y)

8. Willoughby AD, Schlüssel AT, Freeman JH, Lin-Hurtubise K. Angioleiomyoma in a rare location: A case report. *Hawaii J Med Public Health*. 2013; 72(2): 45-48. Web site. <https://www.ncbi.nlm.nih.gov/pmc/articles/PMC3585498/>. Accessed August 4, 2016

9. Jeong BS, Shim JC, Kim JY, et al. Radiologic findings of an angioleiomyoma of the finger: A case report. *J Korean Soc Radiol*. 2011; 64: 599-602. doi: [10.3348/jksr.2011.64.6.599](https://doi.org/10.3348/jksr.2011.64.6.599)

10. Hwang JW, Ahn JM, Kang HS, Suh JS, Kim SM, Seo JW. Vascular leiomyoma of an extremity: MR imaging-pathology correlation. *AJR Am J Roentgenol*. 1998; 171: 981-985. doi: [10.2214/ajr.171.4.9762979](https://doi.org/10.2214/ajr.171.4.9762979)

11. Yoo HJ, Choi JA, Chung JH, et al. Angioleiomyoma in soft tissue of extremities: MRI findings. *AJR Am J Roentgenol*. 2009; 192(6): 291-294. doi: [10.2214/AJR.07.3952](https://doi.org/10.2214/AJR.07.3952)

12. Matsuyama A, Oguro S, Kimura H, Ohtsuka T. *Bone and Soft Tissue Tumors*. 2nd ed. Tokyo, Japan: Shindan To Chiryousha Inc; 2015: 238-279.

Review

***Corresponding author
Martin Oliver Steinhauser, PhD**

Department of Systems Solutions
Fraunhofer-Institute for High-Speed
Dynamics, Ernst-Mach-Institut
EMI, Eckerstrasse 4, 79104
Freiburg, Germany;

Department of Chemistry
Faculty of Science
University of Basel
Klingelbergstrasse 80, CH-4056
Basel, Switzerland

Tel. +49 761-2714-424

Fax: +49 761-2714-1424

E-mail: martin.steinhauser@emi.fraunhofer.de

Volume 1 : Issue 2

Article Ref. #: 1000ROJ1110

Article History

Received: July 25th, 2016

Accepted: September 12th, 2016

Published: September 19th, 2016

Citation

Steinhauser MO. On the destruction of cancer cells using laser-induced shock waves: A review on experiments and multiscale computer simulations. *Radiol Open J*. 2016; 1(2): 60-75. doi: [10.17140/ROJ-1-110](https://doi.org/10.17140/ROJ-1-110)

Copyright

©2016 Steinhauser MO. This is an open access article distributed under the Creative Commons Attribution 4.0 International License (CC BY 4.0), which permits unrestricted use, distribution, and reproduction in any medium, provided the original work is properly cited.

On the Destruction of Cancer Cells Using Laser-Induced Shock Waves: A Review on Experiments and Multiscale Computer Simulations

Martin Oliver Steinhauser, PhD^{1,2*}

¹Department of Systems Solutions, Fraunhofer-Institute for High-Speed Dynamics, Ernst-Mach-Institut, EMI, Eckerstrasse 4, 79104 Freiburg, Germany

²Department of Chemistry, Faculty of Science, University of Basel, Klingelbergstrasse 80, CH-4056, Basel, Switzerland

ABSTRACT

In the clinical treatment of solid tumors, besides traditional surgery and chemotherapy, the use of High Intensity Focused Ultrasound (HIFU) has been established as a minimally non-invasive technique for tumor treatment, which is based on coagulative necrosis of cells, induced by conversion of mechanical energy into heat. Another, less developed technique for the destruction or damage of tumor cells, is based on the pure mechanical effects of strong shock waves on cells, which are generated by using laser ablation, thus avoiding the heat-related unwanted side-effect when using HIFU (cutaneous burns of healthy tissue). Despite the general therapeutic success of extracorporeal shock wave therapy in medicine, e.g. for disintegrating conglomerates, the mechanical effects of shock waves on the cytoskeleton of cells, on the transient permeability and rupture of cell membranes, or on tissue damage remain widely unknown. The mechanical behavior of bio-macromolecules however, is of particular importance on the cellular level as several basic and yet unanswered questions are raised: How are cell stresses and energy transmitted through cells and in what way are the forces and interactions that determine the stability of cell plasma membranes affected by a shock wave and give rise to cell deformation, structural damage or rupture of the membrane with subsequent apoptosis? Here, we intend to review research on the shock wave destruction of tumor cells and discuss the use of laser-ablation as a new potential technique for tumor treatment. We also discuss here recent progress in computational modeling strategies and techniques for understanding the basic physical mechanisms that occur in the interaction of shock waves with cellular structures and show how computer modeling and numerical simulation can contribute to a fundamental understanding in this emerging multidisciplinary field, where physics, chemistry, biology and medicine meet.

KEYWORDS: Shock waves; Molecular dynamics; Multiscale Modeling; Computer simulations; Cancer cells; Ultrasound; Drug delivery; Laser ablation.

ABBREVIATIONS: MRI: Magnetic Resonance Imaging; US: Ultrasound; MD: Molecular Dynamics; TMG: Tumor Suppressor Gene; MM: Multiscale Modeling; LISW: Laser-Induced Shock Waves; ESWL: Extracorporeal Shock Wave Lithotripsy; MRI: Magnetic Resonance Imaging; ECM: Extra Cellular Matrix; FE: Finite Element.

INTRODUCTION

On a fundamental level, cancer is a complex disease which exhibits uncontrolled cell proliferation: cancer cells, either through epigenetic alterations or mutations, overexpress oncogenes and under-express tumor suppressor genes (TMGs). Hence, the cells go through the cell cycle more often, completely disregarding apoptotic signals, resulting in an increased proliferation and uncontrolled tissue growth.¹ Consequently, most cancer therapies attempt to manipulate

these processes either by cytostatic (suppressing entry to or progression through the cell cycle) or cytotoxic (inducing apoptosis, programmed cell death) mechanisms. For example, chemotherapy agents such as doxorubicin are considered to be cytotoxic.² Therapies that target hormone-addicted cells (e.g., tamoxifen in estrogen-driven breast cancer) are considered to be cytostatic.³

The Physics of Cancer Cells

Studies of cells' passive viscoelasticity-based biomechanics have already led to deep insight into a cell since its mechanical properties are directly related to its function by the cytoskeleton composition and architecture.⁴ Intracellular pathologic changes influence cytoskeleton structure and function, which makes a cell's mechanical signature a highly sensitive marker of its health.⁵ In malignant cells the cytoskeleton devolves from an ordered and rigid structure to an irregular and compliant state, including a reduction of the cytoskeleton polymers and accessory proteins and a restructuring of the network. The cell changes from a mature state to a replicating, motile and cancerous form.⁶ From a more general viewpoint, cytoskeleton strength and organization increase as a cell becomes more differentiated. Thus, stem cells and malignant cells, as undifferentiated cells, are expected to be softer than mature and fully differentiated cells. Consequentially, measuring a cell's rigidity provides information about its state and composition and may be viewed as a cell marker.⁵ In recent years, genetic, immunocytochemical and biochemical studies have identified many different players involved in the regulation of the cytoskeleton. Physical studies concentrating on the mechanical properties of cells or *in vitro* cytoskeleton model systems have been helpful in elucidating the complex synergies and redundancies of generic physical and specific biological mechanisms in establishing the overall mechanical performance of biological tissue. Unexpectedly, such studies have revealed a remarkable universality in the viscoelastic response functions of reconstituted networks and of whole cells of different types over a wide range of timescales, which is reminiscent of glassy materials.^{7,8} At the same time, the overall cell stiffness has been demonstrated to be very sensitive to cytoskeleton dysfunction, a connection that lends itself to an extremely efficient and reliable automated detection (and may possibly also be the cause) of some diseases.⁵ To gain a detailed understanding of how these highly universal and specific mechanical properties of cells originate from the molecular structure of the cytoskeleton, it is essential to probe cell mechanics on multiple scales.

Treatments of Cancer

Traditionally, the only cure for solid tumors has been surgery, i.e. the resection of solid tumor tissue.⁹ However, open surgery is always associated with a high risk for the patient, suppression of a patient's immune system and a significant mortality rate. Minimally invasive techniques as an alternative to open surgery, which became available during the 1990's for localized tumor treatment, such as radiofrequency ablation,¹⁰ cryoablation,¹¹ direct laser ablation,¹² or high-intensity focused ultrasound

(HIFU), are methods which use a range of energies for direct *in situ* tumor destruction through energy absorption and killing by heating or evaporation. Besides direct conversion of mechanical energy into heat, biological material may be damaged by the effects of mechanical stress caused by shock waves.¹³ An efficient way to generate shock waves in biological systems became available to biomedical research by the use of high-power lasers shortly after the invention of the Q-switched pulsed laser in the 1960s.¹⁴

The Impact of Shock Waves on Cells

The theoretical foundations of shock wave physics originated from 17th century studies of classical acoustics and 18th century aeroballistics. With the advent of high-speed photography in late 19th century and further progress in experimental visualization techniques in 20th century, the study of shock waves in different states of matter has gradually emerged from a very small and unnoticed branch of physics to a major complex and interdisciplinary science.^{15,16}

Physical Definition of Shock Waves

Shock waves are in essence discontinuous, rapid mechanical phenomena that have been observed and studied in the laboratory and in nature, in microscopic as well as in macroscopic dimensions and in all states of matter: gaseous,^{17,18} liquid,¹⁹⁻²¹ solid,²²⁻²⁴ plasma,^{25,26} and even in Bose-Einstein condensates.²⁷⁻²⁹ Terrestrial examples³⁰ of naturally occurring discontinuities are high-energy events such as meteorite impacts, thunder, volcanic explosions, sea- and earthquakes or tsunamis, while in outer space³¹ they encompass plasma shock waves induced by solar wind, supernovae explosions, implosions of white dwarfs, comet and asteroid impacts, and stellar or galactic jets. This variety of phenomena and in particular the possible applications of shock waves in different areas such as physics, chemistry, biology, medicine and even engineering generally renders the scientific study of shock waves a rather fascinating and interdisciplinary subject.

We focus here on the physical proper definition of shock waves which—in medical literature—is not always used correctly and many studies fail to show that they were really dealing with shock waves and not merely with high-energy sound waves. In the natural sciences, a shock wave describes a mechanical wave characterized by a surface or sheet of discontinuity in which, within a narrow region, thermodynamic quantities such as pressure p , density ρ , particle velocity v or temperature T change abruptly.¹⁷ While a theory of shock waves with an infinitesimal jump condition can be developed *mathematically* in the framework of approximate continuum models of condensed matter, i.e. based on the hydrodynamic equations of ideal fluids or gases, in physical context, shock wave theory is somewhat limited, because the width of a shock wave is always of finite size and because of the actually discrete atomic nature of condensed matter. It turns out that shock waves are essentially small regions

of a system, where non-adiabatic, i.e. irreversible energy dissipation occurs. The notion of a shock wave as an infinitely thin sheet of discontinuity is a mathematical idealization. The width of the shock wave i.e. the size of the dissipative region establishes itself according to the conservation laws of continuum theory. In very strong, high-amplitude shock waves, their width becomes so small that they are practically indistinguishable from the mathematical idealization of an infinitesimally small perturbation with jump conditions for thermodynamic variables.

In solids, physical shock waves are mechanical waves of finite amplitudes and arise when condensed matter is subjected to a rapid compression. Shock waves can be defined by several major distinctive properties as follows:

- A pressure-dependent, supersonic velocity of propagation.
- The formation of a steep wave front with a sudden change of thermodynamic quantities.
- Non-linear superposition properties (for reflection and interaction).
- A strong decrease of propagation velocity with increasing distance from the center of the origin for the case of non-planar shock waves.

Sometimes another criterion for a shock wave is listed in shock wave literature which is the extremely short rise time of the pressure within tens of nanoseconds. However, this is not a defining criterion of shock waves, because no generally agreed upon definition exists of what “extremely short” really is supposed to mean – it is a term of rather subjective nature. A nanosecond rise time certainly applies for lithotripter shock waves which are used in medicine as a non-invasive technique to comminute calculi³² and for other therapeutic purposes³³; however, in the geologic realm for example, meteorite impacts, explosive volcanic eruptions and earthquakes can provoke drastic and irreversible changes within seconds.

One characteristic that distinguishes a shock wave from an ordinary sound wave is that the initial disturbance in the medium that causes a shock wave is always traveling at a velocity greater than the phase velocity of sound in the medium (the electromagnetic analog of this is called Cherenkov radiation).³⁴ Because a shock wave moves faster than the speed of sound, the medium ahead of the shock front cannot respond until the shock strikes, and so the shock wave falling upon the particles of matter initially at rest, is a *supersonic phenomenon*.

Shock Waves Produced by Lithotripters

Since its invention in the early 1980s, Extracorporeal Shock-wave Lithotripsy (ESWL) has evolved as a clinical standard, which is widely used as the only non-invasive surgical technique to eliminate e.g. kidney stones and other urinary calculi.³³ Rassweiler et al³⁵ describe the multiple mechanisms associated with stone disintegration by ESWL as well as current advances in in-

strumentation and clinical praxis. A shock wave is a mechanical wave that induces a transient pressure rise and propagates at a speed above the speed of sound of the corresponding medium. It is created by means of a piezoelectric, electro-hydraulic or electromagnetic transducer, called lithotripter, which generates focused high-amplitude pressure waves in a contact medium outside the body.^{35,36} The patient is positioned such that the stone is brought into the focus of the pressure wave. When the acoustic energy deposited in the focal region is high enough, cavitation bubbles filled with vapor or gas form and collapse violently. This collapse results in formation of a shock wave that in turn disintegrates the stone. Apart from stone destruction, ESWL can cause tissue injury as unwanted adverse effects during treatment.³⁷ The physical mechanisms related to the cavitation phenomenon that cause both stone destruction and tissue damage are very complex, not well understood and hardly experimentally controllable.^{35,37-39} The fact that ESWL can cause tissue damage, inspired experiments that applied lithotripter induced shockwaves to tumors *in vivo*. While several first studies in animal models did not show any impact of shock waves on tumor growth,³⁶ some results seemed encouraging, for example a delayed tumor growth in mice⁴⁰ and even complete remission of dorsal skin tumors in hamsters.⁴¹ However, up-to-date shock wave treatment has not been used in clinical trials, most likely because the cavitation phenomenon is very hard to control and the unspecific effects on ESWL on cells cause the need for live imaging techniques during treatment. Parallel to the *in vivo* experiments on tumors, a large number of *in vitro* studies on different cell lines in culture were performed as reviewed by Coleman and Saunders,³⁶ and Delius.³⁹

The application of several hundred shock waves created by commercial lithotripter systems causes cell death. Most striking for a possible shock wave based tumor therapy was a study on different normal and malignant cell lines, which showed no selective effect.³⁸ When the energy deposited by the lithotripter is reduced below the lethal value, it is possible to permeabilize the cells without killing them.⁴²⁻⁴⁶ In this way, molecules present in the surrounding medium can diffuse into the cells. This effect has possible applications for drug delivery and gene transfer.⁴⁷ In more recent studies, adherently grown cells on transparent substrates were exposed to shock waves and analyzed with (fluorescence) microscopy. In direct vicinity of the cavitation bubble, the cells are completely destroyed and detached from the surface. Cells close to the bubble were permanently permeabilized and killed, whereas cells further away from the bubble survived.^{48,49} This behavior could be connected with deformations of the cytoskeleton.⁵⁰ Generally speaking, ESWL treatment of cells seems to be only poorly controllable because of the cavitation process and no selective effects on cells are observed. These disadvantages might be overcome by the technique of laser-induced shockwave generation discussed in the next section, which is based on purely mechanical destruction of cells, where no cavitation effects occur.

Laser-Induced Shock Waves

When irradiating an absorbing material with a pulsed laser, the optical energy deposited on the absorber is transformed into mechanical energy. A shock wave forms at the surface and then travels the absorber.⁵¹ The shock wave properties such as rise time, velocity of propagation or peak pressure depend on the absorbing material and the laser parameters. For one specific laser/absorber system, the peak stress of the shock wave can be tuned by varying the laser fluence that is equal to the total energy deposited per area of illumination.⁵²⁻⁵⁴ In this experimental configuration, well-defined, reproducible shockwaves can be generated without the side effect of heating or cavitation.⁵⁵ Thus, the pure mechanical effect of the shockwave on the cells can be investigated. As reviewed by Yao et al,⁵⁶ also Laser-Induced Shockwaves (LISW) are able to render the cell membrane permeable, giving rise to drug delivery and gene transfection. The application to whole tissue structures is also possible. For example, transdermal insulin delivery by LISW results in a reduction of the blood glucose level without causing any pain to the patient.⁵⁷ Here, we focus on the direct lethal effect of LISW on cells. In the following, we review the literature concerning the impact of LISW on cells and present current progress and novel developed techniques that will help to further classify the properties of LISW.

In Table 1, we provide an overview of major studies

that investigated the biological effects of the interaction of shock waves (or strong pressure waves) with biological cells.

Figure 1 shows the basic features of the experimental setups used in several studies reported in the literature.^{60-62,65,66,69} The laser beam is directed onto the bottom of a cell culture vessel, that consists of an absorbing material. Upon illumination with the laser, a shock wave is formed that travels into the vessel, and interacts with the cells. For one specific cell line, it turned out that the survival rates of cells exposed to LISW depend on stress gradient $\sigma = p_{max} / \tau_R$, where p_{max} is the peak pressure and τ_R is the rise time of the shock wave.⁶⁰ However, the survival rates among different cell lines differ remarkably at constant physical parameters p_{max} and τ_R . For example, only 50% of transformed (immortalized) retinal pigment epithelium cells survive exposure to shock waves with $p_{max} = 74$ MPa and $\tau_R = 10$ ns. However, 100% of normal retinal pigment epithelium cells survive this procedure.⁶⁰ A shock wave with $\tau_R = 10$ ns and $p_{max} = 30$ MPa kills 50% of mouse breast sarcoma cells, whereas human promyelocytic leukemia cells survive this exposure.⁶⁹

All of the above mentioned studies in Table 2 had major deficiencies in the techniques used to characterize the physical conditions in the vessel. Usually, the pressure profiles are measured with piezoelectric elements (Polyvinylidene fluoride, PVDF) either in form of needle hydrophones or piezoelectric films that are brought in contact to the surface of the culture

Cell type	Type of study & number of pulses	Maximum pressure level & method	Reference
Lymphocytic mouse leukemia cells L1210	<i>In vitro</i> ; cells in suspensions and immobilized in gelatin; 125 to 500 pulses	Dornier XL1 lithotripter; 38.6 MPa	Brümmer et al ⁵⁸
Human renal cell carcinoma RC-8, grown in the mouse	<i>In vivo</i> ; series of 3-200 pulses with pulse duration of 1.5 at 10Hz	Laser ablation (polyimide target) with a Candela LDFD/3 flash lamp pumped dye laser	Reijke et al ⁵⁹
Mouse breast sarcoma cells EMT-6	<i>In vitro</i> ; 25-240 mJ pulse energy; up to 50 pulses	Laser ablation (polyimide target) with ArF/KrF excimer laser; 35-65 MPa	Doukas et al ⁶⁰
Mouse breast sarcoma cells EMT-6	<i>In vitro</i>	Laser ablation (polyimide target) with ArF excimer laser; 30 MPa	Lee et al ⁶¹
Human retinal pigment epithelium cells RPE	<i>In vivo</i> ; 5-150 pulses	Laser ablation (polyimide target) with ARF/KrF excimer laser; 74 MPa, max. 240 mJ	Douki et al ⁶²
HeLa cells	<i>In vitro</i> ; 360 pulses	Siemens lithostar lithotripter; 69.5 MPa	Huber et al ⁶³
Human bladder tumor cells HT-1197	<i>In vitro</i> pulses; 500	Dornier HM-3 lithotripter	Kohri ⁶⁴
Human red blood cells RBC	<i>In vitro</i> ; 5 pulses	Laser ablation (polyimide/polystyrene target) with Q-switched ArF excimer laser; 60 MPa, max. 350 mJ	Mulholland et al ⁶⁵
Mouse breast sarcoma cells EMT-6 and human red blood cells RBC	<i>In vitro</i>	Laser ablation (polyimide target) with ArF excimer laser and Q-switched ruby laser (polystyrene target) 60 MPa	Lee et al ⁶⁶
Mouse tumor cells SW480	<i>In vivo</i>	Piezo-ceramic elements; 40 MPa	Kato et al ⁶⁷
Human endothelial cells HUVEC	<i>In vitro</i>	Nd-YAG laser (copper target) 23 MPa, max. 5.9 mJ	Sondén et al ⁶⁸
HeLa cells	<i>In vitro</i>	ESWL, 28 MPa	Ohl et al ⁶⁸

Table 1: Overview of studies that involved the shock wave exposure of tumor cells. Unfortunately, as can be seen from this compilation of studies, no systematic investigation of biological shock wave effects in different types of cell lines with a very well-defined and reproducible method ever seems to have been conducted. Also the achieved maximum pressure levels of the shock waves and their rise times were not measured in all of the studies.

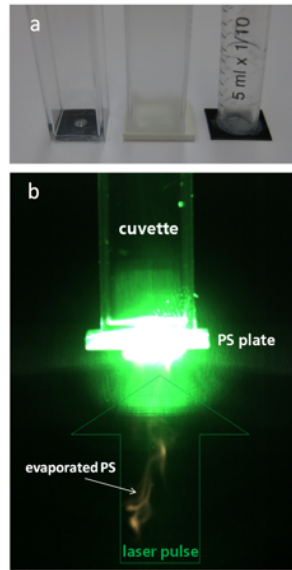


Figure 1: (a) Basic elements of the experimental setups used to study the effects of laser induced shock waves on cells.^{36,49-53} (b) A pulsed laser beam irradiates an absorbing material at the bottom of the vessel (usually a polymer) that contains the cells and their growth medium. At the surface of the absorber, a shock wave is formed that moves forward into the vessel. When the absorbing material is covered with a transparent material facing the laser, the peak pressure of the shock wave is further enhanced.⁵³ In recent breakthrough experiments, Schmidt et al⁷² managed to optimize this setup by using standard multi well culture vessels and black varnish as absorber material. Pressure levels in the cells beyond 80 MPa were achieved, which is well above the pressure levels in all previous studies reported in literature.

System	Microstructure	Method of characterization	Models or constitutive equation	References
Polymer melts	Entangled macromolecules	Dynamic moduli, <i>via</i> shear, viscosity	Reputation theory, viscoelasticity, Maxwell model, Dumbbell model	deGennes ⁷⁶ Doi and Edwards ⁸¹ Bird ⁸² Larson ⁸³
Elastomers	Crosslinked networks of polymers	Dynamic moduli	Gel-type models, yield stresses	Winter and Chambon ⁸⁴
Polymer solutions	Dilute solutions containing polymer chains	Solvent viscosity and intrinsic viscosity	Models for solution and polymer separately	Bird et al ⁸²
Gels with polymers or particles	Network with crosslinks	Yield stress, elasticity (below yield), microrheology	Percolation, fractal dimension	Flory ⁸⁵ deGennes ⁷⁶ Winter and Chambon ⁸⁴
Suspensions, emulsions, micellar solutions	Particles in fluids	Yield stress, viscosity, diffusion	Percolation, particle orientation, small-deformation theory, yield stress	Einstein ⁸⁶ Oldroyd ⁸⁷

Table 2: Rheological properties of a few complex systems that can be used for upscaling in multiscale modeling of cellular soft matter.

vessel. In both cases, a transfer medium (either water or grease) serves as the acoustic contact to the piezoelectric element. However, shock waves are known to decay very rapidly (within micrometers) in liquids and tissue.⁷⁰ Thus, the need for a fluid as contact medium may lead to wrong pressure measurements and it would be desirable to determine shock wave properties on a microscopic scale, rather than with a PVDF sensor of millimeter dimensions. An alternative to determining the pressure profiles with piezoelectric element is to use optical methods that measure the velocity profile of the vessel bottom while the shockwave passes. From this velocity profile the pressure profile in direct vicinity of the bottom plate can be calculated. This information is particularly interesting when studying adherently grown cell cultures. Strand et al⁷¹ developed a cost efficient and compact high-speed velocimetry system that uses a heterodyne detection method.

An optical fiber is used to transport Laser light to a probe that contains a lens. The light is then focused onto the moving surface that reflects or scatters light back into the probe from where it is brought to a detector. The frequency of the light is now Doppler-shifted because of the surface movement. At the detector, it is mixed with non-Doppler shifted light to generate a beat signal that contains the velocity information of the moving surface. In a recent breakthrough application, velocity profiles have been measured in this way and could also serve as input for simulations that computed the pressure fields within the whole vessel with high time resolution.⁷² In this way, the conditions that the cells are exposed to during the shock wave experiment can be characterized on the relevant length and time scales which are micrometers and nanoseconds. For beam diameters of a few millimeters, in the author’s laser lab, with an optimized experimental setup, peak pressures up to approximately 120 MPa were

obtained which is considerable beyond the pressure levels of all previous studies discussed in literature, see Figure 2.

COMPUTATIONAL MULTISCALE MODELING OF CELLS AND TISSUES

Exploring the potential of shock waves for destroying or damaging cancer cells possibly opens a new or complementary road for tumor treatment, avoiding the disadvantages of currently established methods for tumor treatment based on US, and using only the *mechanical* destructive effects of a shock wave interacting with cells. By way of using the mechanical effects of shock waves rather than relying on heating of tissue, it seems possible to destroy or damage the cytoskeleton or the membrane, as shock waves carry much more energy in a much shorter time interval than US waves do. This might open new perspectives for cancer therapies in addition to existing treatments. The complexity occurring in the interaction of shock waves with soft, biological matter requires a combined approach using experi-

mental and numerical methods which is exemplified in Figure 3. To model the mechanical properties of eukaryotic cells, a focus is set on the two salient features of cells that determine their mechanical behavior: the cytoskeleton (composed of a network of macromolecules) and the plasma membrane (composed of double lipid layers).

Considered from a physical perspective, living organisms such as eukaryotic cells or neoplasia are far more complex systems than typical engineering materials such as metals, ceramics, polymers or semiconductors, see Figure 4. They are dynamic and provide integrated functions that include metabolism, reproduction, growth, sensing, communication, control, and apoptosis (programmed cell death).

Different studies have established the connections between structure, mechanical responses and biological functions of different organs and tissues including, for example, the heart, lung, bone, cartilage, blood vessel, and skeletal and cardiac mus-

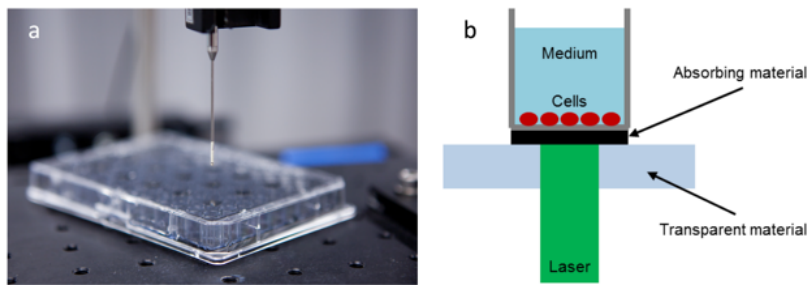


Figure 2: Optimized setup used in recent breakthrough experiments by Schmidt et al.⁷² (a) Ordinary multiwell cell culture plates were used (positioned here on an optical table) and U87 glioblastoma cells were grown adherently on the bottom of the individual wells. The achieved pressure levels were measured directly in the wells by means of PVDF hydrophones with nanosecond time resolution. (b) By using black varnish as absorber material, it was possible to reach pressure levels in the cells beyond 100 MPa which is well above the pressure levels achieved in all previous studies reported in literature. For U87 glioblastoma, it was found that a biological destructive effect occurs above 80 MPa, which is a pressure level well above the ones achieved in all previous experimental studies reported in literature, cf. Table 1. One great advantage of the setup shown here, is its reproducibility in both, the pressure level measurement by using very well-defined single laser pulses per well and the level of destruction in the cells which was verified by cell counting and a long term MTA-analysis over several days, i.e. over several cell cycles with negative results (i.e. no destruction) in the untreated controls.

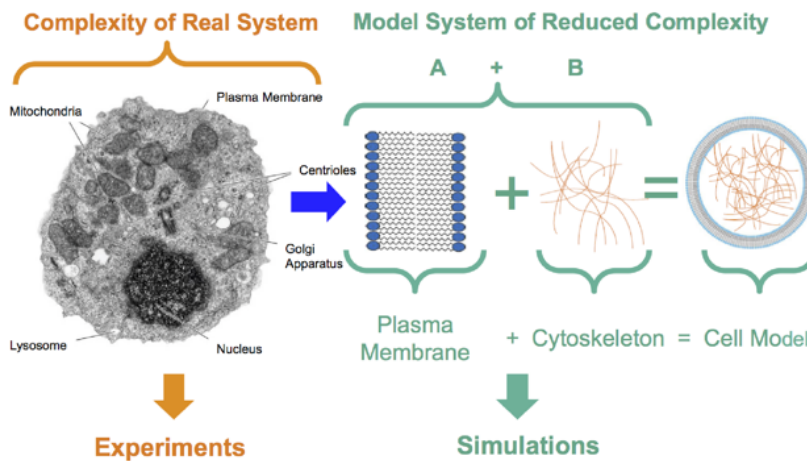


Figure 3: An integrated approach combining the full complexity of the real experimental system with computational coarse-grained (CG) models of extremely reduced complexity. In CG models, typically, only two major components of cells determining their mechanical properties relevant for their interaction with shock waves are considered: The plasma membrane and the cytoskeleton. Figure taken from Steinhauser.⁷³

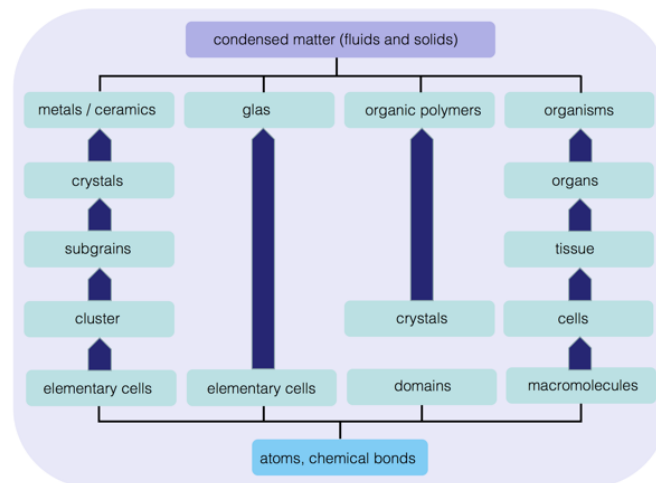


Figure 4: Multistage aspects of different classes of engineering and organic materials, i.e. of condensed matter. Living organisms involve many different features on different length and time scales. Both, engineering materials and living matter are made from the same constituents, i.e. atoms being held together by chemical bonds. Figure taken from Steinhauser.⁷⁷

cles.⁷⁴ These studies have led to better diagnosis and treatment of orthopaedic, cardiovascular and respiratory diseases by providing a greater understanding of how the biological functions of the body are related to bio-solid and bio-fluid mechanics. To decipher the fundamental mechanisms of biological materials, however, more systematic studies of deformation, structural dynamics and mechanochemical transduction in living cells and biomolecules are needed. The mechanics of biological molecules, including proteins and nucleic acids, is crucial to understanding the connection between structure and function in cellular and tissue mechanics. Still in its infancy, this emerging field of bio-mechanics strives to understand the deformation and mechanics of macroscopic tissue structures based on the deformation and mechanics of bimolecular. A recent summary of current multi scale simulation approaches for bridging the scales from sub-cellular components to tissue is provided in a recent review by Steinhauser.⁷³

MECHANICAL PROPERTIES OF COMPLEX MATERIAL SYSTEMS

Upscaling of atomistic and microscopic simulation approaches of the kind as displayed in Figure 5, is one way of trying to understand the basics of shock wave effects on soft matter systems such as cells and living tissue.⁷⁵ There are a number of complex microscopic systems, which are relevant to the study of animal or human cells, and which form the basis of any physical, and mathematical-numerical modeling, since the systems we are interested in build a complex system made of polymer melts and solutions, suspensions, gels and micelle systems. The microstructure of these systems is very important for the elaboration of constitutive equations on a coarse-grained, phenomenological level.

In Table 2, we review and summarize some of the key rheological properties of a few of these systems. For example,

polymers are viscoelastic and may become viscoplastic in some cases when they form a gel (polymer network). They are present in a cell in the form of proteins and play a fundamental role for many cell functions and cell-cell interactions. The basic microstructure of a polymer network consists of chains intermingled with each other (entanglements) with a few weak reticulation points, as well as loops or dangling ends.⁷⁶ Gel materials are interesting systems, because the cell cytoplasm may be regarded as a gel. Elastomers are slightly different and may be considered as viscoelastic solids, in particular, because they cannot flow at very low shear rates. This is mainly due to strong links (covalent sometimes) associating polymer chains thus creating a network which behaves elastically over a wide range of shear rates.

On the nanoscale, their microstructure looks something like a regular net. As the frequency is increased, they undergo a glassy transition where moduli G' and G'' behave as ω^n , where n is an exponent whose value is close to 0.6. Polymer solutions are solutions containing polymers in a solvent and do not exhibit entanglements in this regime. They may be considered to have two components, one being the solvent (which is viscous with constant viscosity η) and the other one being the polymer with viscoelastic properties. The field of suspensions is quite large, because it can describe particulate suspensions, but can also lead to fluid-fluid suspensions called emulsions, and all kinds of systems including deformable objects in a fluid. For example, blood is a mixture of white and red blood cells, platelets and other constituents included in the plasma.

Most of the biological cells are 1-100 microns in size, and they comprise many constituents, Figure 5. The cell is covered by a phospholipid bilayer membrane reinforced with protein molecules, and the interior of the cell includes a liquid phase (cytosol), a nucleus, the cytoskeleton consisting of networks of microtubules, act in and intermediate filaments, organelles of different sizes and shapes, and other proteins, Figure 5. The re-

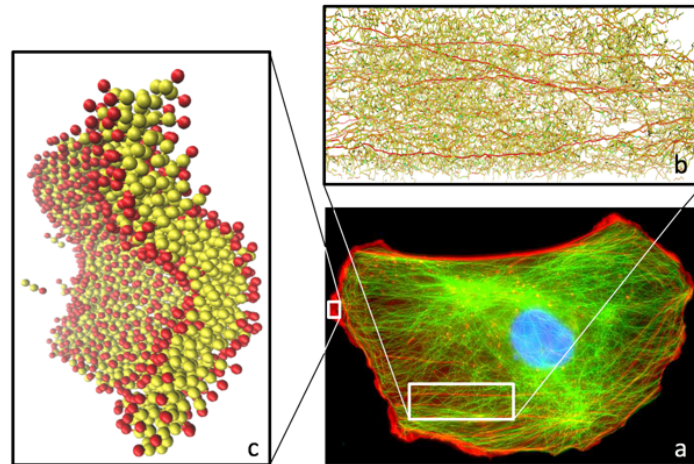


Figure 5: Microscopic modeling and simulation approaches for the cytoskeleton and the amphiphilic plasma membrane of eukaryotic cells. (a) Image of a mouse NIH3T3 fibroblast cell, fixed and stained for DNA (blue) and the major cytoskeleton filaments act in (red) and alpha-tubulin (green). Figure reproduced with permission from Suresh et al.⁴ (b) Modeling approach for the cytoskeleton as a meshed network of polymers. Simulation snapshot generated in the Steinhauser-lab with the molecular dynamics software-suite MD-CUBE,⁷⁸ showing a stretched three-dimensional polymer network.⁷⁹ Color code indicates forces in the bonds of the polymers with red: very large force just before bond failure, and green: force-free bonds. (c) A simulation of the self-assembly of a three-particle amphiphilic lipid model (hydrophilic part of the lipid: red, hydrophobic part: yellow) where the lipids self-assemble to form bilayers. Subsequently, these equilibrated bilayers are exposed to strong shock waves.⁸¹ Simulation snapshot adopted from Schindler et al.⁸⁰

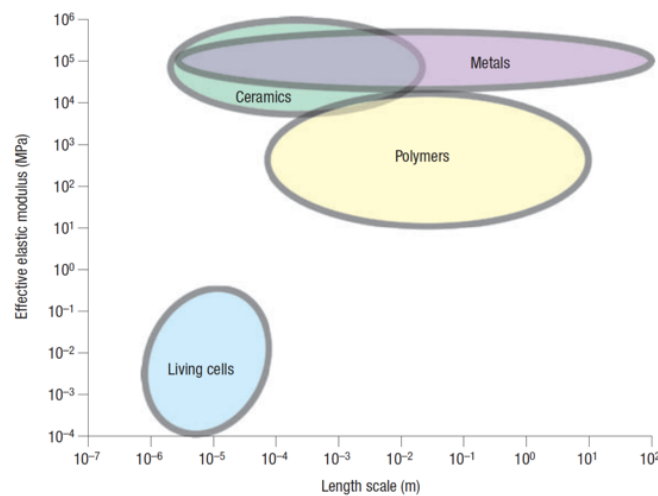


Figure 6: Approximate range of values for the elastic modulus of biological cells and comparisons with those of engineering metals, ceramics and polymers.

sistance of single cells to elastic deformation, as quantified by an effective elastic modulus, ranges from 102 to 105 Pa, see Figure 6, which is orders of magnitude smaller than that of metals, ceramics and polymers. The deformability of cells is determined largely by the cytoskeleton, whose rigidity is influenced by the mechanical and chemical environments including cell-cell and cell-Extracellular Matrix (ECM) interactions.

If the elastic, visco-plastic properties of the basic constituents of cells and tissue are known, there is a variety of techniques to produce constitutive equations for a macroscopic description, such as ensemble averaging,^{88,89} mathematical homogenization,⁹⁰ effective medium theory,⁹¹ or temerity models which are based on the idea to model deformable structures by using sticks and strings under tension.⁹²⁻⁹⁷

It was shown that this approach is particularly well adapted for the description of eukaryotic biological cells.⁹⁸ However, the previously listed techniques are usually not able to account for specific interactions between cells, their individual, specific behavior or the active response of cells to external stimuli.

Another, more direct way of modeling shock wave effects in tissue and cells is to use macroscopic models based on continuum theory rather than upscaling basic properties. Continuum models, e.g. based on finite elements meshes neglect almost all details of the discrete nature of the constituents of cells and tissue but allow for a macroscopic simulation of deformation upon exposure to shock waves. The quality of these type of simulations however, is very strongly depending on the employed

phenomenological material model and additional complexity is to be considered here, because of the local heterogeneity of tissue and a general lack of experimental measurements *in vivo*. Generally speaking, it is at least questionable, whether experimental *in vitro* studies of tissue behavior have real physiological relevance.

MECHANICAL PROPERTIES OF SOFT BIOLOGICAL TISSUES

For many years, researchers have devoted their attention to the study of animal tissues, and important issues have been raised. Finding constitutive relations for such media is not simple, because tissues can behave as elastic, plastic, viscoelastic or viscoplastic materials. One of the most important conclusion is that relating the microstructure with its macroscopic nature is a fundamental problem which forms the basis of any continuum mechanics problem.⁸³ The relevant sciences studying such aspects are rheology^{83,99,100} and biomechanics.¹⁰¹⁻¹⁰⁴

These two fields are actually very close to each other when it comes to dealing with biomaterials, and defining their minor differences here is not my intention. One may say that generally one is interested in finding relationships between the applied forces and the relevant deformations or flows involved in problems dealing with living materials. Classical models (1D), which can be used and can depict the cytoplasm of a cell, are usually viscoelastic or viscoplastic ones. 3D-viscoelastic models can exhibit differential forms, or integral formulations (sometimes equivalent). Other models like viscoplastic ones can also be interesting because they allow us to deal with systems with cross-links, somehow close to gels; in particular, polymers and networks play a role inside the cytoplasm, Figure 5a and 5b. So, at a certain level, we may assume that the size of the system studied is large enough, where is the size of an element at the microscopic level, so that the system exhibits a macroscopic, averaged behavior and can be described using a constitutive relation as it is done in typical, empirical engineering approaches for material modeling.

Generally speaking, material models have to include the following material behavior (listed in increasing order of complexity):

1. Linear elasticity.
2. Hyperelasticity.
3. Hyperviscoelasticity.

Many computational approaches only include hyperelasticity. The general description from which such models start, is the Ogden hyperelastic material model¹⁰⁵ which assumes the existence of a strain energy function in the form:

$$E = \sum_{p=1}^n \frac{\mu_p}{\alpha_p} (\lambda_1^{\alpha_p} + \lambda_2^{\alpha_p} + \lambda_3^{\alpha_p} - 3)$$

where $\lambda_i^{\alpha_p}$ are the principal stretches, n and α_p are material constants, and μ_p denotes the shear modulus of the material

in the undeformed state. We note that the often used Mooney-Rivlin material model,^{106,107} which assumes that can be written as the sum of two invariants, is contained in the above formula as a special case.

Therapeutic technologies such as focused US and shock wave treatment, have an extremely localized area of therapeutic effect and therefore have to be applied directly over specific location of anatomic/functional abnormality, precisely in relation to the current (i.e. intra-operative) patient's anatomy. As surgical intervention tends to distort the pre-operative anatomy and often leads to misalignment between the actual position of pathology and its position determined from pre-operative images, an image-guided surgery requires intra-operative images and/or update of the pre-operative images to the current position of the brain internal structures. To achieve an accurate image update, deformations of the abdominal organs (e.g. the brain, the liver or the kidneys) must be taken into account. Since the late 1990s, significant research effort has been directed towards the prediction of such deformations using biomechanical models.¹⁰⁸⁻¹¹⁵ Typically, in such models, the Finite Element (FE) method¹¹⁶⁻¹¹⁹ is employed to discretize and solve the related differential equations of continuum mechanics, see Figure 7. During image-guided surgery, only low-quality, sparse information about the current tissue position is available.¹²⁰ This information can be used to warp high-quality pre-operative images, such that they correspond to the momentary situation, by computing the deformation field within the brain using a biomechanical constitutive model.

In a comparative study by Wittek et al¹¹⁴ it was shown that the actual choice of a specific material model hardly influences the calculated displacements of tumors. Between different models, the differences in displacement amounted to less than 0.2 mm. It seems that the organ displacement is dominated by its weak compressibility rather than the resulting stresses. Many different experimental setups and different theoretical descriptions are used to extract mechanical parameters from tissue measurements. We end this review by listing the results of various such studies in Table 3. One way of comparing these different results is to calculate Young's modulus based on local linear elasticity.

CONCLUSIONS AND FUTURE PERSPECTIVES

As a clinical tool, within its limits of applications, HIFU is established as a therapeutic tool. As this technique becomes more widely available, it should be possible to coordinate the type of clinical trials that will be necessary to develop the evidence base for the efficacy of HIFU in its various applications, whether alone or in combination. Real-time imaging and treatment monitoring are the subjects of ongoing theoretical research, and the development of techniques such as three-dimensional ultrasound and elastography which measures the change in stiffness of a tissue as it is ablated, are likely to enable improvement in clinical

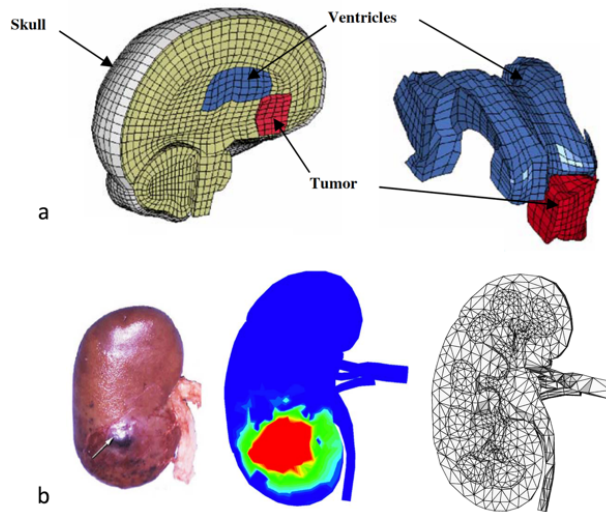


Figure 7: FE applications for modeling the deformation of tissue as a reaction to being exposed to shock waves. (a) FE model of specific meshes of a left hemisphere of a human brain including ventricles and tumor (red). The entire mesh comprises of 16,925 nodes, 15,031 hexahedral (8-noded bricks) and 19 pentahedral elements. The elements' characteristic length varied between 0.6 and 6 mm. (b) From left to right: Typical kidney injuries after an ESWL treatment observed on an adult pig kidney,¹²¹ and the computed field of irreversible volumetric expansion in an exterior view. Meridional section of an anatomically correct finite element mesh of the kidney. The photograph illustrates how difficult it is to generally quantify the amount of tissue injury.

Species	Technique	Model	Young's modulus (kPa)	Reference
Rabbit (<i>in vitro</i>)	Indentation		5.6	Yamada ²⁵
Deer (<i>in vitro</i>)	Indentation, max 20 mm	Linear/nonlinear/viscoelastic	25	Schwartz et al ¹²²
Porcine (<i>in vivo</i>)	Aspiration	Hyperelastic, viscoelastic	90	Nava et al ¹²³
Procine (<i>in vivo</i>)	Indentation, max 500 μ m	Linear	10-15	Ottensmeyer ¹²⁴
Tissue scaffold (<i>in vitro</i>)	AFM nanoindentation		11.6	Zhu et al ¹²⁵
Porcine (<i>in vivo</i>)	Indentation, max 8 mm		13	Tay et al ⁷⁶

Table 3: Mechanical, experimental data on the liver of several studies that may be used as input and for validation of computer simulation approaches that mimic the mechanical behavior of biological tissue.

outcome and to bring about a reduction in treatment duration. In addition, focused ultrasound has been proposed as a vehicle for delivering targeted gene therapy through inducing cavitation of DNA-laden micro bubble contrast agents in the periphery of the zone of ablation, where temperature rises would be sublethal, but these remain secondary considerations to the direct ablative treatment intent at present.

The experimental observation that shock waves are able to destroy cells *in vitro* and to delay tumor growth *in vivo* motivates further studies of the responsible mechanisms. The author believes that characterization of shock wave impact on the cellular level is necessary to understand these processes more systematically. Laser-induced methods for shock wave generation have proven to be reproducible on the macroscopic level and to avoid lithotripter related side-effects such as heating and cavitation. Newly developed optical methods together with multiscale modeling approaches can give insights on the precise conditions that the cells are exposed to during shock wave impact. The knowledge of these conditions is a prerequisite to find and maybe control selective effects on cells. The diverse behavior shown by different cellular strains poses the need to find quantities that

relate cellular properties with shock wave induced killing. Thus, in parallel to shockwave experiments on different cell lines, specific quantities have to be found that relate cellular properties with shockwave impact. Of course, mechanical properties related to the cytoskeleton serve as a first promising candidate and may be determined with combined cell-mechanical and fluorescent microscopic observations. In addition to the experiments on cells, another possible application of shock waves emerges from current biological findings that relate tumorous growth to mechanical properties of tissue. It has long been known that tumors are more stiff than healthy tissue. This fact is even used to detect mammary cancer, for example by palpation or elastography of rigid tissue structures. The mechanical properties of tissues are mostly influenced by the ECM, which mainly consists of collagen. These molecules are produced inside the cells and delivered to the ECM where they form polymeric structures that serve as scaffolds for the cells. When healthy tissue turns into a tumor, the polymeric structure of collagen fibrils is significantly altered, causing a stiffening of the ECM.⁸¹ Cells possess mechanoreceptors that detect physical forces and transform them into biochemical signals.⁸² Thus, cells are able to both sense and alter the mechanical properties of the ECM.⁸³ Interestingly, the bio-

chemical signaling pathway of the mechano-sensing apparatus cross-talks with major pathways that control cell proliferation and it was shown that tissue stiffness promotes cancerous cell growth.⁸⁴ In this way, ECM stiffening and tumor growth form a positive feedback loop that enhances the risk of tumor formation.⁸² On the other hand, these current findings may open new possibilities of cancer therapy basing on *mechanical* methods, i.e. based on the physics of cancer rather than or in addition to pharmaceutical treatments. One of these interesting possibilities of shock waves therapy based on mechanical effects alone, is its potential to be used for gene transfection and molecular drug delivery, which involves interesting physical chemistry research concerning the structure of molecules to be used as drug carriers.⁸⁵

Within the biological sciences, cancer is highlighting the need for interdisciplinary research. There is a growing realization that cancer is a problem requiring input from a wider community of scientists, i.e. physicists, mathematicians and computer engineers. This is reflected in increasing interdisciplinary collaborations around the world, involving biologists, clinicians, physicists, mathematicians and computer scientists, which aim to give new insights into cancer and improvements in its treatment.

In a fashion quite analogous to studies of mechanics of engineering materials, the emerging field of cell and molecular mechanics of biological materials seeks to establish essential linkages between microscopic structure and macroscopic mechanical properties. New multiscale computational approaches have emerged in recent years, coupling e.g. atomistic scale simulations with the macroscopic domain as reviewed in Steinhäuser⁷⁶ and also new numerical approaches combining coarse-grained macromolecular models of bio-molecules with shock wave physics emerged.⁸⁴ Although methods have been developed to measure cell responses during deformation, cell-adhesion, locomotion and mitosis, reliable experimental tools are currently unavailable for quantifying the distribution of mechanical forces between various subcellular structures as well as on individual proteins and nucleic acids inside a cell.

In summary, progress in experimental and computational biology and biomechanics during the past decade has provided unprecedented opportunities to probe the mechanical responses of cells, proteins and DNA molecules. How the forces and deformations associated with these basic structural units of life can be described by physical models, engineered by chemistry and implemented in computer programs, is a topic of substantial scientific excitement and interdisciplinary opportunity.

ACKNOWLEDGEMENTS

The author acknowledges financial support of the Fraunhofer-Gesellschaft, ex., Germany, under grant No. 600016 (Shock Wave Induced Destruction of Tumor Cells), and grant No. 400017 (Extracorporeal, Focused Ultrasound Therapy: Effec-

tiveness, Simulation, and Planning of New Therapies). Interesting discussions with Constantin Coussios from Oxford University in the UK during my visit there, are gratefully acknowledged.

REFERENCES

1. Mendelsohn J, Howley PM, Israel MA, Gray JW, Thompson CB. *The Molecular Basis of Cancer*. Philadelphia, PA, USA: Elsevier Science; 2014.
2. Blagosklonny MV, Robey R, Bates S, Fojo T. Pretreatment with DNA-damaging agents permits selective killing of checkpoint-deficient cells by microtubule-active drugs. *J Clin Invest*. 2000; 105(4): 533-539. doi: [10.1172/JCI18625](https://doi.org/10.1172/JCI18625)
3. Pearson OH, Manni A, Arafah BM. Antiestrogen treatment of breast cancer: An overview. *Cancer Res*. 1982; 42(8 Suppl): 3424s-3429s. Web site. http://cancerres.aacrjournals.org/content/42/8_Supplement/3424s.short. Accessed July 24, 2016
4. Suresh S. Biomechanics and biophysics of cancer cells. *Acta Biomater*. 2007; 3(4): 413-438. doi: [10.1016/j.actbio.2007.04.002](https://doi.org/10.1016/j.actbio.2007.04.002)
5. Guck J, Schinkinger S, Lincoln B, et al. Optical deformability as an inherent cell marker for testing malignant transformation and metastatic competence. *Biophys J*. 2005; 88(5): 3689-3698. doi: [10.1529/biophysj.104.045476](https://doi.org/10.1529/biophysj.104.045476)
6. Fuh G, Cunningham BC, Fukunaga R, Nagata S, Goeddel DV, Wells JA. Rational design of potent antagonists to the human growth hormone receptor. *Science*. 1992; 256(5064): 1677-1680. doi: [10.1126/science.256.5064.1677](https://doi.org/10.1126/science.256.5064.1677)
7. Gardel ML, Valentine MT, Crocker JC, Bausch AR, Weitz DA. Microrheology of entangled F-actin solutions. *Phys Rev Lett*. 2003; 91(15): 158302-158302. doi: [10.1103/PhysRevLett.91.158302](https://doi.org/10.1103/PhysRevLett.91.158302)
8. Gardel ML, Schneider IC, Aratyn-Schaus Y, Waterman CM. Mechanical integration of actin and adhesion dynamics in cell migration. *Annu Rev Cell Devel Biol*. 2009; 26: 315-333. doi: [10.1146/annurev.cellbio.011209.122036](https://doi.org/10.1146/annurev.cellbio.011209.122036)
9. Dunn BB. Cancer: Solving an age-old problem. *Nature*. 2012; 483(7387): S2-S6. doi: [10.1038/483S2a](https://doi.org/10.1038/483S2a)
10. Lackey L, Peterson C, Barr RG. Contrast-enhanced ultrasound-guided radiofrequency ablation of renal tumors. *Ultrasound Q*. 2012; 28(4): 269-274. doi: [10.1097/RUQ.0b013e318274de66](https://doi.org/10.1097/RUQ.0b013e318274de66)
11. Goyal J, Verma P, Sidana A, Georgiades CS, Rodriguez R. Single center comparative oncologic outcomes of surgical and percutaneous cryoablation for treatment of renal tumors. *J Endourol*. 2012; 26(11): 1413-1419. doi: [10.1089/end.2012.0244](https://doi.org/10.1089/end.2012.0244)

12. Vogl TJ, Straub R, Eichler K, Söllner O, Mack MG. Colorectal carcinoma metastases in liver: Laser-induced interstitial thermotherapy-local tumor control rate and survival data. *Radiology*. 2004; 230(2): 450-458. doi: [10.1148/radiol.2302020646](https://doi.org/10.1148/radiol.2302020646)
13. Suhr F, Delhasse Y, Bungartz G, Schmidt A, Pfannkuche K, Bloch W. Cell biological effects of mechanical stimulations generated by focused extracorporeal shock wave applications on cultured human bone marrow stromal cells. *Stem Cell Res*. 2013; 11(2): 951-964. doi: [10.1016/j.scr.2013.05.010](https://doi.org/10.1016/j.scr.2013.05.010)
14. Carome EF, Clark NA, Moeller CE. Generation of acoustic signals in liquids by ruby laser-induced thermal stress transients. *Appl Phys Lett*. 1964; 4(6): 95-97. doi: [10.1063/1.1753985](https://doi.org/10.1063/1.1753985)
15. Krehl POK. *History of Shock Waves, Explosions and Impact: A Chronological and Biographical Reference*. Berlin, Germany: Springer; 2009.
16. Steinhauser MO, Hiermaier S. A review of computational methods in materials science: Examples from shock-wave and polymer physics. *Int Mol Sci*. 2009; 10(12): 5135-5216. doi: [10.3390/ijms10125135](https://doi.org/10.3390/ijms10125135)
17. Rodriguez V, Saurel R, Jourdan G, Houas L. Solid-particle jet formation under shock-wave acceleration. *Phys Rev E Stat Nonlin Soft Matter Phys*. 2013; 88(6): 063011. doi: [10.1103/PhysRevE.88.063011](https://doi.org/10.1103/PhysRevE.88.063011)
18. Zheng J, Chen QF, Gu YJ, Chen ZY. Hugoniot measurements of double-shocked precompressed dense xenon plasmas. *Phys Rev E Stat Nonlin Soft Matter Phys*. 2012; 86(6): 066406. doi: [10.1103/PhysRevE.86.066406](https://doi.org/10.1103/PhysRevE.86.066406)
19. Falk K, Regan SP, Vorberger J, et al. Comparison between x-ray scattering and velocity-interferometry measurements from shocked liquid deuterium. *Phys Rev E Stat Nonlin Soft Matter Phys*. 2013; 87(4): 043112. doi: [10.1103/PhysRevE.87.043112](https://doi.org/10.1103/PhysRevE.87.043112)
20. Brujan EA, Ikeda T, Matsumoto Y. Jet formation and shock wave emission during collapse of ultrasound-induced cavitation bubbles and their role in the therapeutic applications of high-intensity focused ultrasound. *Phys Med Biol*. 2005; 50(20): 4797-4809. doi: [10.1088/0031-9155/50/20/004](https://doi.org/10.1088/0031-9155/50/20/004)
21. Iakovlev S, Iakovlev S, Buchner C, et al. Resonance-like phenomena in a submerged cylindrical shell subjected to two consecutive shock waves: The effect of the inner fluid. *J Fluids Struct*. 2014; 50: 153-170. doi: [10.1016/j.jfluidstructs.2014.05.013](https://doi.org/10.1016/j.jfluidstructs.2014.05.013)
22. Bringa EM, Caro A, Wang YM, et al. Ultrahigh strength in nanocrystalline materials under shock loading. *Science*. 2005; 309(5742): 1838-1841. doi: [10.1126/science.1116723](https://doi.org/10.1126/science.1116723)
23. Kadau K, Germann TC, Lomdahl PS, et al. Shock waves in polycrystalline iron. *Phys Rev Lett*. 2007; 98(13): 135701. doi: [10.1103/PhysRevLett.98.135701](https://doi.org/10.1103/PhysRevLett.98.135701)
24. Knudson MD, Desjarlais MP, Dolan DH. Shock-wave exploration of the high-pressure phases of carbon. *Science*. 2008; 322(5909): 1822-1825. doi: [10.1126/science.1165278](https://doi.org/10.1126/science.1165278)
25. Gurnett DA, Kurth WS. Electron plasma oscillations upstream of the solar wind termination shock. *Science*. 2005; 309(5743): 2025-2027. doi: [10.1126/science.1117425](https://doi.org/10.1126/science.1117425)
26. Gurnett DA, Kurth WS. Intense plasma waves at and near the solar wind termination shock. *Nature*. 2008; 454(7200): 78-80. doi: [10.1038/nature07023](https://doi.org/10.1038/nature07023)
27. Dutton Z, Budde M, Slowe C, Hau LV. Observation of quantum shock waves created with ultra-compressed slow light pulses in a Bose-Einstein condensate. *Science*. 2001; 293(5530): 663-668. doi: [10.1126/science.1062527](https://doi.org/10.1126/science.1062527)
28. Damski B. Shock waves in a one-dimensional Bose gas: From a Bose-Einstein condensate to a Tonks gas. *Phys Rev A*. 2006; 73(4): 043601. doi: [10.1103/physreva.73.043601](https://doi.org/10.1103/physreva.73.043601)
29. Chang JJ, Engels P, Hofer MA. Formation of dispersive shock waves by merging and splitting Bose-Einstein condensates. *Phys Rev Lett*. 2008; 101(17): 170404. doi: [10.1103/PhysRevLett.101.170404](https://doi.org/10.1103/PhysRevLett.101.170404)
30. Millot M, Dubrovinskaia N, Černok A, et al. Planetary science. Shock compression of stishovite and melting of silica at planetary interior conditions. *Science*. 2015; 347(6220): 418-420. doi: [10.1126/science.1261507](https://doi.org/10.1126/science.1261507)
31. McKee CF, Draine BT. Interstellar shock waves. *Science*. 1991; 252(5004): 397-403. doi: [10.1126/science.252.5004.397](https://doi.org/10.1126/science.252.5004.397)
32. McClure S, Dorfmueller C. Extracorporeal shock wave therapy: Theory and equipment. *Clin Tech Equine Pract*. 2002; 2(4): 348-357. doi: [10.1053/j.ctep.2004.04.008](https://doi.org/10.1053/j.ctep.2004.04.008)
33. Lingeman JE, McAteer JA, Gnessin E, Evan AP. Shock wave lithotripsy: Advances in technology and technique. *Nat Rev Urol*. 2009; 6(12): 660-670. doi: [10.1038/nrurol.2009.216](https://doi.org/10.1038/nrurol.2009.216)
34. Cherenkov PA. Visible emission of clean liquids by action of gamma radiation. *R Dokl Akad Nauk SSSR*. 1934; 2: 451-454. doi: [10.1234/12345678](https://doi.org/10.1234/12345678)
35. Rassweiler JJ, Knoll T, Kohrmann KU, et al. Shock wave technology and application: An update. *Eur Urol*. 2011; 59(5): 784-796. doi: [10.1016/j.eururo.2011.02.033](https://doi.org/10.1016/j.eururo.2011.02.033)
36. Coleman AJ, Saunders JE. A review of the physical proper-

- ties and biological effects of the high amplitude acoustic fields used in extracorporeal lithotripsy. *Ultrasonics*. 1993; 31(2): 75-89. doi: [10.1016/0041-624X\(93\)90037-Z](https://doi.org/10.1016/0041-624X(93)90037-Z)
37. McAteer JA, Evan AP. The acute and long-term adverse effects of shock wave lithotripsy. *Semin Nephrol*. 2008; 28(2): 200-213. doi: [10.1016/j.semnephrol.2008.01.003](https://doi.org/10.1016/j.semnephrol.2008.01.003)
38. Brümmer F, Bräuner T, Hülser DF. Biological effects of shock waves. *World J Urol*. 1990; 8(4): 224-232. doi: [10.1007/BF01580025](https://doi.org/10.1007/BF01580025)
39. Delius M. Medical applications and bioeffects of extracorporeal shock waves. *Shock Waves*. 1994; 4(2): 55-72. doi: [10.1007/BF01418569](https://doi.org/10.1007/BF01418569)
40. Oosterhof GO, Smits GA, De Ruyter AE, Schalken JA, Debryne FM. Effects of high-energy shock waves combined with biological response modifiers in different human kidney cancer xenografts. *Ultrasound Med Biol*. 1991; 17(4): 391-399. doi: [10.1016/0301-5629\(91\)90139-N](https://doi.org/10.1016/0301-5629(91)90139-N)
41. Gamarra F, Spelsberg F, Dellian M, Goetz AE. Complete local tumor remission after therapy with extra-corporeally applied high-energy shock waves (HESW). *Int J Cancer*. 1993; 55(1): 153-156. doi: [10.1002/ijc.2910550127](https://doi.org/10.1002/ijc.2910550127)
42. Lauer U, Bürgelt E, Squire Z, et al. Shock wave permeabilization as a new gene transfer method. *Gene Ther*. 1997; 4(7): 710-715. doi: [10.1038/sj.gt.3300462](https://doi.org/10.1038/sj.gt.3300462)
43. Bao S, Thrall BD, Gies RA, Miller DL. In vivo transfection of melanoma cells by lithotripter shock waves. *Cancer Res*. 1998; 58(2): 219-221. Web site: <http://cancerres.aacrjournals.org/content/58/2/219.short>. Accessed July 24, 2016
44. Delius M, Adams G. Shock wave permeabilization with ribosome inactivating proteins: A new approach to tumor therapy. *Cancer Res*. 1999; 59(20): 5227-5232. Web site: <http://cancerres.aacrjournals.org/content/59/20/5227.long>. Accessed July 24, 2016
45. Tschoep K, Hartmann G, Jox R, et al. Shock waves: A novel method for cytoplasmic delivery of antisense oligonucleotides. *J Mol Med*. 2001; 79(5-6): 306-313. doi: [10.1007/s001090100204](https://doi.org/10.1007/s001090100204)
46. Kodama T, Doukas AG, Hamblin MR. Delivery of ribosome-inactivating protein toxin into cancer cells with shock waves. *Cancer Lett*. 2003; 189(1): 69-75. doi: [10.1016/S0304-3835\(02\)00503-7](https://doi.org/10.1016/S0304-3835(02)00503-7)
47. Michel MS, Erben P, Trojan L, et al. Acoustic energy: a new transfection method for cancer of the prostate, cancer of the bladder and benign kidney cells. *Anticancer Res*. 2004; 24(4): 2303-2308. Web site: <http://ar.iiarjournals.org/content/24/4/2303>
- long. Accessed July 24, 2016
48. Ohl C-D, Wolfrum B. Detachment and sonoporation of adherent HeLa-cells by shock wave-induced cavitation. *Biochim Biophys Acta*. 2003; 1624(1-3): 131-138. doi: [10.1016/j.bbagen.2003.10.005](https://doi.org/10.1016/j.bbagen.2003.10.005)
49. Ohl C-D, Arora M, Ikink R, et al. Sonoporation from jetting cavitation bubbles. *Biophys J*. 2006; 91(11): 4285-4295. doi: [10.1529/biophysj.105.075366](https://doi.org/10.1529/biophysj.105.075366)
50. Moosavi-Nejad SF, Hosseini SMR, Satoh M, Takayama K. Shock wave induced cytoskeletal and morphological deformations in a human renal carcinoma cell line. *Cancer Sci*. 2006; 97(4): 296-304. doi: [10.1111/j.1349-7006.2006.00172.x](https://doi.org/10.1111/j.1349-7006.2006.00172.x)
51. Bushnell JC, McCloskey DJ. Thermoelastic stress production in solids. *J Appl Phys*. 1968; 39(12): 5541-5546. doi: [10.1063/1.1656010](https://doi.org/10.1063/1.1656010)
52. Yang LC. Stress waves generated in thin metallic films by a Q-switched ruby laser. 1974; 45(6): 2601-2608. doi: [10.1063/1.1663636](https://doi.org/10.1063/1.1663636)
53. Fabbro R, Fournier J, Ballard P, Devaux D, Virmont J. Physical study of laser-produced plasma in confined geometry. *J Appl Phys*. 1990; 68(2): 775-784. doi: [10.1063/1.346783](https://doi.org/10.1063/1.346783)
54. Venugopalan V, Deutsch TF. Stress generated in polyimide by excimer-laser irradiation. *J Appl Phys*. 1993; 74(6): 4181-4189. doi: [10.1063/1.354422](https://doi.org/10.1063/1.354422)
55. Doukas AG, Flotte TJ. Physical characteristics and biological effects of laser-induced stress waves. *Ultrasound Med Biol*. 1996; 22(2): 151-164. doi: [10.1016/0301-5629\(95\)02026-8](https://doi.org/10.1016/0301-5629(95)02026-8)
56. Yao C-P, Zhang Z-X, Rahmanzadeh R, Huettmann G. Laser-based gene transfection and gene therapy. *IEEE Trans Nanobiosci*. 2008; 7(2): 111-119. doi: [10.1109/TNB.2008.2000742](https://doi.org/10.1109/TNB.2008.2000742)
57. Doukas AG, Kollias N. Transdermal drug delivery with a pressure wave. *Adv Drug Deliver Rev*. 2004; 56(5): 559-579. doi: [10.1016/j.addr.2003.10.031](https://doi.org/10.1016/j.addr.2003.10.031)
58. Brümmer F, Brenner J, Bräuner T, Hülser DF. Effect of shock waves on suspended and immobilized L1210 cells. *Ultrasound Med Biol*. 1989; 15(3): 229-239. doi: [10.1016/0301-5629\(89\)90067-7](https://doi.org/10.1016/0301-5629(89)90067-7)
59. de Reijke TM, Schamhart DH, Kurth KH, Löwik CW, Donkers LH, Sterenberg HJ. Tumor growth delay by laser-generated shock waves. *Lasers Surg Med*. 1994; 14(3): 205-212. doi: [10.1002/lsm.1900140302](https://doi.org/10.1002/lsm.1900140302)
60. Doukas AG, McAuliffe DJ, Lee S, Venugopalan V, Flotte

- TJ. Physical factors involved in stress-wave-induced cell injury: The effect of stress gradient. *Ultrasound Med Biol.* 1995; 21(7): 961-967. doi: [10.1016/0301-5629\(95\)00027-0](https://doi.org/10.1016/0301-5629(95)00027-0)
61. Lee S, Anderson T, Zhang H, Flotte TJ, Doukas AG. Alteration of cell membrane by stress waves in vitro. *Ultrasound Med Biol.* 1996; 22(9): 1285-1293. doi: [10.1016/S0301-5629\(96\)00149-4](https://doi.org/10.1016/S0301-5629(96)00149-4)
62. Douki T, Lee S, Dorey K, Flotte TJ, Deutsch TF, Doukas AG. Stress-wave-induced injury to retinal pigment epithelium cells in vitro. *Lasers Surg Med.* 1996; 19(3): 249-259. doi: [10.1002/\(SICI\)1096-9101\(1996\)19:3<249::AID-LSM1>3.0.CO;2-S](https://doi.org/10.1002/(SICI)1096-9101(1996)19:3<249::AID-LSM1>3.0.CO;2-S)
63. Huber PE, Jenne J, Debus JJ, Wannemacher MF, Pfisterer P. A comparison of shock wave and sinusoidal-focused ultrasound-induced localized transfection of HeLa cells. *Ultrasound Med Biol.* 1999; 25(9): 1451-1457. doi: [10.1016/S0301-5629\(99\)00099-X](https://doi.org/10.1016/S0301-5629(99)00099-X)
64. Kohri K, Uemura T, Iguchi M, Kurita T. Effect of high energy shock waves on tumor cells. *Urol Res.* 1990; 18(2): 101-105. doi: [10.1007/BF00302468](https://doi.org/10.1007/BF00302468)
65. Mulholland SE, Lee S, McAuliffe DJ, Doukas AG. Cell loading with laser-generated stress waves: The role of the stress gradient. *Pharm Res.* 1999; 16(4): 514-518. doi: [10.1023/A:1018814911497](https://doi.org/10.1023/A:1018814911497)
66. Lee S, Doukas AG. Laser-generated stress waves and their effects on the cell membrane. *IEEE J Sel Top Quant.* 1999; 5(4): 997-1003. doi: [10.1109/2944.796322](https://doi.org/10.1109/2944.796322)
67. Kato M, Ioritani N, Suzuki T, et al. Mechanism of anti-tumor effect of combination of bleomycin and shock waves. *Jpn J Cancer Res.* 2000; 91(10): 1065-1072. doi: [10.1111/j.1349-7006.2000.tb00886.x](https://doi.org/10.1111/j.1349-7006.2000.tb00886.x)
68. Sondén A, Svensson B, Roman N, Brismar B, Palmblad J, Kjellstöm BT. Mechanisms of shock wave induced endothelial cell injury. *Lasers Surg Med.* 2002; 31(4): 233-241. doi: [10.1002/lsm.10093](https://doi.org/10.1002/lsm.10093)
69. Kodama T, Kodama T, Hamblin MR, Hamblin MR, Doukas AG. Cytoplasmic molecular delivery with shock waves: Importance of impulse. *Biophys J.* 2000; 79(4): 1821-1832. doi: [10.1016/S0006-3495\(00\)76432-0](https://doi.org/10.1016/S0006-3495(00)76432-0)
70. Juhasz T, Hu XH, Turi L, Bor Z. Dynamics of shock waves and cavitation bubbles generated by picosecond laser pulses in corneal tissue and water. *Lasers Surg Med.* 1993; 15(1): 91-98. doi: [10.1002/lsm.1900150112](https://doi.org/10.1002/lsm.1900150112)
71. Strand OT, Goosman DR, Martinez C, Whitworth TL, Kuhlow WW. Compact system for high-speed velocimetry using heterodyne techniques. *Rev Sci Instrum.* 2006; 77(8): 083108. doi: [10.1063/1.2336749](https://doi.org/10.1063/1.2336749)
72. Schmidt M, Kahlert U, Wessolleck J, et al. Characterization of a setup to test the impact of high-amplitude pressure waves on living cells. *Nature Sci Rep.* 2014; 4: 3849. doi: [10.1038/srep03849](https://doi.org/10.1038/srep03849)
73. Steinhauser MO, Steinhauser MO, Schmidt M. Destruction of cancer cells by laser-induced shock waves: Recent developments in experimental treatments and multiscale computer simulations. *Soft Matter.* 2014; 10(27): 4778-4788. doi: [10.1039/c4sm00407h](https://doi.org/10.1039/c4sm00407h)
74. Fung YC. *Biomechanics: Motion, Flow, Stress, and Growth.* New York, USA: Springer; 1990.
75. Verdier C. Rheological Properties of Living Materials. From Cells to Tissues. *J Theoretical Medicine.* 2003; 5(2): 67-91. doi: [10.1080/10273360410001678083](https://doi.org/10.1080/10273360410001678083)
76. de Gennes PG. *Scaling Concepts in Polymer Physics.* Ithaca, London, UK; Cornell University Press; 1979.
77. Steinhauser MO. *Computational Multiscale Modeling of Fluids and Solids - Theory and Applications.* 2nd ed. New York, USA: Springer; 2016.
78. Steinhauser MO. A molecular dynamics study on universal properties of polymer chains in different solvent qualities. Part I. A review of linear chain properties. *J Chem Phys.* 2005; 122(9): 094901. doi: [10.1063/1.1846651](https://doi.org/10.1063/1.1846651)
79. Bienfait Y. Modelling and molecular dynamics simulations of flexible polymer networks. In: Steinhauser MO, ed. December 2013.
80. Schindler T, Kröner D, Steinhauser MO. On the dynamics of molecular self-assembly and the structural analysis of bilayer membranes using coarse-grained molecular dynamics simulations. *Biochim Biophys Acta.* 2016; 1858(9): 1955-1963. doi: [10.1016/j.bbamem.2016.05.014](https://doi.org/10.1016/j.bbamem.2016.05.014)
81. Doi M, Edwards SF. *The Theory of Polymer Dynamics.* New York, USA: Clarendon Press, Oxford; 1986.
82. Bird RB, Hassager O, Armstrong RC, Curtis CF. *Dynamics of Polymeric Liquids.* New York, USA: Wiley; 1977.
83. Larson RG. *The Structure and Rheology of Complex Fluids.* New York, USA: Oxford University Press; 1999.
84. Winter HH. Analysis of linear viscoelasticity of a crosslinking polymer at the gel point. *J Rheol.* 1986; 30(2): 367. doi: [10.1122/1.549853](https://doi.org/10.1122/1.549853)

85. Flory PJ. *Statistical Mechanics of Chain Molecules*. New Jersey, USA: John Wiley & Sons, Inc; 1969.
86. Einstein A. Eine neue Bestimmung der Moleküldimensionen. *Ann Phys*. 1906; 324(2): 289-306. doi: [10.1002/andp.19063240204](https://doi.org/10.1002/andp.19063240204)
87. Oldroyd JG. The elastic and viscous properties of emulsions and suspensions. *Science*. 1953; 218(1132): 122-132. doi: [10.1098/rspa.1953.0092](https://doi.org/10.1098/rspa.1953.0092)
88. Hashin Z, Rosen BW. The elastic moduli of fiber-reinforced materials. *J Appl Mech*. 1964; 31(2): 223-232. doi: [10.1115/1.3629590](https://doi.org/10.1115/1.3629590)
89. Hill CR. Theory of mechanical properties of fibre-strengthened materials: I. Elastic behaviour. *J Mech Phys Solids*. 1964; 12(4): 199-212. doi: [10.1016/0022-5096\(64\)90019-5](https://doi.org/10.1016/0022-5096(64)90019-5)
90. Fung YC. Microrheology and constitutive equation of soft tissue. *Biorheology*. 1988; 25(1-2): 261-270. Web site: <http://europepmc.org/abstract/med/3196823>. Accessed July 24, 2016
91. Choy TC. *Effective Medium Theory: Principles and Applications*. Oxford, UK: Oxford University Press; 1999.
92. Ingber DE, Heidemann SR, Lamoureux P, Buxbaum RE. Opposing views on tensegrity as a structural framework for understanding cell mechanics. *J Appl Physiol*. 2000; 89(4): 1663-1678. doi: [10.1016/0012-1606\(71\)90073-X](https://doi.org/10.1016/0012-1606(71)90073-X)
93. Stamenovic D, Ingber DE. Models of cytoskeletal mechanics of adherent cells. *Biomech Model Mechan*. 2002; 1(1): 95-108. doi: [10.1007/s10237-002-0009-9](https://doi.org/10.1007/s10237-002-0009-9)
94. Ingber DE. Tensegrity I. Cell structure and hierarchical systems biology. *J Cell Sci*. 2003; 116(Pt 7): 1157-1173. doi: [10.1242/jcs.00359](https://doi.org/10.1242/jcs.00359)
95. Wang N, Naruse K, Stamenovic D, et al. Mechanical behavior in living cells consistent with the tensegrity model. *Proc Natl Acad Sci*. 2001; 98(14): 7765-7770. doi: [10.1073/pnas.141199598](https://doi.org/10.1073/pnas.141199598)
96. Ingber DE, Wang N, Stamenovic D. Tensegrity, cellular biophysics, and the mechanics of living systems. *Rep Prog Phys*. 2014; 77(4): 046603. doi: [10.1088/0034-4885/77/4/046603](https://doi.org/10.1088/0034-4885/77/4/046603)
97. Pritchard RH, Huang YYS, Terentjev EM. Mechanics of biological networks: From the cell cytoskeleton to connective tissue. *Soft Matter*. 2014; 10(12): 1864-1884. doi: [10.1039/c3sm52769g](https://doi.org/10.1039/c3sm52769g)
98. Ingber DE, Madri JA, Jamieson JD. Role of basal lamina in neoplastic disorganization of tissue architecture. *PNAS*. 1981; 78(6): 3901-3905. Web site: <http://www.pnas.org/content/78/6/3901.short>. Accessed July 24, 2016
99. Chen D, Wen Q, Janmey PA. Rheology of soft materials. *Condensed Matter Physics*. 2010; 1: 301-322. doi: [10.1146/annurev-conmatphys-070909-104120](https://doi.org/10.1146/annurev-conmatphys-070909-104120)
100. Müller KW, Bruinsma RF, Lieleg O, Bausch AR, Wall WA, Levine AJ. Rheology of semiflexible bundle networks with transient linkers. *Phys Rev Lett*. 2014; 112(23): 238102-238102. doi: [10.1103/PhysRevLett.112.238102](https://doi.org/10.1103/PhysRevLett.112.238102)
101. Brunner C, Niendorf A, Käs JA. Passive and active single-cell biomechanics: A new perspective in cancer diagnosis. *Soft Matter*. 2009; 5(11): 2171-2178. doi: [10.1039/b807545j](https://doi.org/10.1039/b807545j)
102. Sayed El T, Mota A, Fraternali F, Ortiz M. A variational constitutive model for soft biological tissues. *J Biomech*. 2008; 41(7): 1458-1466. doi: [10.1016/j.jbiomech.2008.02.023](https://doi.org/10.1016/j.jbiomech.2008.02.023)
103. Qin Z, Dimas L, Adler D, Bratzel G, Buehler MJ. Biological materials by design. *J Phys Condens Matter*. 2014; 26(7): 073101. doi: [10.1088/0953-8984/26/7/073101](https://doi.org/10.1088/0953-8984/26/7/073101)
104. Meyers MA, Chen P-Y, Lopez MI, Seki Y, Lin AYM. Biological materials: A materials science approach. *J Mech Behav Biomed*. 2011; 4(5): 626-657. doi: [10.1016/j.jmbbm.2010.08.005](https://doi.org/10.1016/j.jmbbm.2010.08.005)
105. Ogden RW. Large Deformation Isotropic Elasticity - On the Correlation of Theory and Experiment for Incompressible Rubberlike Solids. *Proceedings of the Royal Society of London A: Mathematical, Physical and Engineering Sciences*. 1972; 326(1567): 565-584. doi: [10.1098/rspa.1972.0026](https://doi.org/10.1098/rspa.1972.0026)
106. Mooney M. A theory of large elastic deformation. *J Appl Phys*. 1940; 11(9): 582-592. doi: [10.1063/1.1712836](https://doi.org/10.1063/1.1712836)
107. Rivlin RS. Large Elastic Deformations of Isotropic Materials. IV. Further Developments of the General Theory. *Philosophical Transactions of the Royal Society of London Series A Mathematical and Physical Sciences*. 1948; 241(8): 379-397. doi: [10.1098/rsta.1948.0024](https://doi.org/10.1098/rsta.1948.0024)
108. Miller K, Chinzei K. Mechanical properties of brain tissue in tension. *J Biomech*. 2002; 35(4): 483-490. doi: [10.1016/S0021-9290\(01\)00234-2](https://doi.org/10.1016/S0021-9290(01)00234-2)
109. Xu M, Nowinski WL. Talairach-Tournoux brain atlas registration using a metalforming principle-based finite element method. *Med Image Anal*. 2001; 5(4): 271-279. doi: [10.1016/S1361-8415\(01\)00045-7](https://doi.org/10.1016/S1361-8415(01)00045-7)
110. Warfield SK, Haker SJ, Talos I-F, et al. Capturing intraoperative deformations: research experience at Brigham and Women's Hospital. *Med Image Anal*. 2005; 9(2): 145-162. doi: [10.1016/j.media.2004.11.005](https://doi.org/10.1016/j.media.2004.11.005)

111. Miller K, Chinzei K. Constitutive modelling of brain tissue: Experiment and theory. *J Biomech.* 1997; 30(11-12): 1115-1121. doi: [10.1016/S0021-9290\(97\)00092-4](https://doi.org/10.1016/S0021-9290(97)00092-4)
112. Miller K. Method of testing very soft biological tissues in compression. *J Biomech.* 2005; 38(1): 153-158. doi: [10.1016/j.jbiomech.2004.03.004](https://doi.org/10.1016/j.jbiomech.2004.03.004)
113. Wittek A, Kikinis R, Warfield SK, Miller K. Brain shift computation using a fully nonlinear biomechanical model. *Med Image Comput Comput Assist Interv.* 2005; 8(Pt 2): 583-590. doi: [10.1007/11566489_72](https://doi.org/10.1007/11566489_72)
114. Wittek A, Hawkins T, Miller K. On the unimportance of constitutive models in computing brain deformation for image-guided surgery. *Biomech Model Mechan.* 2008; 8(1): 77-84. doi: [10.1007/s10237-008-0118-1](https://doi.org/10.1007/s10237-008-0118-1)
115. Dumpuri P, Thompson RC, Dawant BM, Cao A, Miga MI. An atlas-based method to compensate for brain shift: Preliminary results. *Med Image Anal.* 2007; 11(2): 128-145. doi: [10.1016/j.media.2006.11.002](https://doi.org/10.1016/j.media.2006.11.002)
116. Bathe KJ. *Finite Element Procedures in Engineering Analysis.* Cambridge, UK: Prentice Hall; 1982.
117. Cash DM, Miga MI, Sinha TK, Galloway RL, Chapman WC. Compensating for intraoperative soft-tissue deformations using incomplete surface data and finite elements. *IEEE Trans Med Imaging.* 2005; 24(11): 1479-1491. doi: [10.1109/TMI.2005.855434](https://doi.org/10.1109/TMI.2005.855434)
118. Kim JS, Sun SX. Continuum modeling of forces in growing viscoelastic cytoskeletal networks. *J Theor Biol.* 2009; 256(4): 596-606. doi: [10.1016/j.jtbi.2008.10.023](https://doi.org/10.1016/j.jtbi.2008.10.023)
119. Kim S-H, Suh HS, Cho MH, Lee SY, Kim T-S. Finite element simulation of ultrasound propagation in bone for quantitative ultrasound toward the diagnosis of osteoporosis. *Conf Proc IEEE Eng Med Biol Soc.* 2009; 2009: 436-439. doi: [10.1109/IEMBS.2009.5334707](https://doi.org/10.1109/IEMBS.2009.5334707)
120. Hostettler A, George D, Rémond Y, Nicolau SA, Soler L, Marescaux J. Bulk modulus and volume variation measurement of the liver and the kidneys in vivo using abdominal kinetics during free breathing. *Comput Meth Prog Bio.* 2010; 100(2): 149-157. doi: [10.1016/j.cmpb.2010.03.003](https://doi.org/10.1016/j.cmpb.2010.03.003)
121. Cleveland RO, Lifshitz DA, Connors BA, Evan AP, Willis LR, Crum LA. In vivo pressure measurements of lithotripsy shock waves in pigs. *Ultrasound Med Biol.* 1998; 24(2): 293-306. doi: [10.1016/S0301-5629\(97\)00270-6](https://doi.org/10.1016/S0301-5629(97)00270-6)
122. Schwartz J-M, Denninger M, Rancourt D, Moisan C, Laurendeau D. Modelling liver tissue properties using a non-linear visco-elastic model for surgery simulation. *Med Image Anal.* 2005; 9(2): 103-112. doi: [10.1016/j.media.2004.11.002](https://doi.org/10.1016/j.media.2004.11.002)
123. Nava A, Mazza E, Kleinermann F, Avis NJ, McClure J. Determination of the mechanical properties of soft human tissues through aspiration experiments. *Medical Image Computing and Computer-Assisted Intervention.* 2003; 2003: 222-229. doi: [10.1007/978-3-540-39899-8_28](https://doi.org/10.1007/978-3-540-39899-8_28)
124. Ottensmeyer MP. Minimally invasive instrument for in vivo measurement of solid organ mechanical impedance. Web site. <https://dspace.mit.edu/handle/1721.1/8858>. Accessed July 24, 2016
125. Zhu Y, Dong Z, Wejinya UC, Jin S, Ye K. Determination of mechanical properties of soft tissue scaffolds by atomic force microscopy nanoindentation. *J Biomech.* 2011; 44(13): 2356-2361. doi: [10.1016/j.jbiomech.2011.07.010](https://doi.org/10.1016/j.jbiomech.2011.07.010)